DISSERTATION
SUBMITTED TO THE
COMBINED FACULTIES FOR THE NATURAL
SCIENCES AND FOR MATHEMATICS
OF THE RUPERTO-CAROLA UNIVERSITY OF
HEIDELBERG, GERMANY
FOR THE DEGREE OF
DOCTOR OF NATURAL SCIENCES

presented by

Dipl. Phys. Birgitta Schiedt
born in: Ludwigshafen am Rhein

Oral examination: May 16, 2007

CHARACTERIZATION AND APPLICATION OF ION TRACK-ETCHED NANOPORES

Referees: Prof. Dr. Reinhard Neumann

Prof. Dr. Wolfgang Ensinger

ZUSAMMENFASSUNG

Thema dieser Arbeit sind Untersuchungen der Transporteigenschaften einzelner, konischer Nanoporen in Polymerfolien, sowie deren Anwendung als Biosensoren. Die Herstellung der Poren erfolgte durch Aufätzen der Schadenspuren energiereicher Schwerionen (Ionenspurätztechnik).

Die Geometrie solcher sowie zylindrischer Poren wurde mit unterschiedlichen Methoden (Röntgenkleinwinkelstreuung, Elektronenmikroskopie, Leitfähigkeitsmessungen) untersucht, mit dem Ergebnis, daß der Porendurchmesser nahe der Oberfläche kleiner als im Inneren der Membran ist.

Die untersuchten konischen Poren sind kationenselektiv und zeigen asymmetrische Strom-Spannungs ($I - U$) Kennlinien, deren Charakteristika von pH-Wert und Konzentration des für die Messung verwendeten Elektrolyten abhängen. Diese Eigenschaften resultieren aus der aufgrund des Herstellungsprozesses negativ geladenen Oberfläche der Poren, die zu einer asymmetrischen Potentialverteilung entlang der Porenachse führt. Maximale Asymmetrie der $I - U$ -Kurven ist bei einer KCl-Konzentration von etwa 0.1 M zu beobachten. Rechnungen mit einem einfachen Kontinuumsmodell führten zum gleichen Ergebnis.

Die Selektivität der Poren hängt von der Richtung eines äußeren Konzentrationsgradienten ab. Sie ist höher, wenn die niedrigere Konzentration sich auf der Seite der kleinen Porenöffnung befindet. Auch hier ergab sich qualitaitve Übereinstimmung mit den Modellrechnungen.

Geringe Konzentrationen von divalenten Kationen beinflussen stark die Transporteigenschaften der untersuchten Poren.

Konische Kaptonporen konnten zudem zum Nachweis einzelner DNA-Moleküle verwendet werden, die während ihres Durchgangs durch die Pore den Ionenstrom verringern.

ABSTRACT

This thesis investigates the ionic transport properties of single, conical nanopores in polymers, as well as their applicability as single-molecule sensors. The pores were produced by selective etching of the damaged zones of energetic heavy ions (track-etching technique).

More basic investigations of the shape of track-etched pores (by small-angle X-ray scattering, electron microscopy and conductometry) are also included, revealing smaller pore sizes on top of a membrane than inside the pore.

Conical track-etched nanopores are cation selective and show asymmetric $I - V$ characteristics, depending on pH value and concentration

of the electrolyte. These properties result from their negative surface charges created during the etching process, which lead to an intrinsic asymmetric electric potential along the pore axis. Experiments show a maximum for the rectification at about 0.1 M KCl, in accordance with theoretical calculations.

The selectivity of the pores depends on the direction of an applied concentration gradient, being higher for the lower concentration facing the small opening of the pore, again in agreement with calculations.

The pores transport properties are strongly influenced by small concentrations of divalent cations.

Conical polyimide pores have been found suitable to detect single DNA molecules passing through them via changes in the ionic current.

CONTENTS

1 INTRODUCTION

It is nowadays well known that properties of materials on the nanoscale can be quite different from their macroscopic counterparts. One reason for that is the increasing surface to volume ratio which enhances the influence of surface properties. Also, as one approaches the molecular scale, the particle nature of matter becomes relevant in physical processes, for example as the dimensions of electronic devices approach the electron mean free path length, or those of ionic devices reach the distances between ions in solution.

While the fabrication of nanostructures has become more and more sophisticated in recent years only, a broad range of ready-made structures exist in nature. Some of the most important of these are ion channels in cell membranes, which are responsible for all generation and transduction of electrical signals in living organisms, e. g., in nerve and muscle cells [1]. While the structures of these channels can be determined nowadays, e. g., by X-ray diffraction [2, 3][1], and techniques like patch-clamping make it possible to study the transport properties of single channels, resulting in knowledge about their function [3–8], there is still very much research going on in this field, especially concerning diseases related to ion channel dysfunctions.

Nanopores (natural as well as synthetic ones) have a large potential in biotechnology, where they can be applied as filters, sensors for biomolecules or as single-molecule detectors and analyzers. A broad range of work is currently going on in the latter field, which is based on the fact that the translocation of a single molecule with a size comparable to that of the pore can be detected as a change in the ionic current during the passage time of the molecule. Early work in this field started using the protein pore α-hemolysin as the nanopore [9–18], but the focus has moved more and more towards solid-state nanopores due to their higher durability [19–26]. For all these applications it is crucial to have a fundamental understanding of how ions and (charged) molecules are transported in systems with nanometer scale geometries.

Single ion track-etched pores in polymer foils have been found to show some properties similar to biological channels, such as selectivity [27, 28], voltage-dependent current fluctuations [29, 30] and rectification [31–33] of ionic current. Thus, it is of special interest to further investigate the underlying mechanisms of these effects.

1 R. MacKinnon was the first to publish the X-ray structure of a potassium channel in 1998, a work so important that he got the nobel prize in chemistry for it only five years later, in 2003 [2].

The aim of this thesis was to continue these fundamental studies of transport properties of single conical pores and at the same time explore their potential in biotechnological applications, especially in single-molecule sensing. These topics are covered in several relatively self-contained sections.

First, techniques and materials used for the production of the pores under study are described in chapter 2. This includes irradiation by heavy ions, etching techniques used to develop latent ion tracks into pores of various geometries as well as an overview of the different polymers used.

Chapter 3 deals with the range of techniques which are used to determine nanopore geometry, both aggregate values for many-pore membranes and individual measurements for single pores. The most important method for single pores is to extract their size from conductivity measurements, while for samples containing a large number of pores electron microscopy is widely used. The limits of these techniques are also discussed. In addition, a section about small-angle X-ray scattering on multi-pore samples is included, a method yielding 3D-information about a large pore ensemble.

The chapters 4 and 5 are devoted to studies of the ionic transport characteristics rectification and selectivity under different external electrolyte conditions. Here a comparison is made with a theoretical model developed by J. Cervera and P. Ramírez [34].

Chapter 6 discusses blockage by divalent cations, another similarity with biochannels [35, 36]. This is introduced mainly phenomenologically, since a full theory describing this effect has yet to be developed.

The principle of single-molecule detection is described in chapter 7, together with an overview of the work done up to now with biological as well as with synthetic nanopores. First experiments with track-etched pores are presented, using DNA as the molecule to be sensed.

Finally, this thesis concludes with a discussion of the results achieved, and an outlook on the work planned for the near future.

2 FABRICATION OF TRACK-ETCHED NANOPORES

The nanopores investigated here are produced in polymer foils using the ion track-etching technique [37]. This method, which has become well established to create very uniform pores in insulators, is based on the following effect: When a swift heavy ions passes through matter, it deposits its energy along its trajectory, thus creating a cylindrical damage zone, the latent track. By suitable wet etchants the damaged material along the track can be removed quicker than the bulk material, thus developing the tracks into pores. Size and shape of these pores can be controlled, e. g., via etching time and etching solution. Under suitable conditions, pores down to a few nanometers in diameter can be produced.

2.1 HEAVY-ION IRRADIATION

Charged particles which penetrate a solid, can lose their energy via various interaction types, such as [38]

- Excitation and ionization of target electrons (electronic energy loss)
- Projectile excitation and ionization
- Electron capture
- Elastic collisions with target atoms (nuclear energy loss)
- Electromagnetic radiation (Bremsstrahlung, Cherenkov effect)

For heavy ions, the crucial processes are nuclear and electronic energy loss, dominating at low ($\leq$ 00.1 MeV/u) and higher ($>$ 0.1 MeV/u) kinetic energies, respectively. Only at extremely high velocities, where relativistic effects cannot be neglected any more and the energy of the ions is much higher than their rest mass, the radiative processes start to play a role. The energy loss depending on the specific energy of the incoming ion is displayed in Fig. 1 for a uranium ion passing through polyimide, calculated using the SRIM03 code [39]. It is a characteristic of fast ions that the maximum of their electronic energy loss occurs shortly before the particle is stopped, because their interaction cross section for these processes increases with decreasing velocity. This maximum is called the Bragg peak and its existence is exploited in radiation tumor therapy, where most of the energy is deposited inside the tumor and not in the tissue in front of it.

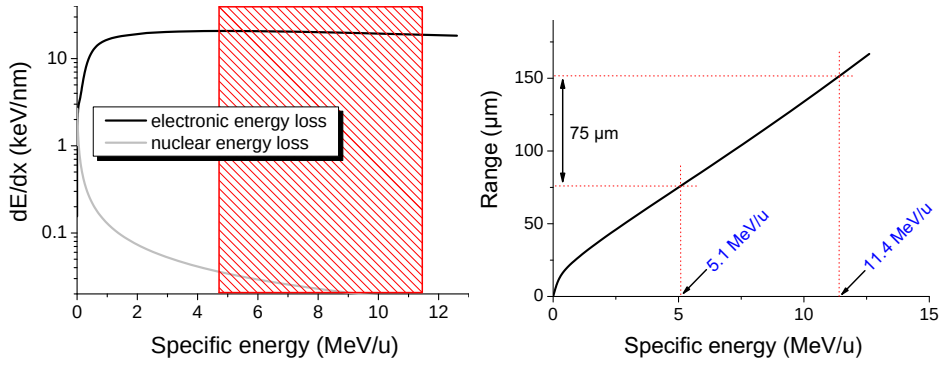

(a) (b)

Figure 1. a) Nuclear and electronic energy loss depending on the specific energy of ^{238}U in polyimide; the hatched area corresponds to the energy region an ion with initial energy of 11.4 MeV/u passes during the irradiation of 75 µm polyimide. b) Range of uranium in polyimide depending on specific energy; both calculated by SRIM03. The Bragg peak, which is rather broad for uranium, is not clearly visible in this picture due to the chosen plotting range.

The electronic energy loss can be described by the Bethe-Bloch formula [40]

$$\frac{\mathrm{d}E}{\mathrm{d}x} = \frac{4\pi \cdot e^4 \cdot Z_{\mathrm{eff}}^2 \cdot Z_t \cdot N}{m_e \cdot v^2} \left[\ln\left(\frac{2m_e v^2}{I}\right) - \beta^2 - \delta - U \right], \tag{2.1}$$

where

e	elementary charge
Z_{eff}	effective charge of the projectile
Z_t	atomic number
N	number of target atoms per unit volume
m_e	electron mass
v	velocity of the ion
I	ionisation energy
β	v/c
δ	relativistic correction
U	correction taking into account screening of inner electrons

The effective charge, which is crucial for the energy loss, depends on interactions of the projectile with the target. If the velocity of the incoming ion is higher than the orbital velocities of its electrons, the slowest electrons will be stripped off and the ion thus changes its charge state. For very high velocities, the ion loses all its electrons and $Z_{\mathrm{eff}} = Z$, with Z being the atomic number of the ion. Z_{eff} can be described by the

empirical Barkas formula [37]:

$$Z_{\text{eff}} = Z\left[1 - \exp\left(-\frac{130\beta}{Z^{2/3}}\right)\right]. \tag{2.2}$$

Therefore, heavier ions have a higher effective charge and thus a higher energy loss. This makes them ideal for creating continuous etchable tracks, which requires a material dependent minimal energy loss, being about 2–5 keV/nm for polymers [41].

The polymer foils used here for nanopore fabrication have a thickness of typically 12.5 µm and are irradiated in stacks of 6 by heavy ions (^{197}Au, ^{206}Pb and ^{238}U) of energy 11.4 MeV/u at the linear accelerator UNILAC of GSI. At this energy, the electronic energy loss, which has a maximum at about 4 MeV/u dominates and nuclear interactions can be neglected as long as the ion is not stopped inside the material.

The projected range R of an ion depends on its initial kinetic energy E_0 and its energy loss $\mathrm{d}E/\mathrm{d}x$ in the material. R is given by

$$R = \int_0^{E_0} \left(\frac{\mathrm{d}E}{\mathrm{d}x}\right)^{-1} \mathrm{d}E. \tag{2.3}$$

The range for a uranium ion with initial energy 11.4 MeV/u is about 152 µm (calculated by means of the SRIM code). As can be seen in Fig. 1(b), a uranium ion has still an energy of about 5.1 MeV/u after passing through 75 µm (a stack of 6 times 12.5 µm) of polyimide. Therefore, its energy loss is more or less constant between 19 and 21 keV/nm (Fig. 1(a)) throughout the whole stack, thus being well above the threshold for track formation.

The incident ion induces ionization and electric excitation, which in polymers predominantly lead to the destruction of chemical bonds (degradation) [42, 43], creation of unsaturated bonds and amorphisation in the case of polycrystalline material. Small volatile fragments can also outgas and thus reduce the density in the latent track [44, 45].

The density of track-etched pores in a sample can be varied via the applied fluence; here membranes with 10^7–$3{\cdot}10^8$ tracks/cm^2 have been used, in addition to membranes with just one single track. Single-ion irradiation is performed in the following way: A metal mask with a centered aperture of diameter $d = 300$ µm is placed in front of the sample, which is then irradiated with a defocused ion beam. The frequency of ions passing through the aperture is lowered thereby to a few ions/s. This makes it possible to switch off the beam by electrostatic deflection as soon as the detector behind the sample registers the first ion, thus avoiding the passage of a second one. The sample holder used for the irradiation of foils having a diameter of 30 mm is shown in Fig. 2 together with the metal mask used for the single-ion irradiation.

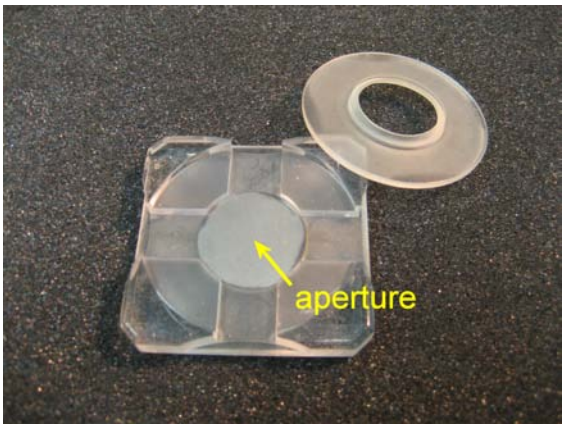

Figure 2. Sample holder used for the irradiation of foils having a diameter of 30 mm including the metal mask used for single-ion irradiation.

2.2 ETCHING

The final shape of the etched pores depends on how much faster the track is etched in comparison to the bulk material, which is removed isotropically during the etching process. While the bulk-etch velocity v_b (etch rate of undamaged material) and the track-etch velocity v_t (etch rate along the track) both depend on the etching conditions, v_t is also influenced by the energy loss of the incoming ion. It increases linearly with increasing $\mathrm{d}E/\mathrm{d}x$, due to the higher damage along the ion track.

The etching process is shown schematically in Fig. 3. The opening angle φ of the resulting pore is determined by the ratio v_t and v_b. The higher the track-etch velocity v_t is compared to the bulk-etch velocity v_b, the more cylindrical the pores become.

2.2.1 *Etching of single-pore membranes*

To produce a single pore with a specific size, it is necessary to monitor the etching process online to be able to stop the etching at the right time. This is possible by etching in a conductivity cell (Fig. 4), in which the polymer foil separates the two halves of the cell. To create a cylindrical pore, both halves of the cell are filled with the etching solution, and a voltage of typically 1 V is applied across the membrane to constantly monitor the current flowing through it during the etching. As long as the pore is not yet etched through, the membrane acts as an infinitely large resistance, and no current will flow. As soon as the two etching cones, which are created along the track from both sides, meet, the pore opens (this is called 'breakthrough') and a sudden jump in current is observed. Since the magnitude of the current flowing is proportional

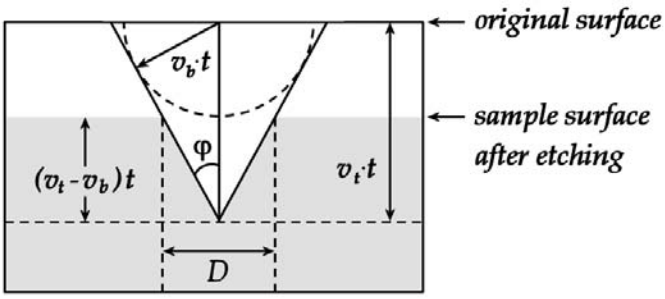

Figure 3. Schematic of an etched ion track. The opening angle φ is determined by the ratio of track etch rate v_t and bulk etch rate v_b. D is the final pore diameter.

to the cross section area of the pore ($I \sim r^2$), the widening of the pore during further etching is observed as a quadratic increase in the current. Therefore, it is possible to observe the increasing pore size during the etching and stop it as soon as the desired pore diameter d is reached. To calculate d directly from the measured current, one has to know the length of the pore (corresponding to the foil thickness) as well as the specific conductivity of the etching solution, and one has to assume a certain pore geometry. The resistance R of the pore is proportional to the reciprocal of the specific conductivity κ as well as to the integral over the reciprocal value of the cross-section area A of the pore:

$$R = \frac{1}{\kappa} \int_0^L \frac{1}{A(x)} \mathrm{d}x. \tag{2.4}$$

More details about how to determine the size of pores with different geometry via their conductance are described in section 3.1.

For the current measurements during the etching, gold electrodes are used due to their chemical resistance, which is important in the aggressive environment of the etching solution.

Conical pores

To create a conical pore, etching is performed from one side only, the other half of the cell contains a solution that is able to neutralize the etchant as soon as the pore opens, thus slowing down the further etching process. To additionally stop the etching, the voltage used to monitor the etching process is applied in such a way, that the negatively charged ions of the etchant are drawn out of the pore tip (Fig. 5). This twofold automatic stopping is mandatory for the controlled production of nanosized pores.

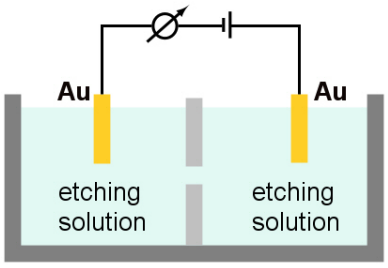

Figure 4. Principle of etching a cylindrical pore in a conductivity cell. The conductance of the membrane is monitored by applying a constant voltage between the two halves of the cell and constantly measuring the current with picoampere precision.

The dynamic of the opening process is different for the etching of PET

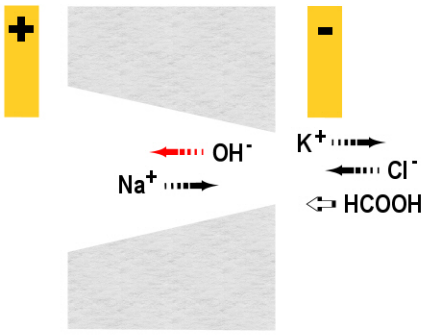

Figure 5. a) Principle of electro-stopping, illustrated for etching with NaOH and a stopping solution 1 M KCl + 1 M HCOOH. The formic acid neutralizes the sodium hydroxide as soon as it comes in contact with it.

and polyimide [46] using the following etching and stopping solutions: PET: 9 M NaOH for etching, 1 M KCl + 1 M HCOOH for stopping PI: 13% NaOCl (pH =12.6) for etching, 1 M KI for stopping. Typical examples of both cases are shown in Fig. 6. For PET, the breakthrough usually occurs as a sudden jump in current to typically $\sim$ 100 pA, followed by a period of time in which the current fluctuates very strongly. If the etching is interrupted during this time, which can last for several minutes, the pores tend to close again. In the following time the current is more stable but does usually not increase significantly over a time period of tens of minutes. Only then a further increase in current is observed. In polyimide, the etching curve is close to what is expected from theory: At the breakthrough, first a current in the picoampere range is recorded,

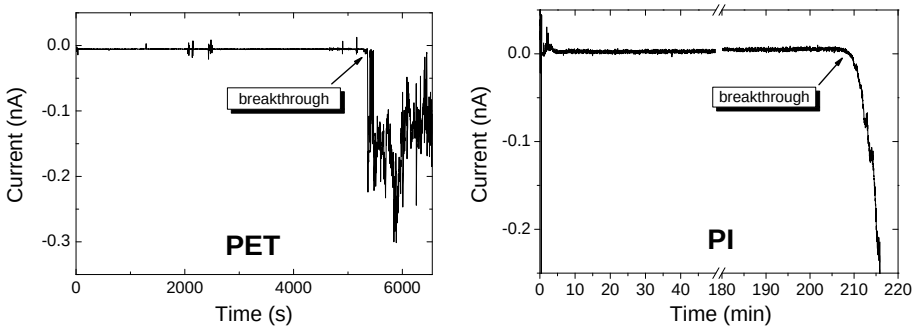

Figure 6. Typical etching curves for a) PET and b) polyimide. In both cases the breakthrough is clearly visible. The current is negative because a voltage of –1 V was applied during etching.

which then increases almost quadratically with time. These different behaviors are most probably due to the different chemical reactions occurring between etching and stopping solution after breakthrough. The stopping is extremely effective in the case of PET, where the pore diameter stays constant over a long time. The chemical reactions between NaOH and HCOOH are most likely responsible for the observed effects, since etching with only 1 M KCl as stopping solution leads to etching curves more similar to that of Kapton. The exact processes occurring soon after breakthrough are not yet fully understood. However, the PET pores used in this work were etched with the addition of 1 M HCOOH as stopping solution as shown in Fig. 5, because the main requirement was to obtain a pore size as small as possible.

2.2.2 *Etching parameters*

The choice of the etching solutions depends on the polymer as well as on the desired pore shape. NaOH is used for polyethylene terephthalate (PET) and polycarbonate (PC), whereas polyimide (PI) requires the use of NaOCl. To create the cylindrical pores in PC investigated in section 3.3, a solution of 5 M NaOH at 60 °C was used. Conical pores in PET have been etched with 9 M NaOH at room temperature, using a stopping solution of 1 M KCl + 1 M HCOOH. Tracks in Kapton were etched in as received 13% NaOCl (pH =12.6) at 55 °C, the stopping medium being 1 M KI, which acts as a reducing agent for the OCl^- ions. Under these conditions, the bulk etch rates as determined from thickness and weight reduction measurements are $\sim$ 1.6 nm/min for PET at 23 °C [31] and $\sim$ 7 nm/min for Kapton [47]. Typical etching times required for breakthrough of 12 µm thick foils are $\sim$ 1 h for PET and 3–4 h for PI.

This results in large pore openings of several hundred nm and 1–2 µm for PET and PI, respectively.

2.3 MATERIALS

The different polymers used here and some properties of the resulting pores are described now.

2.3.1 *Polycarbonate*

Polycarbonate (PC) is one of the most common polymers used for track-etching, due to its narrow pore size distribution (see section 3.3). Polycarbonate has the following chemical structure:

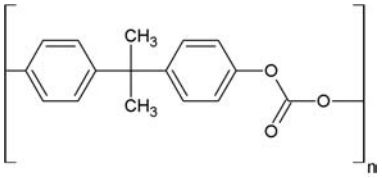

Typical etching conditions for the production of cylindrical pores are 6 M NaOH at 50 °C. The bulk etch rate of Makrofol KG (Bayer), 30 µm thickness (the material typically used here) is about 13 nm/min [48]; if a lower bulk etch rate is required (e. g., for controlled etching of single pores), 2 M NaOH at 60 °C is usually a good choice ($v_b \sim 2$ nm/min [48]). Conical geometries can be obtained by increasing the bulk etch rate either by the addition of 20–30% methanol to 9 M NaOH used at room temperature [49] or by applying higher voltages during the etching process [50].

A disadvantage of polycarbonate is its high hydrophobicity, which makes it difficult to use very small pores for applications in wet environments. Nevertheless, somewhat wider conical pores in polycarbonate have been used recently successfully for the detection of DNA molecules [51].

Since the commercial production of Makrofol was stopped by Bayer, it is important to investigate the etching properties of other polycarbonates. Pores in Pokalon (LOFO), which is the successor material of Makrofol, were reported to exhibit cigar-like pore shapes [52, 53]. On the other hand, pores in this material exhibit an extremely uniform pore size distribution, as determined by small-angle X-ray scattering (see section 3.3).

2.3.2 *Polyethylene terephthalate*

Since polyethylene terephthalate (PET) (Hostaphan RN 12, Hoechst, thickness 12 µm)

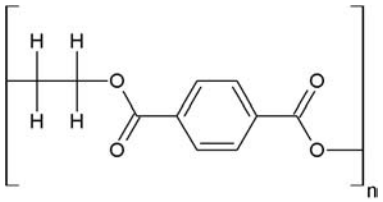

is more hydrophilic than PC, it is better suited for applications requiring very narrow pores. During the etching process, negatively charged carboxyl groups, which are attached to flexible polymer chains, are created on the pore surface. These flexible chains have been held responsible for voltage dependent ionic current fluctuations in PET pores similar to those occurring in biological ion channels, as it is predicted that their random thermal motions are modulated by the applied electric field [54]. The conical pores used here are etched with a 9 M NaOH solution at room temperature.

2.3.3 *Polyimide*

Etching of polyimide (Kapton 50 HN, DuPont, thickness 12.3 µm) has to be performed with a 13% NaOCl solution at 55 °C. Using the solution as received (pH =12.6) creates conical pores, while a solution with lower pH value (pH 8, buffered with boric acid) can be used to obtain quasi-cylindrical pores [55]. Kapton is ideal for applications requiring a stable ion current signal, such as single-molecule detection (see chapter 7). This results from the fact that they have a smoother surface than pores in PET due to the aromatic structure of polyimide (shown below for Kapton HN).

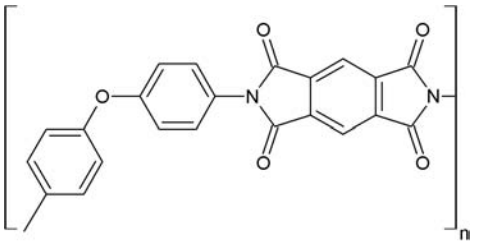

Therefore, the carboxyl groups, which are also created on the pore walls during etching, are directly fixed on the pore surface and do not disturb the ionic current [47].

Fig. 7 shows examples of the polymer foils typically used here, with diameter 3 cm. The different materials presented are, from left to right: polyimide, polyethylene terephthalate and polycarbonate.

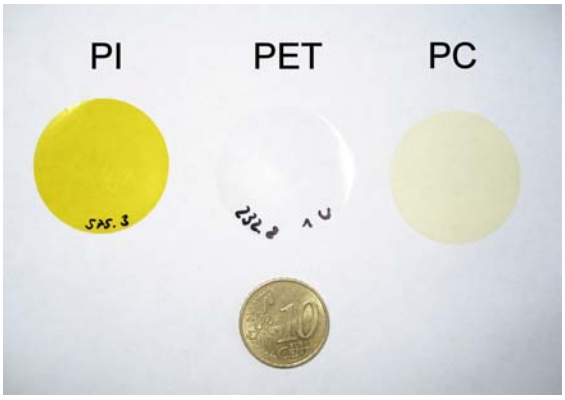

Figure 7. Examples of the different polymer foils used for track-etching.

3 GEOMETRICAL CHARACTERIZATION OF PORES

For any application or theoretical description of the nanopores, it is important to know their real shape and dimensions as precisely as possible. There are a variety of methods which can be used to obtain this information, including different imaging methods (e. g., scanning electron microscopy (SEM), transmission electron microscopy (TEM), atomic force microscopy (AFM)...), conductance measurements, size exclusion techniques, scattering experiments or pore shape replication by template methods.

Electrolytic measurements (section 3.1) (for conical pores in combination with SEM imaging (section 3.2.1)) are used here on a regular basis, deducing the size of single pores from their conductance.

An alternative method to access the pore size and pore size distribution is small-angle X-ray scattering (SAXS) (section 3.3) on membranes containing a large number of pores. The pores are acting as scattering objects for the X-rays and a mean pore size can be deduced from the scattering patterns. If a theoretical model for the description of the data is available, it is possible to obtain additional information about the inner shapes of the pores, in contrast to all microscopy techniques, which only access the surface of track-etched membranes. SAXS is non-destructive and a single measurement gives information about a whole pore ensemble. It has been applied here to investigate the effect of a UV irradiation prior to etching on the pore size distribution in different polycarbonate types. A narrow pore size distribution is certainly of importance for applications using many-pore samples such as filtration, but it is as well relevant for all single-pore applications, since it increases the reproducibility of pore production.

3.1 CONDUCTOMETRY

A quick and easy method to determine the diameter of track-etched pores is based on their ionic conductance. The resistance of a pore is determined by measuring the electric current flowing through at a given voltage. Assuming a certain geometry and knowing the conductivity of the electrolyte used, the size of the pores can be calculated.

3.1.1 *Cylindrical pores*

For a cylindrical pore, this calculation can either be performed simultaneously with the etching process, if the specific conductivity κ of the

etching solution is known, or at a later stage using KCl solution of a known conductivity.

The resistance R of a cylinder with diameter d and specific conductivity κ is given by

$$R = \frac{U}{I} = \frac{4L}{\pi d^2 \kappa}\,, \tag{3.1}$$

which leads to

$$d = \sqrt{\frac{4LI}{\pi \kappa U}}\,, \tag{3.2}$$

where L is the length of the pore, corresponding to the foil thickness.

3.1.2 *Conical pores*

For conical pores etched with a stopping solution on one side, the pore size cannot be determined simultaneously during etching, due to the different conductivities of etching and stopping solution and their mixing after the breakthrough. It has to be calculated in a second step, by substituting the solutions on both sides of the membrane with KCl solution of a known conductivity. Formula (3.1) has to be slightly modified, taking into account the conical geometry with two different diameters on both sides (Fig. 8):

$$d = \frac{4LI}{\pi \kappa U D}. \tag{3.3}$$

Although this solution is not exact due to curved equipotentials inside

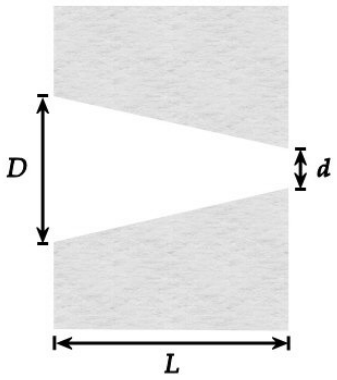

Figure 8. Dimensions of a conical pore.

a conical pore, it is a good approximation for small opening angles as fulfilled here [56]. The access resistance R_a of the pore (the resistance

along the convergent paths from the bulk medium to the pore opening [1]), which gives a significant contribution to the total resistance especially for short channels and can be calculated [57] by

$$R_a = \frac{1}{4\kappa r}, \tag{3.4}$$

is small compared to the pore resistance and is therefore neglected here. As can be easily derived by trigonometry from Fig. 3, the large opening D can be calculated from the bulk etch rate and the etching time, taking into account the thickness reduction of the foil during the etching process, via

$$D = 2tv_b\sqrt{\frac{v_t - v_b}{v_t + v_b}}. \tag{3.5}$$

For $v_t \gg v_b$ Eq. (3.5) is approximated by $D = 2tv_b$.

Alternatively, D can be measured by electron microscopy (see section 3.2.1). For this purpose a sample containing 10^7 pores/cm^2 is etched simultaneously with the single pore, using a cell consisting of three chambers, of which the middle one contains the etchant and is open to the left as well as to the right (Fig. 9).

All the parameters used in the above equations (3.2) and (3.3) are subject to uncertainties, resulting in a typical error for diameters determined by conductivity measurements of approx. 10%.

3.2 SCANNING ELECTRON MICROSCOPY

3.2.1 *Conical pores*

To be able to determine the size of the small opening of a pore from its conductivity, it is necessary to know its diameter at the base of the cone. For most applications it is of interest to know these values before starting the measurements. But since drying, mounting on a sample holder, and sputtering gold will usually make the pore useless, recording a SEM picture of the pore is not feasible before an experiment such as single-molecule detection. On the other hand, imaging the pore can sometimes be helpful to detect variations in the bulk etch rate, which may otherwise go unnoticed especially in the case of polyimide etching with NaOCl due to steady degradation of the solution. Although the bulk etch rate could be determined individually for each sample by measuring the thickness reduction of the foil, this requires also complete drying to avoid an underestimation caused by swelling of the material in wet state and will not be very precise. A simple method to obtain a value for the large diameter of a pore without imaging it, is to etch simultaneously (Fig. 9) a foil containing a larger number of latent tracks, but irradiated under the same conditions as the single-track foil. The single-pore diameter can

then be estimated based on the average diameter of several pores in this foil.

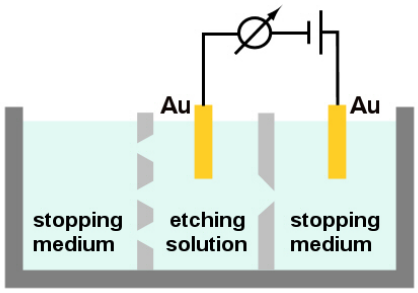

Figure 9. Simultaneous etching of single- and many-pore samples.

Comparison with images of single pores have shown that the diameter of the single pore is usually in good agreement with the average value obtained from a sample containing 10^7 pores/cm^2 (Fig. 10).

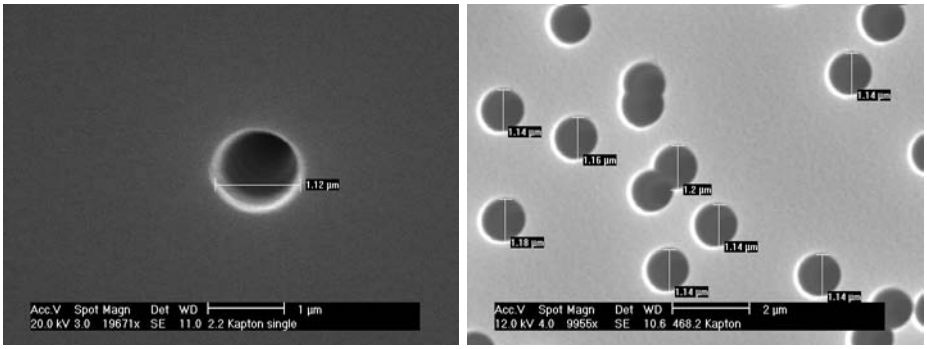

(a) (b)

Figure 10. a) Sample #2.2: single pore in polyimide b) Sample #468.2: membrane with 10^7 pores/cm^2 etched simultaneously with the single pore membrane in a).

In order to locate the single pore in the SEM, the area exposed to the beam during ion irradiation (200 µm diameter) is marked after the etching procedure by sputtering gold onto the sample, using the same mask as for irradiation. A thinner gold layer is sputtered afterwards on the whole sample, to create the conductive surface needed for imaging.

3.2.2 *Cylindrical pores*

Recent SEM investigations of cylindrical pores revealed a special pore geometry problem. A comparison between SEM images and data obtained by conductometry, replica methods, and SAXS gave indications that pores in polycarbonate and PET are wider inside than measured at the surface with SEM. This might be a problem also when determining the large diameter of conical pores by SEM. The most likely cause is the presence of a constriction of the pore close to the surface, but other possibilities have yet to be ruled out, such as differences between the wet and dry states of the polymer membrane, closing of the pores by the gold layer sputtered on the membrane for imaging, or other systematic errors related to SEM imaging. Indeed, recent SEM images of metallic wires grown inside cylindrical track-etched polycarbonate templates showed a tapering of the pores over the last micrometer. A similar effect is known for commercially available track-etched membranes in polycarbonate [52], for which it has been suggested that this shape is caused by an inhomogeneous damage along the track, due to the fact that regions near the surface are exposed to a smaller number of secondary electrons than those in the center of the membrane. More recently, 'candle-shaped' pores were also observed in polyimide [58]. There, the effect was attributed to surface layers of 2–3 µm thickness with different chemical properties, originating from the manufacturing process. If this could be also the case for the polymers used here can be tested by pre-etching samples before the irradiation, to remove such a surface layer. An alternative explanation for a constriction near the membrane surface are surface tension effects.

PORES IN PC Track-etched polycarbonate membranes were used as templates for copper wire growth[1]. The diameters of the wires fabricated in the template and the pore openings as obtained from SEM were analyzed. Fig. 11 compares the pore diameters at the surface with mean wire diameters for different etching times. It can be seen that the wire diameters are systematically larger than the pore openings. The difference between both first increases with increasing diameters, but then reaches a constant value of about 280 nm. The values obtained for the wires are in good agreement with those of single cylindrical pores determined by conductometry as well as those obtained by means of Faraday's law from the deposited charge during the growth of single wires [48].

PORES IN PET A similar observation was made with cylindrical pores in PET. They were produced by etching single- and many-track membranes simultaneously in a large vessel. Afterwards, the diameters of the single pores were determined by conductivity measurements, those of the many-pore samples by SEM. Again, the values obtained by SEM

1 Experiments performed by M. Quiliot during his practical training at GSI.

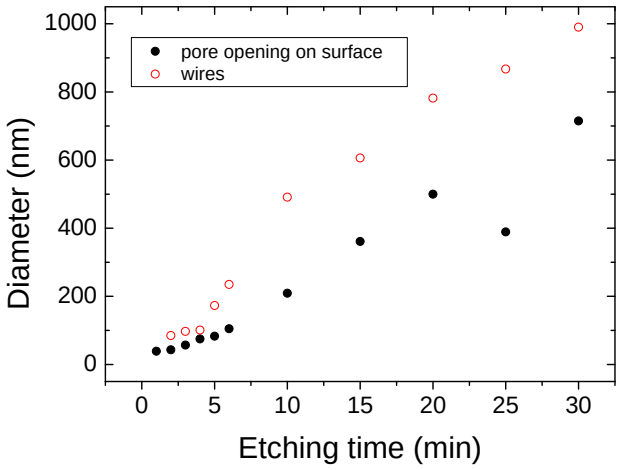

Figure 11. Diameters of pore openings in PC and of wires grown in templates etched simultaneously, as determined by SEM. The diameters of the wires are systematically higher than those of the pore openings.

were found to be systematically lower than those from the conductivity measurements, this time by about 100 nm (see Fig. 12). The errors for the values from conductivity measurements are estimated to be $\pm 10\%$, while those for the SEM measurements result from the standard deviation of the measurement of 20 pores for each etching time.

From these results, it seems to be unlikely that the gold layer sputtered on top of the membrane is the reason for the smaller SEM diameters, because the small pores in Fig. 11 would then rather be closed than reduced by only a small value.

In order to obtain precise values for the pore diameters, this effect has to be further examined, particularly with regard to conical pores.

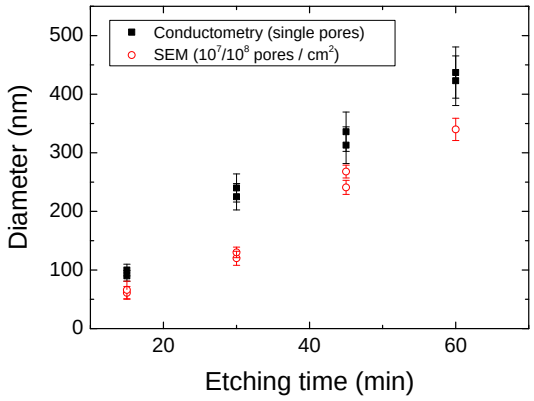

Figure 12. Diameters for single- and many-pore PET membranes etched simultaneously. Values for single pores obtained by conductivity measurements, for many-pore samples by SEM. Two samples of single- and many-pore membranes were etched and measured for each time.

3.3 SMALL-ANGLE X-RAY SCATTERING

Small-angle X-ray scattering (SAXS) is the elastic scattering of monochromatic X-rays at small scattering angles. As for all diffraction processes, the size of the diffraction image behaves inversely to the size of the diffracting object. This means that relatively large objects like colloid particles or macromolecules scatter the incoming beam only by a small angle. Since X-rays are scattered due to interaction with electrons, the observed diffraction pattern contains information about the electron distribution in the sample.

If the X-rays are scattered by an object of a size comparable to the wavelength, the phase shift g under small scattering angles for waves scattered from different points in this object is always much smaller than the wavelength (Fig. 13(a)). Therefore structures in this size region are not influencing the intensity distribution at small angles.

On the other hand, for an object much larger than the wavelength (Fig. 13(b)), two waves scattered from different points of the object can have phaseshifts of several wavelengths for the relatively large angles of a few rad, leading to complete cancellation if the waves scattered from all points of the object are added up. For smaller scattering angles also constructive interference of all these waves is possible, when the maximum phaseshift is below one wavelength, leading to the observed intensity patterns at small angles. The maximum intensity is reached for forward scattering at zero angle, where all scattered waves are in phase [59].

The particle size range in which SAXS is applicable is limited upwards

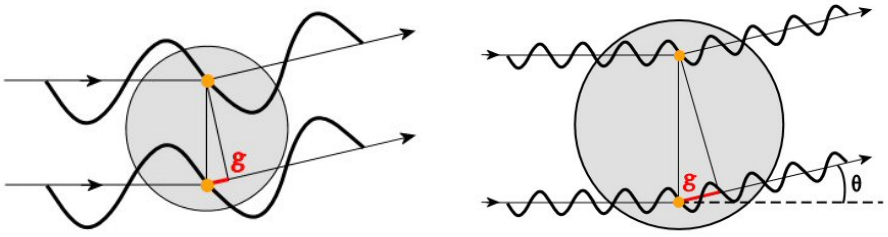

(a) (b)

Figure 13. a) Scattering of X-rays under small angles from an object of dimension similar to the wavelength. b) Scattering of X-rays on an object of dimension bigger than the wavelength.

by the smallest angles accessible by the experimental setup and downwards to sizes of the order of several wavelengths, where the scattering is very wide but also very weak [60].

3.3.1 *Theoretical background*

A general scheme of a scattering experiment can be seen in Fig. 14.

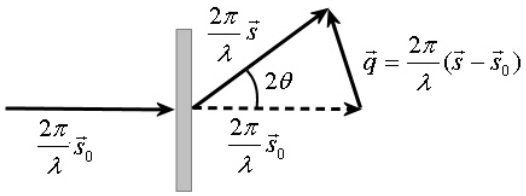

Figure 14. Schematic of a scattering experiment.

The parameter used to describe the scattering process is the momentum transfer $\vec{q}$, being the difference between the incoming and outgoing wave with wave vectors $\frac{2\pi}{\lambda}\vec{s_0}$ and $\frac{2\pi}{\lambda}\vec{s}$ respectively. The magnitude of $\vec{q}$ is

$$|\vec{q}| = \frac{4\pi}{\lambda}\sin\theta. \tag{3.6}$$

For small angles this becomes

$$|\vec{q}| \approx \frac{4\pi}{\lambda}\theta. \tag{3.7}$$

The amplitude A of the scattered wave is the Fourier transform of the contrast function $\rho(\vec{r})$ of the scattering object, which is given by its

electron density for X-rays. Therefore,

$$A(\vec{q}) = \int_{-\infty}^{+\infty} \rho(\vec{r}) e^{-i\vec{q}\vec{r}} \, \mathrm{d}^3\vec{r}. \tag{3.8}$$

The intensity $I(\vec{q})$ measured in an experiment is

$$I(\vec{q}) = A(\vec{q}) \cdot A^*(\vec{q}) = |A(\vec{q})|^2 . \tag{3.9}$$

The amplitude is proportional to the number of scattering centers per volume. For samples without long-range ordering, the amplitude reaches a constant value at large angles, which is proportional to the mean density of the whole sample. For small angles, it depends only on local density variations [61]. In the case of SAXS one observes local changes in electron density.

But as in optics (Babinet's principle) one can not distinguish between positive or negative density variations [62], this information has to be deduced by other means. For track-etched pores, it is clear that the electron density inside the pores has to be lower than in the bulk material, since the material has been removed inside the pores.

3.3.2 *Cylinder model*

To model the scattered intensity, a certain geometry for the scattering object has to be assumed. The pores investigated here are assumed to be of cylindrical shape (Fig. 15), which is known to be a good approximation from nanowires grown inside such pores [63].

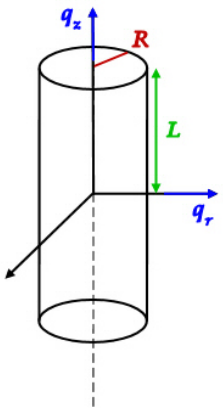

Figure 15. Track-etched pore modeled as a cylinder.

To get the scattered intensity in this case, one has to calculate the

Fourier transform of a cylinder. The mean amplitude is [61]

$$\bar{A}(\vec{q}) = \int_{-\infty}^{+\infty} \Delta\rho(\vec{r}) e^{-i\vec{q}\vec{r}}\, \mathrm{d}^3\vec{r}, \tag{3.10}$$

where $\Delta\rho$ is the deviation from the mean electron density in the sample. Due to the rotational symmetry of the pore, it is helpful to use cylindrical coordinates. The deviation from the mean electron density is assumed to be constant ($\Delta\rho = C$) in the pore and zero outside. Under these conditions, Eq. (3.10) becomes

$$\bar{A}(\vec{q}, R, L) = 2\ \pi\ C\ L\ R^2\ \frac{\sin(q_z L)}{q_z L}\ \frac{J_1(q_r R)}{q_r R}, \tag{3.11}$$

where

- L half length of the cylinder
- R radius of the cylinder
- J_1 first-order Bessel function
- q_r radial component of $\vec{q}$
- q_z longitudinal component of $\vec{q}$

The full deduction of this formalism can be found in [61].

As an example, in Fig. 16 the intensity for a cylinder with radius $R = 50$ nm and half length $L = 15$ µm is shown, calculated with the program PXY7 [64], which was also used to fit the experimental data. The scattered intensity would look like this, if all pores were of exactly the same size and shape.

An easy way to determine the radius of gyration R_g[2] of a scattering object is to use Guinier's law, which expresses that the scattered intensity can be approximated for small q by a Gauss function

$$I(\vec{q}) = I_0 e^{-cR_g^2 q^2}. \tag{3.12}$$

Therefore, R_g can be determined from the slope of the plot of the logarithm of $I(\vec{q})$ against q^2.

For the cylinder model, one can expand the radial part of the scattered amplitude (the Bessel function) in a MacLaurin series, giving

$$\bar{A}(\vec{q}, R, L) = 2\ \pi\ C\ L\ R^2\ \frac{\sin(q_z L)}{q_z L}\ \left[1 - \frac{R^2 q_r^2}{8} + \frac{R^4 q_r^4}{192} - \ldots\right]. \tag{3.13}$$

This series can be approximated for small q by an exponential function [65]:

$$\bar{A}(\vec{q}, R, L) = 2\ \pi\ C\ L\ R^2\ \frac{\sin(q_z L)}{q_z L}\ e^{-\frac{R^2 q^2}{8}}. \tag{3.14}$$

2 R_g is, in analogy with classical mechanics, the mean square of distances of the scattering electrons from the electronic center of mass of the scattering object [59, 60].

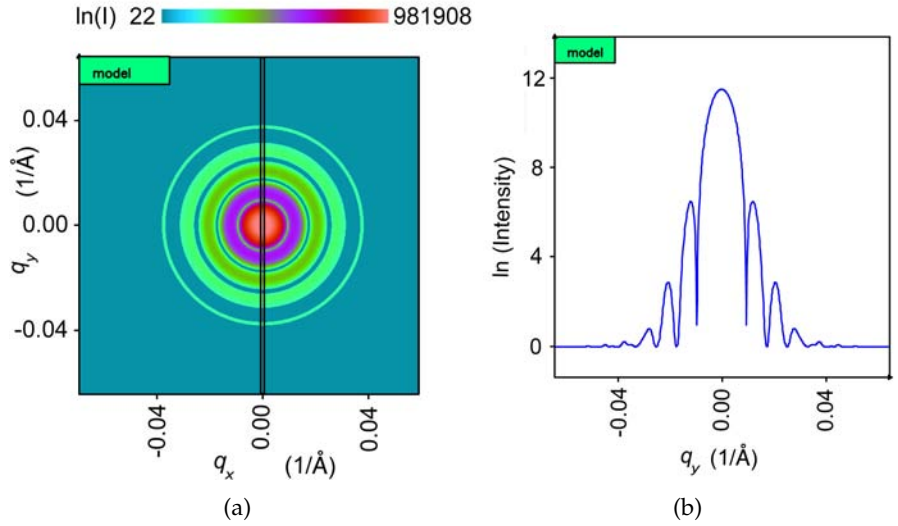

Figure 16. a) Modeled scattering intensity for a cylinder with radius $R = 50$ nm and half length $L = 15$ µm b) Intensity for the pixels lying inside the vertical filter shown in a) projected against q_y.

Therefore the scattered intensity becomes

$$I(\vec{q}, R, L) = 4\,\pi^2\,C^2\,L^2\,R^4\,\frac{\sin(q_z L)^2}{(q_z L)^2}\,e^{-\frac{R^2 q^2}{4}}. \tag{3.15}$$

In this case the radius of gyration is corresponding to the radius of the cylinder.

However, for the evaluation of the following experiments, the original amplitude function containing the Bessel function was used due to the good quality of the scattering data also for larger q.

3.3.3 *Experimental conditions*

As mentioned earlier, one aim of this study was to examine the positive effect of UV irradiation prior to etching on the pore size distribution of track-etched membranes. This is a treatment which is widely used to enhance preferential etching of ion tracks [66–68]. Another goal was to compare different types of polycarbonate with respect to their suitability for track-etching applications.

The membranes investigated here were two different types of amorphous polycarbonate foils, 30 µm thick Makrofol KG (Bayer) and 20 µm thick Pokalon OG (LOFO). They were irradiated at the linear accelerator UNILAC of GSI (Darmstadt, Germany) with Xe ions of 1.4 GeV total energy. The range of these ions is more than 150 µm and thus much

larger than the foil thickness, ensuring an almost constant energy loss throughout the sample. Pieces of a few cm² in size were exposed normal to the surface to fluences of $3{\cdot}10^8$, $5{\cdot}10^8$, and $1{\cdot}10^9$ ions/cm². Subsequent to the ion irradiation, half of the samples were exposed to UV light for 1 h from each side.

To etch the samples, 5 M aqueous NaOH at 60 °C was used. The etching duration was 3, 5, and 8 min, producing pore diameters between $\sim$ 60 and 340 nm.

The scattering experiments were performed at the ID01 beamline at the ESRF synchrotron (Grenoble, France) with a monochromatic X-ray beam of $\lambda = 0.088$ nm. The position sensitive detector was a Princeton CCD camera with 1242 x 1152 pixels of 63.3 µm² each. The sample-detector distance was variable, and distances of 0.7, 2.0 and 4 m were used. To improve the flatness of the samples and avoid a tilting of the tracks against each other, each foil was covered by a 10 µm thick mica sheet. The samples were mounted on a goniometer head and could be adjusted in the vertical and horizontal axes (Fig. 17).

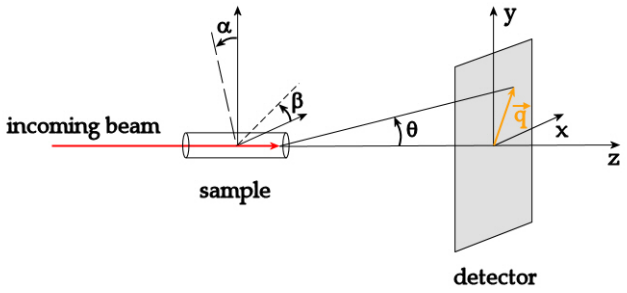

Figure 17. Schematic view of the SAXS setup. θ is the scattering angle, α and β denote a rotation of the sample around the horizontal (x) or vertical (y) axis, respectively.

Due to the high aspect ratio of the pores, a precise alignment of the channel axis against the X-rays is necessary—small variations in the orientation influence the scattering pattern enormously (see Fig. 18) [69]. A rotationally symmetric intensity distribution is obtained, when the channels axis is parallel to the incoming beam (see Fig. 16). For each sample, its position was first scanned around the horizontal axis until the scattering pattern became symmetric in the horizontal plane. Then scattering images were recorded for a number of different angles against the vertical axis.

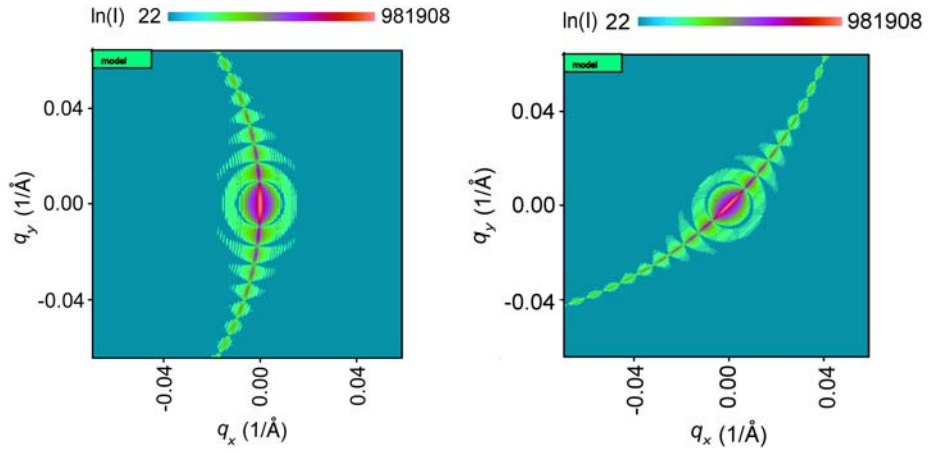

(a) (b)

Figure 18. Calculated scattered intensities for a) cylinder turned around the vertical axis by $\beta = 1°$ b) cylinder turned around the horizontal and the vertical axis by $\alpha = \beta = 1°$ each; to be compared with Fig. 16, where $\alpha = \beta = 0°$.

3.3.4 *Fitting procedure*

To analyze the scattering data, the measured intensity distribution has to be compared with calculations, assuming a certain size and geometry of the pore—here the cylinder model described in section 3.3.2 was used. Since the samples are expected to have a certain radius dispersion, a function taking this into account had to be included in the model. This induces a damping increasing with q in the otherwise undamped oscillations of the Bessel function. In order to improve the fitting quality, the angular resolution of the beamline had to be taken into account. This has the effect of a constant damping with q. Finally also a length dispersion was included, since the foil thickness can show variations over the area of a sample.

The radius and length dispersion can be included in the formula for the scattered intensity, yielding

$$I(\vec{q}, R_0, L_0) = \int_0^\infty p_{Rln}(R_0, R)\,\mathrm{d}R \int_0^\infty p_{LG}(L_0, L)\,\mathrm{d}L\,|A(\vec{q}, R, L)|^2\,, \quad (3.16)$$

where p_{LG} is a Gaussian and p_{Rln} a log normal distribution.

It was checked that the final set of parameters gives good fits for all angles between the pore axis and the primary X-ray beam.

To keep the amount of calculation reasonable, the analysis was based on data sets with the pore axis tilted by a few degrees against the X-ray

beam, resulting in anisotropic scattering patterns similar to the one in Fig. 18(a). For the fits, values from pixels lying inside two narrow rectangular filters (one vertical, one horizontal) were used (Fig. 19). The value plotted against q is the total intensity of all pixels belonging to a certain q value inside the chosen filter.

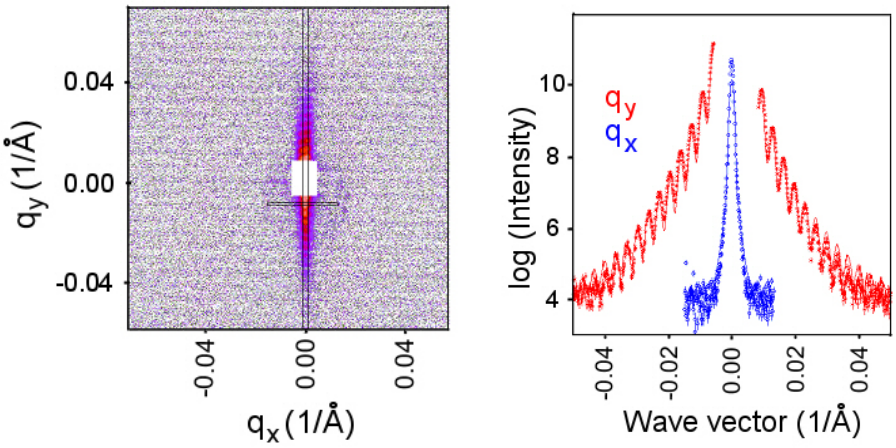

(a) (b)

Figure 19. Example for data analysis on Pokalon, $3 \cdot 10^8$ ions/cm², etched for 8 min, UV irradiated, sample tilted by 4.5° around the horizontal axis a) Scattered intensity recorded with a position sensitive detector b) Intensity inside the vertical and horizontal filters shown in a) plotted against q; fits are also included.

3.3.5 *Results*

Pore radii

The pore radii of the different samples were deduced using the model described above. In the current stage of development the software does not yet provide error values for the extracted radii. The results for the set of samples irradiated with a fluence of $3 \cdot 10^8$ ions/cm² are shown in Fig. 20(a). Both investigated materials show a linear etching behavior, but it turned out that Makrofol has a higher bulk etching rate, resulting in pore radii between 60 and 170 nm for Makrofol and between 30 and 90 nm for Pokalon. The results for the UV treated and non-treated samples are both shown in Fig. 20(a), yielding no significant influence of the UV irradiation on the pore size.

As already mentioned, SAXS gives information about the bulk properties of the sample, while SEM probes the sample surface. Since we suspect the pore diameter of cylindrical pores to be larger in the bulk than at

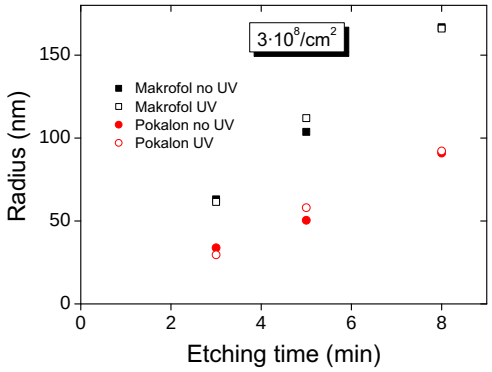

(a)

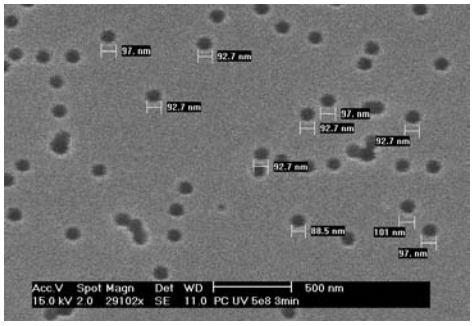

(b)

Figure 20. a) Pore size determined by SAXS as a function of etching time for Makrofol and Pokalon irradiated with $3{\cdot}10^8$ ions/cm² and etched in 5 M NaOH at 60 °C with (empty symbols) and without (filled symbols) UV treatment b) SEM picture of Makrofol, $3{\cdot}10^8$, 3 min etched, UV irradiated. The SEM picture yields a mean radius of 47 nm, compared to a value of $r = 65$ nm as extracted from SAXS.

the surface (see sections 3.1.1 and 3.2.2) all samples were additionally imaged by electron microscopy (example in Fig. 20(b)) to compare the thus obtained radii to the values measured by SAXS. The results for the UV irradiated set of samples are presented in Fig. 21 for Makrofol and Pokalon for $3{\cdot}10^8$ ions/cm² (a) and $5{\cdot}10^8$ ions/cm² (b). Again, the radii measured by SEM (errors are standard deviation of 20 measurements) are significantly smaller than those obtained by SAXS.

Because the value obtained by SAXS is a mean value over the whole pore length, this is another indication that the pores indeed have a constriction close to the surface rather than being smaller over the whole length when in dry state, since the samples used for SAXS were also dried. Nevertheless, SAXS measurements on wet as well as on metal filled samples are in preparation to fully clarify this issue.

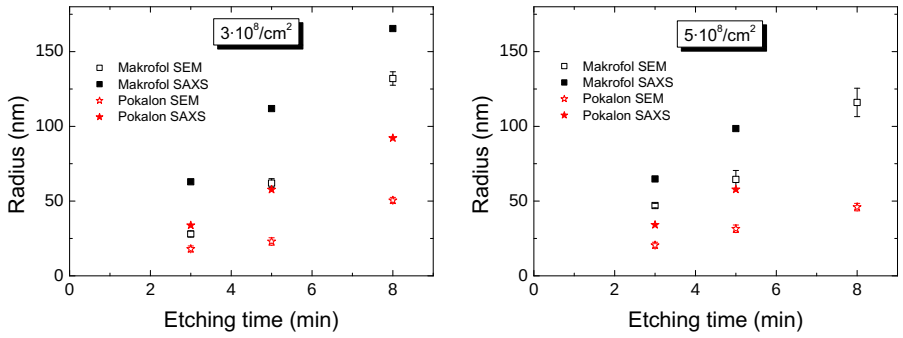

Figure 21. a) Pore size as a function of etching time for Makrofol and Pokalon irradiated with (a) $3{\cdot}10^8$ ions/cm² (b) $5{\cdot}10^8$ ions/cm², etched in 5 M NaOH at 60 °C with and without UV treatment.

Pore size distribution

A clear beneficial effect of UV irradiation on the pore size distribution (recognizable by more pronounced oscillations for samples with UV treatment) was detected for the majority of the samples. The effect of the UV treatment on the scattering images is presented in Fig. 22 for a Pokalon sample with a pore density of $3{\cdot}10^8$/cm², etched for 5 min. The curve with the more pronounced oscillations of the Bessel function belongs to the sample irradiated with UV light prior to the etching. For the non-UV treated sample, the oscillations are much more damped, as a result of a broader pore size distribution. This effect is also visible in the SEM pictures, shown in Fig. 23 for Makrofol, $5{\cdot}10^8$ pores/cm², etched for 8 min. The UV treated sample is shown on the left, yielding a quite narrow pore size distribution. The image of the corresponding sample without UV irradiation is shown on the right. A variety of different pore sizes are visible here of which some especially small pores are indicated by the arrows.

The beneficial effect of UV treatment was found to be most pronounced in Pokalon, where all SAXS spectra of the UV irradiated samples could be fitted without introducing a radius dispersion, whereas in the case of Makrofol a radius dispersion was needed also for some of the UV treated samples [70].

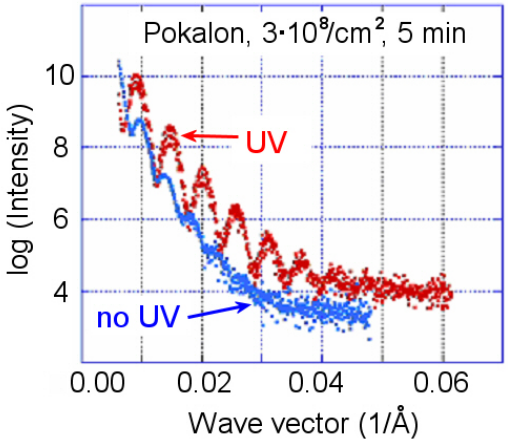

Figure 22. Effect of UV irradiation before etching on the SAXS patterns shown for Pokalon, $3{\cdot}10^8$ pores/cm², etched for 5 min. The oscillations of the Bessel function are much more damped for the sample without UV irradiation, indicating a broader pore size distribution.

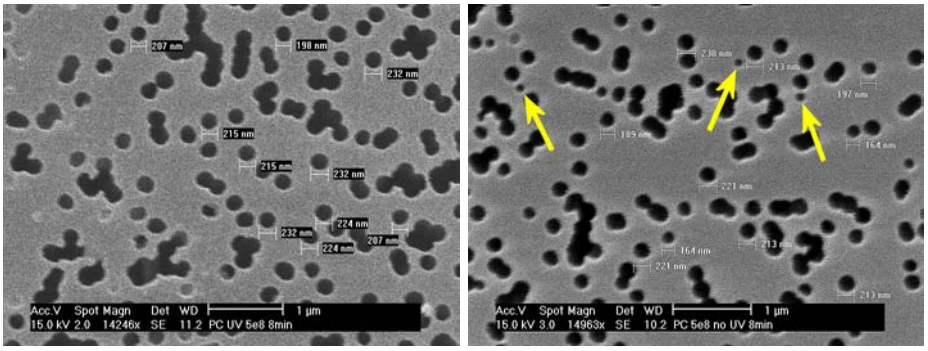

(a) (b)

Figure 23. SEM images of Makrofol samples, $5{\cdot}10^8$ pores/cm², etched for 8 min a) with UV irradiation before the etching b) without UV irradiation. The pore size distribution in the non-UV treated sample is less uniform, arrows indicate examples of very small pores.

4

ASYMMETRIC I-V CURVES OF SINGLE CONICAL NANOPORES

In biology, ion channels with asymmetric $I - V$ characteristics are a well known phenomenon [1]. Their behavior is also called 'rectifying', because they transport more ions in one direction than in the other. An example of these are the inwardly rectifying potassium channels [71, 72], which transport potassium effectively into, but not out of the cell. Surprisingly, it has been found that synthetic, conical, charged nanopores can also show this characteristic. Among the systems showing this feature are conical track-etched nanopores (which are negatively charged at neutral pH due to the presence of carboxyl groups on the pore surface created during the track-etching process, see section 2.3) [31], asymmetric pores in Si_3N_4 [21], gold nanotubes [27], quartz nanopipettes [73, 74] or asymmetrically functionalized single-wall carbon nanotubes [75].

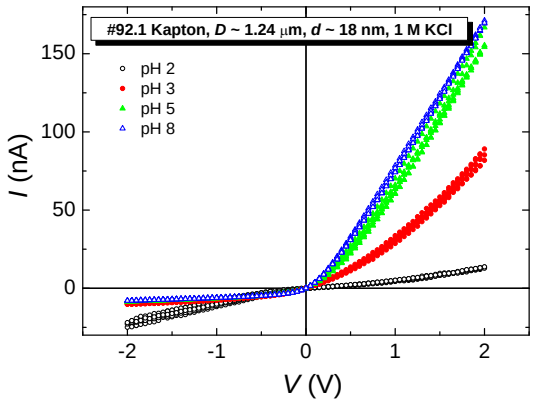

Figure 24. $I - V$ curve of a track-etched conical pore in polyimid recorded in 1 M KCl of different pH value. For neutral pH, the carboxyl groups at the pore walls are negatively charged, resulting in a high rectification ratio. At low pH they become protonated and the rectification vanishes.

In all these systems the rectification properties depend on the pH value of the electrolyte used, suggesting that the charges on the pore walls are responsible for the effect. This has also been demonstrated experimentally by tuning the charge either chemically or physically [27, 74, 76], leading to changes in the $I - V$ characteristics. Neutral pores did not rectify the ion current, while positively and negatively charged pores rectify the current in opposite directions [27]. An example of this pH dependence

is shown in Fig. 24 for a conical track-etched pore in polyimide, whose pore walls are negatively charged at neutral pH (COO^-) and become neutral at low pH, where the carboxyl groups are protonated (COOH). It is clearly seen that the negatively charged pore rectifies the ionic current while the neutral one does not. The same behavior is also found with PET pores [77].

Additionally, a broken symmetry in the electro-chemical potential of the pore is required, which can not only be provided by the geometrical shape of the pore, but also by an asymmetric charge distribution along the pore axis [78], which can be achieved for example by exposing the two openings of a cylindrical pore to electrolytes of same concentrations but different pH values.

Such an asymmetric charge distribution along the pore axis leads to an asymmetric electrostatic potential inside the pore, called the 'intrinsic' potential, because it is independent of an external voltage, which is then superimposed, leading to different potential shapes for different polarities. The shape of the intrinsic potential of a conical negatively charged nanopore is shown schematically in Fig. 25. Several mathematical mod-

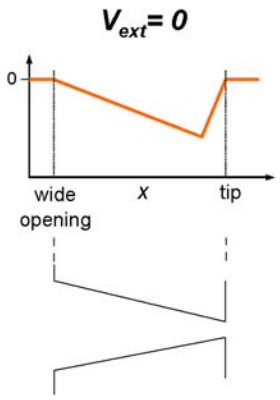

Figure 25. Scheme of the intrinsic electric potential of a conical, negatively charged nanopore. Not drawn to scale.

els have been developed to explain the rectification behavior of these systems, of which a comprehensive review can be found in [32]. The most prominent of these focus either on the asymmetric ratchet-like potential inside the pore [32, 33, 79], which leads to the formation of a cation trap and therefore lower current for one polarity of the applied voltage (see Fig. 26), or they explain the different currents for different polarities by concentration changes inside the pore [34, 80–83].

The experimental data presented in sections 4.14 and 5.2 have been compared with calculations performed with a simple continuum model based on the Poisson-Nernst-Planck (PNP) equations, developed by J. Cervera and P. Ramírez [34, 80]. This model uses surface charge as the

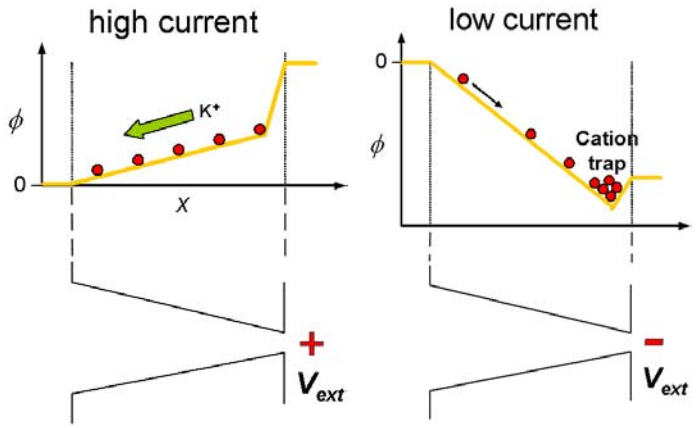

Figure 26. Resulting potential inside a conical negatively charged nanopore for a) positive external potential b) negative external potential. The formation of a cation trap for negative potentials is illustrated.

only free parameter and is able to reproduce the experimental results semiquantitatively, although some of the assumptions made (e. g., its use of bulk diffusion coefficients, use of concentrations in nanometer sized systems which could hold a small number of ions) have been questioned [32, 78, 84].

The shape of the potentials calculated by both the ratchet and PNP models are asymmetric, and depend strongly on the charges present on the pore walls, as thus do the $I - V$ characteristics. The effect of these surface charges on the electric potential is moderated by their screening by mobile ions (i. e., the thickness of the electrical double-layer at the pore wall). Since the thickness of this double-layer is influenced by the electrolyte concentration, the $I - V$ characteristics should depend strongly on this parameter, if electrostatic interactions are responsible for the rectification effect.

For lower salt concentrations, the electrical double-layer at the pore walls is thicker, i. e., fewer counter-ions are screening the surface charges, so their effect is more pronounced. Therefore, one would expect that lowering the electrolyte concentration will enhance the rectification effect. A systematic study of this dependence has been performed here (published in [85]). These measurements were done primarily on PET pores, which were also of interest since they have similar transport properties as biological channels, such as ion-current fluctuations [32].

4.1 EXPERIMENTAL SETUP

Measurements of the $I - V$ curves discussed in the following chapters were performed in an electrolytic cell similar to that used for etching (see section 2.2.1). Shielding from electrical interference was achieved by inserting the cell into a grounded matching stainless steel box (Fig. 27). Homemade Ag|AgCl electrodes were used for the experiments, chlorided

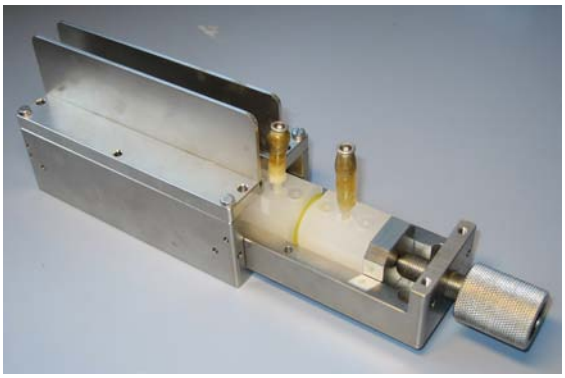

Figure 27. Photograph of the cell used for etching as well as for $I - V$ measurements.

in 0.1 M HCl at 0.4 V for 4 h or in 1 M NaCl at 2 V for 10 min. Ag|AgCl electrodes are usually used for precision measurements, because they have stable and reproducible equilibrium potentials. If they are used in an aqueous environment containing chloride ions, the following reaction takes place: $\mathrm{AgCl(s)} + \mathrm{e^-} \rightleftharpoons \mathrm{Ag(s)} + \mathrm{Cl^-(aq)}$.

To obtain the $I - V$ curve of a pore, a triangular voltage signal composed of 100 mV steps has been applied at the narrow side of the pore (Fig. 28). Its frequency was 0.005 Hz, which is low enough to avoid capacitance spikes[1] and the system can be regarded as adiabatic [54, 86]. Data were recorded with two different systems: either with a National

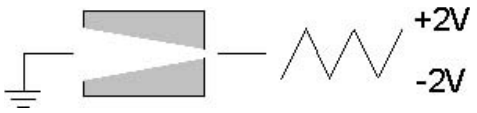

Figure 28. Setup for recording $I - V$ curves of conical pores.

Instruments DA/AD card generating the voltage signal and reading back the output of a Keithley 616 picoamperemeter, or with a GPIB controlled Keithley 6487 picoamperemeter with integrated voltage source.

1 The thin polymer foil has a relatively large capacitance through which a current pulse flows when the voltage is changed suddenly. The $I - V$ curves recorded here with low-frequency voltage signals are not influenced by the capacitance.

Fig. 29 shows an example set of current and voltage measurements, together with the corresponding $I - V$ curve and highlighting the associated directions of cation flow.

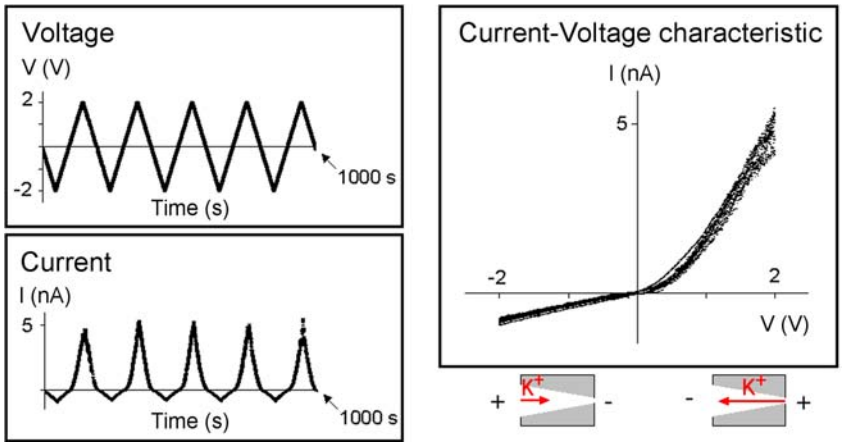

Figure 29. Applied voltage, current and corresponding $I - V$ curve of a conical nanopore. The arrows in the insets indicate the direction of cation flow.

Due to this nonlinear behavior of the $I - V$ curves, current-voltage pairs for the determination of the small pore diameter by conductivity measurements according to Eq. (3.3) have to be taken from the region close to the origin, in which the $I - V$ curve is ohmic.

4.2 CONCENTRATION DEPENDENCE OF CURRENT RECTIFICATION

To investigate the rectification as a function of concentration, measurements at KCl concentrations between 0.01 and 3 M were performed. Unbuffered KCl of pH $=5.6 \pm 0.2$ has been used, to avoid the introduction of additional ionic species into the system. The measurements were usually done starting with the highest concentration, then lowering it stepwise. Before each concentration change, the measurement cell was rinsed with deionized water and then again with the next electrolyte concentration to be used.

A measure of the degree of rectification is given by the ratio of absolute current values for positive and negative applied voltages $|I(V)|/|I(-V)|$. In the following, sets of $I - V$ curves parametric in the concentration are presented for two PET pores of different sizes (parts (a) of Figs. 30 and 31). The degree of rectification is shown as a function of the applied voltage for the different concentrations in parts (b). Error bars for $|I(V)|/|I(-V)|$ were obtained by the Gaussian error propagation law from the errors of $I(V)$. These are derived from the standard deviation of the mean value of current as measured for a certain applied voltage during several voltage

sweeps.

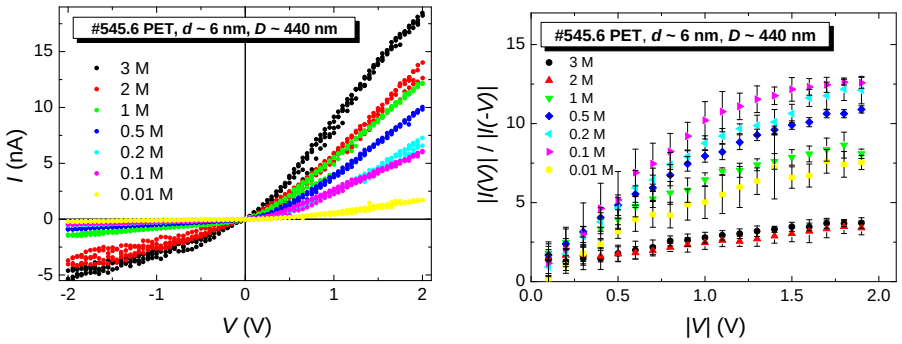

(a) (b)

Figure 30. a) Asymmetric $I - V$ curve of a conical PET pore with $d \sim 6$ nm and $D \sim 440$ nm for concentrations in the range 0.01–3 M KCl b) Variation of the degree of rectification with concentration.

For a discussion of the voltage dependence of the rectification strength, see section 4.3.2. As expected, the degree of rectification is very low for high concentrations and increases for decreasing concentrations. This is intuitively clear, because at high concentrations the surface charges are almost completely screened by mobile counter-ions, leading to an almost 'neutral' pore, while at lower concentrations the thickness of the double-layer increases and therefore the charges are less screened, leading to more asymmetric potentials and therefore higher rectification. The dependence of rectification on the concentration can be displayed in

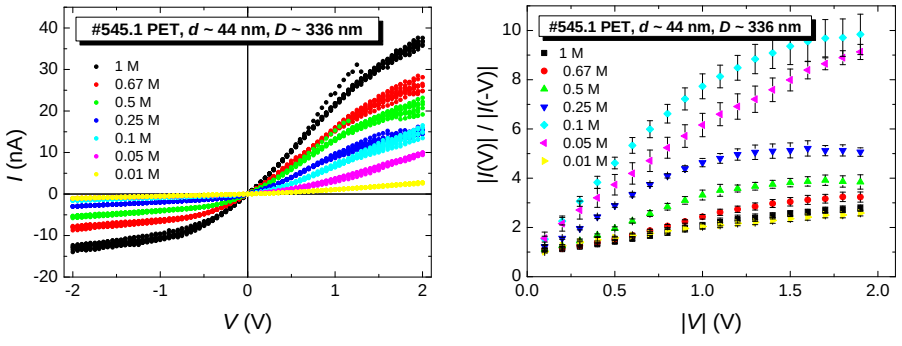

(a) (b)

Figure 31. a) Asymmetric $I - V$ curve of a conical PET pore with $d \sim 44$ nm and $D \sim 336$ nm for concentrations in the range 0.01–3 M KCl b) Variation of the degree of rectification with concentration.

a way slightly different from Figs. 30(b) and 31(b), by plotting the values of $|I(V)|/|I(-V)|$ for a fixed voltage against the concentration. This has been done in Fig. 32 for both pores treated above. Surprisingly the rectification goes down again for concentrations below $\sim$ 0.1 M. While an intuitive explanation for this phenomenon is not easy, a mathematical one can be found in section 4.3.

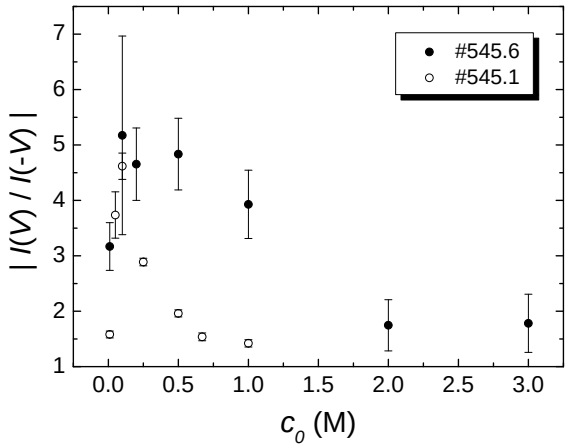

Figure 32. Degree of rectification against concentration for the samples treated above at 0.5 V.

Since biological pores show a saturation in conductance when the concentration is raised well above the physiological level (either due to limited geometry, or a limiting binding-unbinding rate [1]), it was an interesting question as to whether these rectifying track-etched pores would show a similar behavior. Fig. 33 shows conductances (I/V, Fig. 33(a)) and molar conductances (I/Vc, Fig. 33(b)) at various voltages, as a function of electrolyte concentration for sample #545.6 ($I-V$ curves in Fig. 30). As can be seen from the figure, such a saturation is not observed, but the increase in ion current with KCl concentration is especially steep for low concentrations. To extract the typical features of the rectifying pores compared to a classically behaving pore of the same size, the conductance of such a 'classical' pore was calculated as

$$G_c = \frac{Dd\pi\kappa(c_0)}{4L}, \tag{4.1}$$

where d and D are respectively the small and large diameters of the pore, L is the pore length, and $\kappa(c_0)$ the specific conductivity of KCl, (assumed to be the same as in bulk solution, taken from [87] for concentrations between 0.07 M and 2.4 M and calculated by an empirical formula given in [78] for higher and lower concentrations).

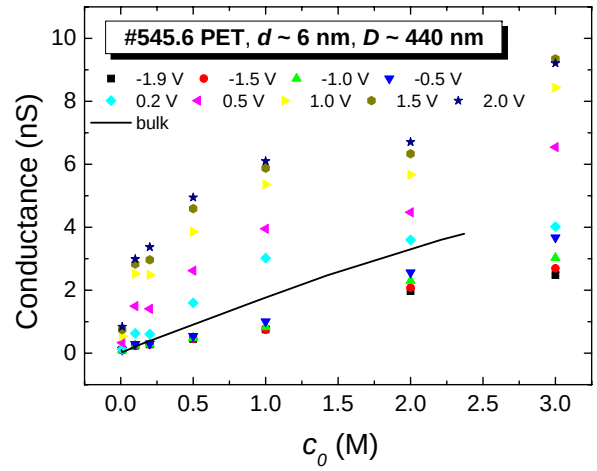

(a)

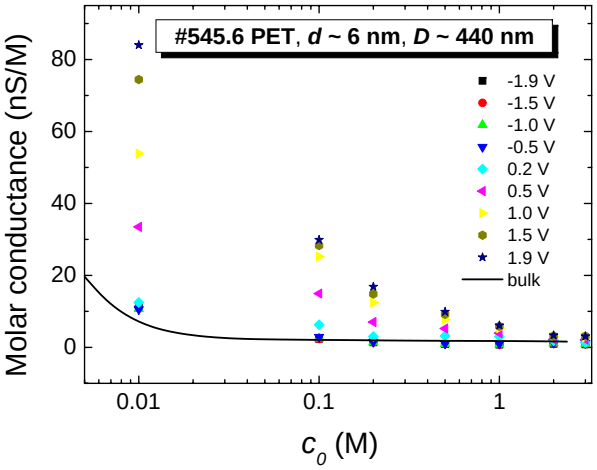

(b)

Figure 33. a) Conductance versus concentration parametric in V for sample #545.6 compared to the value calculated for a pore of the same dimensions, obeying the classical behavior described in the text (bulk) b) Molar conductance versus concentration for the values from a).

Fig. 33(a) compares the measured conductance with the conductance calculated according to Eq. (4.1). The first striking feature is that for positive voltages, the experimental values of the pore's conductance are higher than the calculated values, while for negative voltages they are significantly lower. This result indicates that the nanopores restrict the ion flow in one direction, but promote it in the other. The effect of the steep increase for low concentrations is even more obvious when plotted as molar conductance vs. concentration (Fig. 33(b)). This could be related to surface conductivity, i. e., where a higher concentration of ions near the pore surfaces causes an increased conductance. In this case, the negative surface charge attracts K^+ to the pore walls, forming the double-layer. Thus at lower absolute concentrations, the relative concentration of K^+ ions in the pore (compared to that in the bulk) is much greater (i. e., the double-layer is thicker, filling more of the pore). This higher relative concentration will give elevated conductances, compared to bulk estimates.

4.3 THEORETICAL DESCRIPTION OF ION CURRENT BY CONTINUUM MODEL

The results presented above have been studied by Cervera et al., using a model based on the Poisson and Nernst-Planck (PNP) equations [34, 80]. This model, which uses the surface charge as the only free parameter, is able to reproduce the experimental results semiquantitatively.

4.3.1 *Poisson-Nernst-Planck model*

For these calculations, the nanopore is represented as shown in Fig. 34. Here a_L and a_R are the left and right pore radii, respectively, L is the

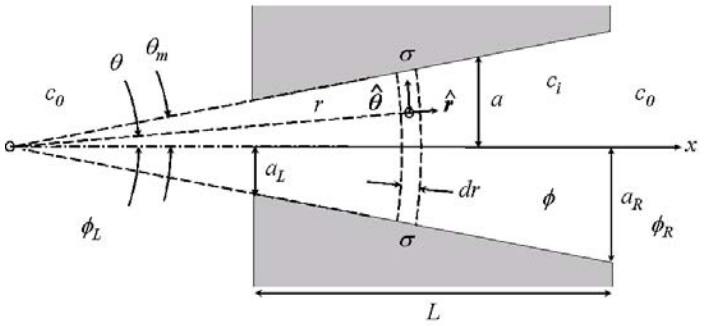

Figure 34. Schematic view of the conical nanopore and spherical coordinates used for solving the PNP equations [34].

length of the nanopore and θ_m denotes its opening angle. ϕ is the local dimensionless electric potential (in units of RT/F) and c_i is the concentration of ionic species i ($i = +$ for cations and $i = -$ for anions). c_0 and $\phi_{L,R}$ are the concentration and potential in left and right bulk solutions. σ is the surface charge density on the pore walls.

The theory is based on the following equations:

The Nernst-Planck equations

$$\vec{j_i} = -D_i(\nabla c_i + z_i c_i \nabla \phi),\ i = +, - \tag{4.2}$$

describe the ionic flux under the influence of an electric potential as well as a concentration gradient.

The Poisson equation

$$\nabla^2 \phi = \frac{F}{RT}\frac{-\rho}{\epsilon} = \frac{F^2}{\epsilon RT}(c_- - c_+) \tag{4.3}$$

allows to calculate the electrostatic potential from the charge density ρ inside the nanopore.

The steady-state continuity equations

$$\nabla \cdot \vec{j_i} = 0,\ i = +, - \tag{4.4}$$

are used.

In these equations, $\vec{j_i}$, D_i, and z_i are the flux density [mol/m^2], diffusion coefficient, and charge number of the ionic species i, respectively. ϵ is the dielectric permittivity of the solution.

The Poisson and Nernst-Planck equations have to be solved simultaneously, because the Nernst-Planck equations give the flux of ion in terms of the concentration and electric profiles, but a the same time the ions influence the electric potential because they carry electric charge [88].

Due to the rotational symmetry of the pore, it is useful to solve the equations in spherical coordinates. Eqs. (4.2) and (4.3) become

$$-\frac{\vec{j_i}}{D_i} = \frac{\partial c_i}{\partial r}\hat{r} + \frac{1}{r}\frac{\partial c_i}{\partial \theta}\hat{\theta} + z_i c_i \left(\frac{\partial \phi}{\partial r}\hat{r} + \frac{1}{r}\frac{\partial \phi}{\partial \theta}\hat{\theta}\right),\ i = +, - \tag{4.5}$$

and

$$\frac{1}{r^2}\frac{\partial}{\partial r}\left(r^2\frac{\partial \phi}{\partial r}\right) + \frac{1}{r^2 \sin\theta}\frac{\partial}{\partial \theta}\left(\sin\theta \frac{\partial \phi}{\partial \theta}\right) = \frac{F^2}{\epsilon RT}(c_- - c_+). \tag{4.6}$$

A few assumptions are made, to be able to solve the above equations:

- the external solutions are ideal and perfectly stirred
- electro-osmotic effects are ignored at first approximation [89]

- the system is isothermal
- the negative charges are distributed homogeneously over the pore wall
- diffusion coefficients for infinite dilution are used [90] ($D_+ = 1.95 \cdot 10^{-5}\mathrm{cm}^2/\mathrm{s}$ and $D_- = 2.03 \cdot 10^{-5}\mathrm{cm}^2/\mathrm{s}$).

Additionally, it is assumed that due to the small pore angle, the ionic fluxes have only radial components ($\vec{j_i} = j_i \hat{r}$, $i = +, -$) and therefore Eq. (4.5) becomes

$$-\frac{j_i}{D_i} = \frac{\partial c_i}{\partial r} + z_i c_i \frac{\partial \phi}{\partial r},\ i = +, -. \tag{4.7}$$

This assumption is reasonable, because the solution cannot penetrate the pore walls. To minimize the computational effort, instead of solving the Nernst-Planck and Poisson equations locally, average values over spherical shells dr are calculated by using the average operator

$$\langle\rangle \equiv \frac{1}{(1-\cos\theta_m)} \int_0^{\theta_m} \sin\theta \, \mathrm{d}\theta. \tag{4.8}$$

It is further assumed that the average concentrations inside and outside the pore are related through the Donnan equilibrium conditions [91]

$$\begin{aligned} \langle c_i \rangle_L &\equiv \langle c_i(r_L) \rangle = c_0 \exp(-z_i \Delta\phi_{D,L}),\ i = +, -, \\ \langle c_i \rangle_R &\equiv \langle c_i(r_R) \rangle = c_0 \exp(z_i \Delta\phi_{D,R}),\ i = +, -, \end{aligned} \tag{4.9}$$

where $\Delta\phi_{D,L} \equiv \langle \phi(r_L) \rangle - \phi_L$ and $\Delta\phi_{D,R} \equiv \phi_R - \langle \phi(r_R) \rangle$ are the Donnan potential drops at the left and right pore/solution interfaces, respectively.

A Donnan equilibrium, involving an electric potential gradient, is built up at interfaces between regions of which both contain mobile ions, but one additionally contains charges which are not able to penetrate into the other region. This can be either the case (as studied originally by Donnan [91]), if two electrolyte solutions are separated by a membrane not permeable to an ionic species present in only one of the solutions (e. g., a cell containing big charged proteins which cannot pass the cell membrane) or as well at the interface between a narrow pore containing fixed charges and the surrounding solution [92–94]. This equilibrium arises from a balance between diffusion and electrical attraction/repulsion between the mobile and fixed charges.

To deduce the value of the electric potential which is built up, as well as the relations between concentrations of different ionic species inside and outside the pore (or on either side of the membrane), it is usually assumed that the total electrochemical potential μ_i (being the sum of the chemical potential and the electrostatic potential)

$$\mu_i = \underbrace{\mu_i^0 + RT \ln(c_i)}_{\text{chem. pot.}} + \underbrace{RT z_i \phi_i}_{\text{el. pot.}} \tag{4.10}$$

is equal for one ionic species on both sides of the interface [95]. In Eq. (4.10) the chemical potential has been split in a part (μ_i^0) independent of and a part depending on the concentration c_i (here c_i was substituted for the activity coefficient, since the ideal dilute solution case is considered and the activity coefficients are equal inside and outside the pore).

For the pore/solution interface of a system with concentrations c_i^{out} outside and c_i^{in} inside the pore, this leads to

$$RT\ln(c_i^{\text{in}}) + RTz_i\phi_i^{\text{in}} = RT\ln(c_i^{\text{out}}) + RTz_i\phi_i^{\text{out}}, \tag{4.11}$$

where it has been assumed that $\mu_i^{0,\text{in}} = \mu_i^{0,\text{out}}$ for each ionic species. Therefore, the Donnan potential difference is

$$\Delta\phi_D = \phi_i^{\text{in}} - \phi_i^{\text{out}} = \frac{1}{z_i}\left(\ln(c_i^{\text{in}}) - \ln(c_i^{\text{out}})\right) = \frac{1}{z_i}\ln\left(\frac{c_i^{\text{in}}}{c_i^{\text{out}}}\right). \tag{4.12}$$

This can also be written as

$$c_i^{\text{in}} = c_i^{\text{out}}\exp(z_i\Delta\phi_D). \tag{4.13}$$

Because $\Delta\phi_D$ is the same for all ionic species, one can also write

$$\frac{1}{z_+}\ln\left(\frac{c_+^{\text{in}}}{c_+^{\text{out}}}\right) = \frac{1}{z_-}\ln\left(\frac{c_-^{\text{in}}}{c_-^{\text{out}}}\right) \Rightarrow \ln\left(\frac{c_+^{\text{in}}}{c_+^{\text{out}}}\right) = \ln\left(\frac{c_-^{\text{out}}}{c_-^{\text{in}}}\right) \tag{4.14}$$

or

$$c_+^{\text{in}}\cdot c_-^{\text{in}} = c_+^{\text{out}}\cdot c_-^{\text{out}}. \tag{4.15}$$

To fulfill electroneutrality, $c_+^{\text{out}} = c_-^{\text{out}} = c_0$ in the case studied here, which then leads to Eq. (4.9).

Combining them with the condition of local electroneutrality

$$\sum_i z_i\langle c_i\rangle_j + X_j = 0,\ j = L, R, \tag{4.16}$$

at the interfaces, where

$$X_j \equiv X(r_j) = \frac{\sin\theta_m\sigma}{Fr(1-\cos\theta_m)} \tag{4.17}$$

is the fixed charge concentration contained in a spherical shell of radius r_j (the Gauss law $\frac{1}{r}\frac{\partial\phi}{\partial\theta}|_{\theta=\theta_m} = \frac{F\sigma}{\epsilon RT}$ has been used in the integration of the Poisson equation) finally leads to the average ionic concentrations and electric potentials at the pore/solution interfaces

$$\langle c_i\rangle_j \equiv \langle c_i(r_j)\rangle = \frac{1}{2}(-z_iX_j + \sqrt{X_j^2 + 4c_0^2}) \tag{4.18}$$

and

$$\langle\phi(r_j)\rangle = \phi_j - \frac{1}{z_i}\ln\frac{\langle c_i\rangle_j}{c_0}, \tag{4.19}$$

both with $i = +, -$ and $j = L, R$.

The $I - V$ curve is now obtained by calculating the average concentration and potential profiles at any applied voltage $V \equiv RT(\phi_L - \phi_R)/F$ using the boundary conditions from Eqs. (4.18) and (4.19). From these profiles, the average ionic fluxes are calculated. Finally, the total electric current passing through any spherical section of the nanopore is obtained by

$$I = \sum_i z_i F \langle J_i \rangle , \tag{4.20}$$

with

$$\langle J_i \rangle = 2\pi(1 - \cos\theta_m) r^2 \langle j_i \rangle , \; i = +, -. \tag{4.21}$$

The full derivation of the equations can be found in [34, 80] and has been developed by J. Cervera and P. Ramírez.

4.3.2 *Comparison with experimental results*

Figs. 35 and 36 compare the experimental and theoretical $I - V$ curves for KCl concentrations between 0.01 and 1 M for the two samples #545.1 and #545.6 already presented in section 4.14. In the graphs, radii a_L and a_R as introduced in Fig. 34 are now given instead of diameters D and d for consistency reasons.

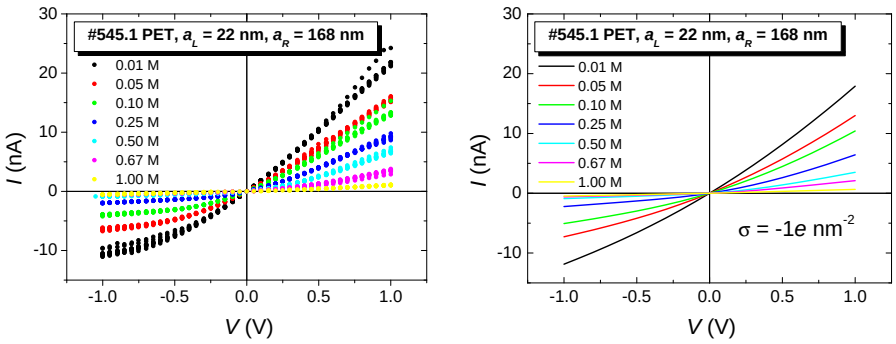

(a) (b)

Figure 35. Experimental (a) and calculated (b) $I - V$ curves for sample #545.1 with $a_L = 22$ nm and $a_R = 168$ nm, parametric in the electrolyte concentration.

To reduce the computational effort, calculations were performed only up to 1 V in contrast to the measurements, which range up to 2 V. For both samples, a value of $\sigma = -1\ e/\text{nm}^2$ has been used, which is in agreement with the values reported experimentally for track-etched

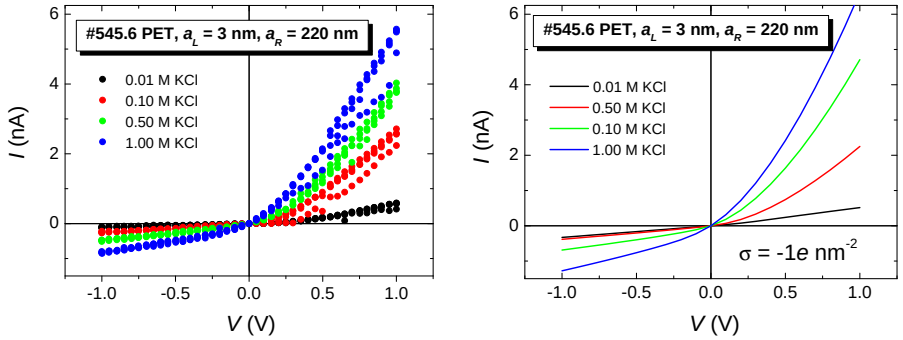

Figure 36. Experimental (a) and calculated (b) $I - V$ curves for sample #545.6 with $a_L = 3$ nm and $a_R = 220$ nm, parametric in the electrolyte concentration.

PET pores [77, 96]. In Fig. 37, the calculated average potential profiles inside the pore for sample #545.1 are shown for $c_0 = 0.1$ M and different applied voltages. The electric potential profiles are strongly nonlinear

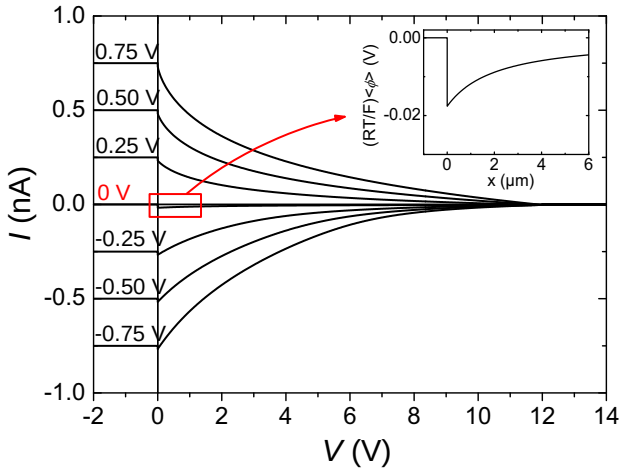

Figure 37. Calculated average profile of the electric potential of sample #545.1, parametric in V.

in the region of the tip of the pore, where the effects of fixed charges have the strongest influence. The inset shows a potential well at the pore tip, similar to that found in the ratchet model. This leads to strong concentration changes in these regions, as shown in Fig. 38, where the average concentration profiles for positive and negative charges are

displayed. For $V > 0$ the electric field drags the cations to the pore

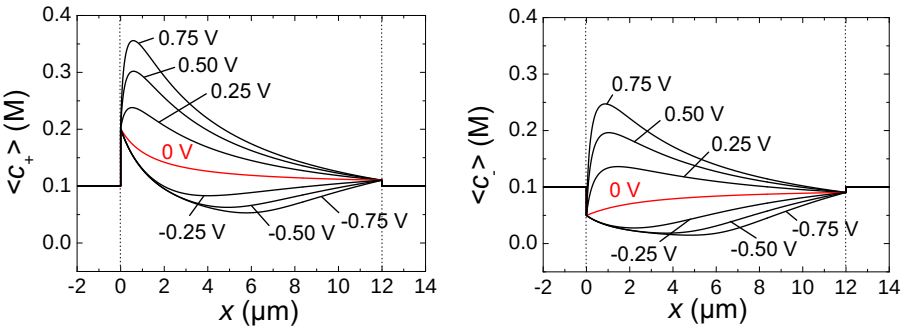

Figure 38. Calculated average concentration profiles of cations and anions inside sample #545.1, parametric in the applied voltage.

tip, where they tend to accumulate due to the fixed charges, and this leads to a maximum in the concentration profile. The anions are also forced towards the nanopore tip in order to preserve electroneutrality, and the shape of the corresponding concentration profile is similar to that of the cations. For $V < 0$, however, the electric field drives the positive majority ions out of the narrow pore region, and the negative minority ions follow the same trend to preserve electroneutrality (the concentration profiles of both the majority and minority ions attain now a minimum). The conductance (I/V) is directly related to the concentration of charge carriers, so the decreased concentrations for negative voltages give lower conductances than in the case $V > 0$ and therefore lower currents, leading to the observed rectification effect.

Besides this general difference for positive and negative polarities, one can look at the voltage dependence of the conductance. As an example the experimental and calculated conductance values are shown in Fig. 39 for sample #545.1 at 0.1 M. It can be seen that the general trend is reproduced by the model, however, deviations seem to increase for higher voltages, especially for higher concentrations. In the region between 1 and 2 V, for concentrations > 0.5 M, the experimental conductance values saturate, or for some pores, even reach a maximum and begin to decrease again. This leads then to the saturation somtimes observed in the degree of rectification for higher voltages (see Figs. 30(b) and 31(b)). The origin of this voltage dependent saturation/maximum is not yet clear and it would be an interesting task to perform calculations also for these higher voltages.

In Fig. 40, $|I(V)|/|I(-V)|$ has been plotted against the concentration for both pores treated above for 0.5 V, together with the corresponding calculations. Both experimental and theoretical values increase for de-

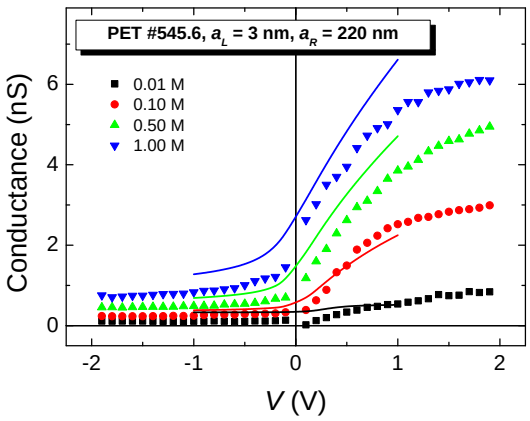

Figure 39. Voltage dependent conductance (I/V) for different concentrations of c_0 for sample #545.6. Symbols correspond to the experimental values, the lines to the theoretical ones.

creasing concentrations, attain a maximum at about 0.1 M and decrease again for $c_0 < 0.1$ M.

To better understand this maximum, the absolute current values for the same sample for $V = 0.5$ V and $V = -0.5$ V are plotted against the concentration c_0 in Fig. 41 for sample #545.6. Again, symbols correspond to the experimental values and the solid lines to the theoretical ones.

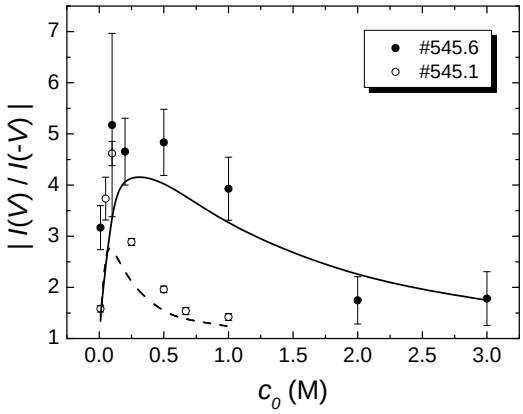

Figure 40. Rectification ratio for the samples #545.1 and #545.6 at $V = 0.5$ V. Symbols correspond to the experimental data and lines to the theoretical results.

It is clearly visible that the absolute current values for positive and negative voltages approach each other for decreasing concentrations. In the limit $c_0 \to 0$, the theory gives total anion exclusion from the pore and

therefore

$$\langle c_- \rangle \ll \langle c_+ \rangle \approx -X(r) \tag{4.22}$$

and

$$r^2 \langle j_- \rangle \ll r^2 \langle j_+ \rangle = \text{const.} \tag{4.23}$$

For this case the linear $I - V$ relationship

$$I \approx 2\pi(1 - \cos\theta_m) F r^2 \langle j_+ \rangle \approx -\frac{2\pi D_+ \sin\theta_m F \sigma}{RT \ln(a_R/a_L)} V \tag{4.24}$$

is obtained.

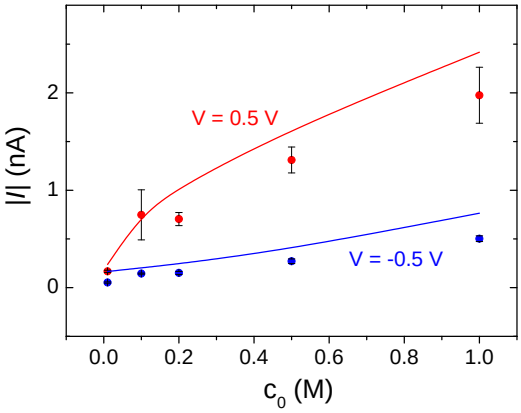

Figure 41. Absolute current values for $V = 0.5$ V and $V = -0.5$ V for sample #545.6; data points: experimental values; line: theoretical values.

The results presented above show that the main features of the $I - V$ curves of charged, conical pores can be described by a fairly simple model, which helps to give an intuitive view of the physical processes taking place in these systems. Up to now the model has been applied also to selectivity measurements with these pores presented in the following chapter, and it will be interesting to explore the range of its validity, for example, by applying it to $I - V$ measurements with Kapton pores, which usually exhibit a much stronger rectification effect than PET.

4.3.3 *Sensitivity of calculations to pore diameter and surface charge*

As mentioned earlier, the only free parameter in the model is the surface charge σ, which is usually determined by a fit to the experimental data. However, important input parameters to the model are the two diameters of the pore. As pointed out in chapter 3, there is some uncertainty in the

determination of the big (and subsequently also the small diameter) such that the real diameter could be bigger than the one extracted from SEM measurements or calculations. This would result in the small diameter being reduced by the same factor by which the large diameter is increased. For the calculations in the following chapters, the values were used as obtained from SEM/etch times (D) and conductometry (d), due to a lack of more precise values. Also the effects observed to date concern cylindrical pores, studies with wires in conical pores are under way. Some earlier publications: a PEG translocation study [77] and the recent SEM observation of 40 nm small pore openings [50] also indicate that the values obtained for the diameters by the methods used here are realistic.

Nevertheless, the effect of increasing D by 50 or 100 nm (possible values for PET pores in the size region of several hundred nanometer diameter; see Fig. 12) on the model calculations is illustrated in the following figures. As an example, sample #545.6 ($D \sim 440$ nm, $d \sim 6$ nm, corresponding to $R \sim 220$ nm and $r \sim 3$ nm, $I - V$ curves in Fig. 30(a)) was used. Increasing the diameter by 50 nm, results in $R \sim 245$ nm and $r \sim 2.7$ nm (radii are used in the model), increasing it by 100 nm leads to $R \sim 270$ nm and $r \sim 2.4$ nm. The results for these different pore radii, together with the experimental values for this pore are shown in Fig. 42 for 0.1 and 1 M KCl. A value of $\sigma = -1\ e/\text{nm}^2$ as obtained from the fit with the initial radii, was used for all sizes.

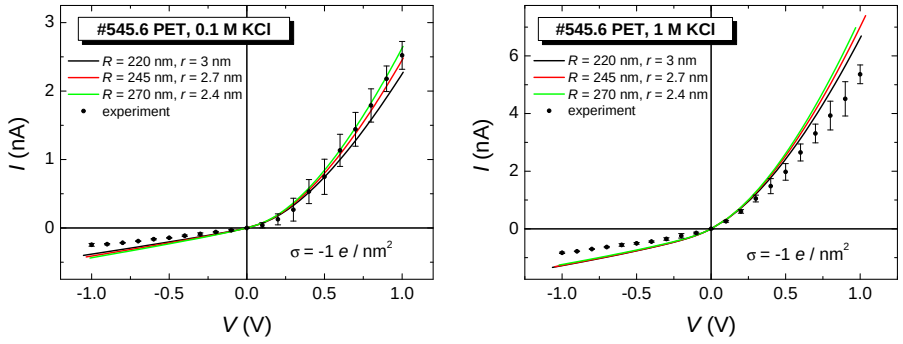

(a) (b)

Figure 42. $I - V$ curves for sample #545.6 in a) 0.1 M KCl and b) 1 M KCl (black dots). The pore openings were determined by SEM/conductometry to be $R \sim 220$ nm and $r \sim 3$ nm. Calculations with the PNP model for these dimensions as well as R increased by 25 nm and 50 nm with correspondingly reduced r values are also shown. $\sigma = -1\ e/\text{nm}^2$ in all calculations.

The results for larger R and smaller r show a slightly higher rectification (higher currents for positive voltages, negligible change for negative voltages) which makes sense, assuming that a larger opening angle gives

higher rectification due to a stronger asymmetry of the electrostatic potential inside the pore (cylindrical pores do not rectify the current at all). However, the change for positive voltages is for both concentrations in the same range as the experimental error, while the fit is in general not as good for negative voltages.

Fig. 43 illustrates the effect of a change in σ, the parameter describing the surface charge. Again, the measurements for 0.1 and 1 M are shown, together with calculations for the original diameter values ($R \sim 220$ nm, $r \sim 3$ nm) and a set of curves parametric in σ for the most deviating dimensions $R \sim 270$ nm and $r \sim 2.4$ nm.

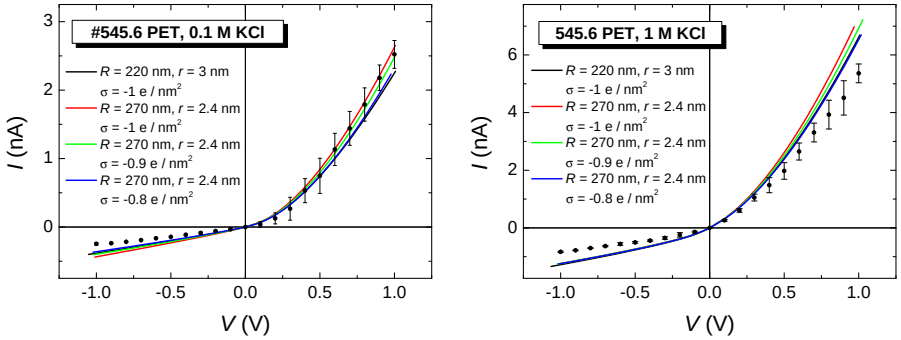

(a) (b)

Figure 43. $I - V$ curves for sample #545.6 in a) 0.1 M KCl and b) 1 M KCl (black dots). The $I - V$ curves as calculated for $R \sim 220$ nm, $r \sim 3$ nm (black curves) and $R \sim 270$ nm, $r \sim 2.4$ nm (red curves) are shown together with calculations for the latter values parametric in σ (green and blue curves). A change of σ by 0.2 e/nm^2 is needed to compensate the diameter change.

The effect of lowering σ is opposite to increasing the opening angle: reducing σ by 0.2 e/nm^2, brings the curve back to the initial shape. This effect is also not really surprising, since a lower surface charge leads to lower rectification (neutral pores do not rectify) (see Fig. 24).

Due to this relatively weak dependence on a simultaneous change of both radii (as it could be caused here by uncertainties in the determination of R), the qualitative findings presented here should not be significantly affected.

5 SELECTIVITY

One of the most important properties of biological ion channels is their selectivity for different ions, which leads to electric membrane potentials due to different intra- and extracellular ionic concentrations. These channels are therefore able to create electric signals by changes in membrane potentials, which control a large number of processes in all living organisms.

One example for highly selective ion channels are potassium channels, which transport K^+ ions, but are impermeable to the even smaller Na^+ ions. How this is possible was discovered in 1998, when the first crystal structure of a potassium channel was published, revealing a narrow selectivity filter of only 12 Å length, which is chemically and structurally optimized to let pass only potassium ions, but not the smaller sodium ions [2]. To pass the channel, an ion has to be dehydrated, which costs energy. Inside the selectivity filter, binding sites exist, which can replace the water shell of the ion, thus minimising the required energy for transport. But this works only if the ion has exactly the right size, and not if it is too small [97]. Another example are Ca^{2+} channels, which preferably transport calcium ions, even though the concentration of other ions such as K^+ or Na^+ is much higher and though furthermore Ca^{2+} and K^+ ions have almost the same size. This is achieved by high-affinity Ca^{2+} binding sites, which can change conformation to transport the calcium ions [97]. Synthetic nanometer sized charged pores are known to also exhibit selectivity due to their fixed surface charges, by transporting mainly ions with the opposite charge to those fixed on the pore walls, and rejecting those of equal charge [27, 28, 98–101].

This is also interesting for gaining a better understanding of the underlying processes and also for any future applications involving transport of charged particles through nanopores.

5.1 BACKGROUND

To understand how selectivity can lead to potential differences, the following example is usually considered:

A membrane containing one or more selective pores separates two solutions of different concentrations, each containing an ionic species which can pass through the pores, as well as one that cannot [1]. In Fig. 44, the electrolyte is KCl and the membrane is permeable only to the positively charged K^+ ions. Immediately after insertion of the solutions, there is no electric potential difference present, but the ions which are

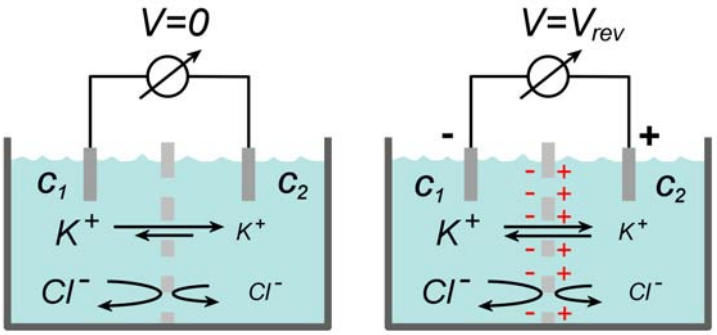

Figure 44. Membrane permeable only to positive ions separates two different concentrations of KCl ($c_1 > c_2$) a) Situation directly after insertion of solutions; $V = 0$, equilibrium not yet reached b) equilibrium state, $V = V_{\text{rev}}$.

able to pass the pore will start to diffuse along the concentration gradient, therefore there is a net flux of K^+ ions from one side to the other. Since the Cl^- ions can not pass through with them to preserve elctroneutrality, the side to which the net flow is directed becomes slightly positively charged relative to the other. This potential difference now results in a flow of cations in the opposite direction. The potential will build up, until both fluxes are equal and equilibrium is reached.

This potential, which is also called reversal potential V_{rev}, can either be measured directly with an amplifier in current-clamp mode, or if such equipment is not available, simply extracted from an $I - V$ curve recorded under asymmetric electrolyte conditions, where V_{rev} is the potential for zero current (Fig. 45).

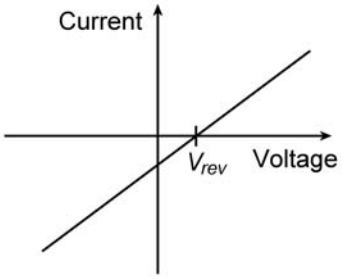

Figure 45. Schematic example of an $I - V$ curve recorded under asymmetric electrolyte conditions, indicating V_{rev} as the potential for zero current.

For an ideally selective membrane as the one in Fig. 44, V_{rev} is given

by the Nernst equation [1]

$$V_{\text{rev}} = \frac{RT}{F}(\phi_2 - \phi_1) = \frac{RT}{zF}\ln\frac{c_1}{c_2}, \tag{5.1}$$

where ϕ_1 and ϕ_2 are the potentials on each side of the membrane and c_1 and c_2 are the corresponding concentrations of an ion with charge number z.

However, if a membrane is not ideally selective (i. e., also allowing a small flux of anions to pass), the magnitude of the measured value of V_{rev} will be smaller than the theoretical value predicted by Eq. (5.1).

A measure for the amount of current transported by one ionic species (and therefore for the selectivity of a system to that species) is the transference number t_i, which is defined as

$$t_i = \frac{I_i}{I_{\text{tot}}},\ i = +, -, \tag{5.2}$$

where I_i is the current carried by the ionic species i, and I_{tot} is the total measured current. From this definition it is clear that $t_+ + t_- = 1$ (if only one type of anion and cation are present in the solution, as considered here) and Eq. (5.1) becomes [102]

$$V_{\text{rev}} = V_+ - V_- = \underbrace{\frac{RT}{F}\ln\frac{c_1}{c_2}}_{V_{\text{max}}}(t_+ - t_-). \tag{5.3}$$

And because $t_- = 1 - t_+$,

$$t_+ = \frac{V_{\text{rev}}}{2V_{\text{max}}} + 0.5 = \frac{1}{2}\left[1 + \frac{F}{RT}\frac{V_{\text{rev}}}{\ln(c_1/c_2)}\right]. \tag{5.4}$$

Using this relation, the selectivity of a pore can be determined by measuring its reversal potential.

5.2 ASYMMETRIC REVERSAL POTENTIAL IN CONICAL NANOPORES

Conical track-etched nanopores are known to be highly cation selective due to the negative charges created on their inner walls during the etching process [33, 77]. More recently it was found that the selectivity of such pores depends on the direction of the applied concentration gradient, being higher when the lower concentration is on the side of the pore with the small opening. Siwy et al. [28] studied this phenomenon in terms of the diffusive current, which is the current flowing through the pore at zero potential. In contrast, the measurements done here focus directly on the reversal potential, since this is the easiest way to compare the results with other measurements (e. g. on biological ion channels) where V_{rev} is usually the quantity considered.

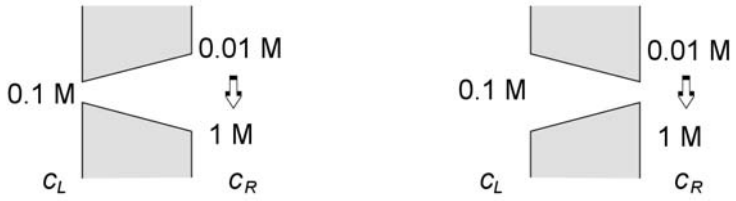

(a) Arrangement 1 (b) Arrangement 2

Figure 46. The two experimental arrangements in which the concentration gradients were applied.

The pores investigated were prepared in PET by asymmetric track-etching as described in section 2.2.2, and measurements were done in the following way: up to 10-fold concentration gradients of KCl were applied such that one of the two concentrations was always 0.1 M. This means that for a fixed concentration of 0.1 M on one side of the pore, the concentrations on the other side were varied from 0.01–1 M (see Fig. 46). In this case, a measurement cell composed of three chambers (see Fig. 47) was used, where the PET foil under study separated the left and middle chambers (L and R) and a second PET foil containing two wide (700 nm), cylindrical pores, separates the middle and right chambers (R and G). The outer chambers were always filled with electrolyte of equal

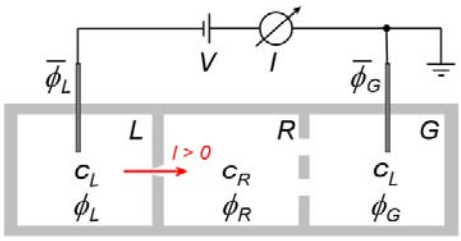

Figure 47. Sketch of the setup used for the measurements of V_{rev}. In addition to the foil under study which separates chambers L and R, a second foil containing a wide, cylindrical PET pore is used as a salt bridge to allow the two measurement electrodes to be always in equal concentrations.

concentrations, so that the measuring Ag|AgCl electrodes were not in contact with different electrolyte concentrations, which would lead to additional potential gradients and affect the results. The contribution of the large pores to V_{rev} can be neglected, since their conductance is much larger than that of the conical pore. It has been tested that the $I - V$ curve of the pore under study is the same with and without the cylindrical

pores added.

For this setup, the measured value is the total electric potential difference between chambers L and G which is composed of

$$\bar{\phi_L} - \bar{\phi_G} = \underbrace{(\bar{\phi_L} - \phi_L)}_{\text{left electrode}} + \underbrace{(\phi_L - \phi_R)}_{\text{conical nanopore}} + \underbrace{(\phi_R - \phi_G)}_{\text{cylindrical pores}} + \underbrace{(\phi_G - \bar{\phi_G})}_{\text{right electrode}} \quad (5.5)$$

The contributions for the electrodes cancel, because they are both immersed in the same electrolyte concentration. The contribution for the cylindrical pores is negligible under current flow due to their high conductance and gives approximately the liquid junction value [103] $\phi_R - \phi_G = -\frac{D_- - D_+}{D_- + D_+} \ln \frac{c_L}{c_R}$ for zero current, due to their comparably big radii. If infinite dilution values are assumed for the diffusion coefficients $D_+ = 1.95 \cdot 10^{-5}\text{cm}^2/\text{s}$ and $D_- = 2.03 \cdot 10^{-5}\text{cm}^2/\text{s}$ [90], this yields a potential drop of about ± 1.5 mV for a 10-fold concentration gradient, corresponding to the highest one used in the experiments.

Otherwise, the setup for the $I - V$ measurements was identical to that described in section 4.1, where the voltage is applied via a National Instruments analog I/O card. The triangular signal used to record the current-voltage curves was composed of 10-mV steps and ranged from –0.5 to +0.5 V. The time interval between two points was 1 s. Again, unbuffered KCl of pH 5.6±0.2 has been used.

At least two periods of $I - V$ curves were recorded for each concentration gradient and the mean current was calculated for each voltage level, with the error given by the standard deviation. V_{rev} was obtained by linear interpolation between the pair of consecutive measurement points which enclose the voltage-axis. The error bars result from the different interpolation lines and include also the uncertainty due to the cylindrical pores estimated above.

Since the Nernst equation is linear in $\ln(c_R/c_L)$, it is advantageous to plot V_{rev} against the logarithm of the concentration gradient. The result for a pore with $a_L \sim 4$ nm and $a_R \sim 110$ nm is shown in Fig. 48.

Fig. 48(a) shows the $I - V$ curve of this pore recorded in 0.1 M KCl and Fig. 48(b) the results for V_{rev} for the two configurations of the concentration gradient as indicated. For comparison, the theoretical Nernst limit for an ideally selective pore is shown. It can be seen that the measured potential is always lower than the theoretical one, indicating that the pore is not 100% selective for cations but also allows some anions to pass through. It is also evident that in general the deviation from the theoretical limit is smaller for lower concentrations ($\log_{10}(c_R/c_L) < 0$), which can be explained by the fact that in this case the charges on the pore walls are less screened and can therefore influence the ionic transport to a larger extent. The second result that can be extracted from Fig. 48(b) is the fact that there is a noticeable difference between the curves belonging to arrangement 1 and 2. The potential is higher for arrangement 1 when $\log_{10}(c_R/c_L) > 0$, and for arrangement 2 when $\log_{10}(c_R/c_L) < 0$. These

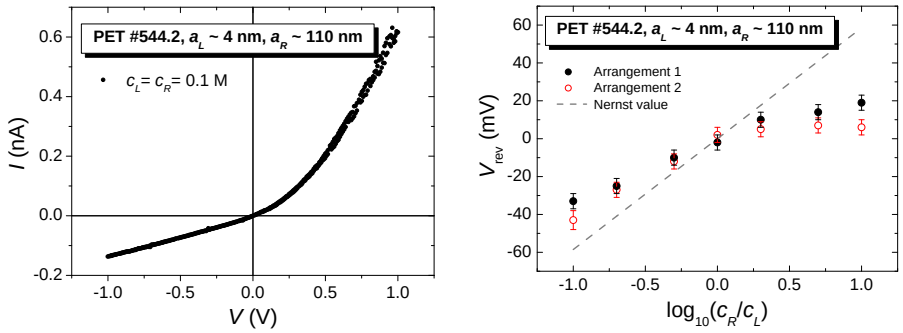

(a) (b)

Figure 48. a) $I - V$ curve of a pore with $a_R \sim 110$ nm and $a_L \sim 4$ nm, recorded in 0.1 M KCl under symmetric conditions b) Reversal potentials for up to 10-fold concentration gradients, direction as indicated in the insets.

cases represent the situation where the lower concentration is on the small side of the pore. This result is consistent with the findings in [28] and can again be explained by a lower screening of the fixed charges at the pore tip for lower concentrations, since the majority of the total resistance of the system, and thus the majority of the potential difference, occurs close to the pore tip [104]. For example, with the pore studied, 50% of the total resistance is due to the first 200 nm [105] (supporting information), after the pore tip. As a result, the overall behavior of the pore depends stronly on the transport characteristics of the tip region. The difference between the curves is larger for $\log_{10}(c_R/c_L) > 0$, because here the effect of the screening at the pore tip for arrangement 1 is relatively larger compared to arrangement 2.

5.3 DESCRIPTION BY POISSON-NERNST-PLANCK MODEL

To better understand the results, it is again useful to apply the PNP model described in section 4.3, which allows one to calculate not only the average electric potential and concentration profiles along the pore together with the total ionic flux, but also the transport numbers, t_+ and t_-.

5.3.1 *Theory*

The parameters used to describe the pore are given in Fig. 49 and are identical to these in Fig. 34 except that there are now different concentrations on the left- and right-hand side of the pore. To study the dependence of

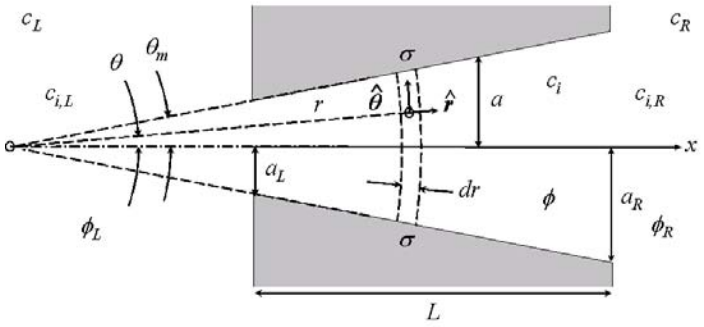

Figure 49. Scheme of a conical nanopore in the presence of a concentration gradient.

selectivity on the direction of the concentration gradient, the two different experimental arrangements presented in Fig. 46 are considered. The concentration in the left chamber is always c_L= 0.1 M, while c_R will be varied from 0.01 to 1 M. The potential difference between the solutions in the chambers L and R is defined as

$$V \equiv \frac{RT}{F}(\phi_L - \phi_R), \tag{5.6}$$

and ion flux from left to right is defined as positive. Since the reversal potential is given by Eq. (5.6) for zero current, it can be obtained by using $I = 0$ in Eq. (4.20). This leads to

$$\langle J_+ \rangle = \langle J_- \rangle \equiv \langle J \rangle \,, \tag{5.7}$$

and therefore

$$\langle j_+ \rangle = \langle j_- \rangle \equiv \langle j \rangle \,. \tag{5.8}$$

The total potential at zero current can be divided into three parts [92]:

$$V_{\text{rev}} = V_{D,L} + V_{\text{diff}} + V_{D,R}, \tag{5.9}$$

where $V_{D,L}$ and $V_{D,R}$ are the Donnan potential differences occurring at the left and right pore-solution interfaces

$$\begin{aligned} V_{D,L} &= \frac{RT}{F}\left[\phi_L - \langle \phi(r_L) \rangle\right] = \frac{RT}{F} \ln \frac{\langle c_+ \rangle_L}{c_L} \\ &= \frac{RT}{F} \ln \frac{-X_L/2 + \sqrt{(X_L/2) + c_L^2}}{c_L} \end{aligned} \tag{5.10}$$

and

$$\begin{aligned} V_{D,R} &= \frac{RT}{F}\left[\langle\phi(r_R)\rangle - \phi_R\right] = \frac{RT}{F}\ln\frac{c_R}{\langle c_+\rangle_R} \\ &= \frac{RT}{F}\ln\frac{c_R}{-X_R/2+\sqrt{(X_R/2)+c_R^2}}, \end{aligned} \tag{5.11}$$

as calculated from Eqs. (4.14) and (4.19). Again, $X_k, k = L, R$ is the volume fixed charge concentration (see Eq. (4.17)). V_{diff} is the so-called diffusion potential, which corresponds to the potential difference inside the nanopore between tip and base. It is given by

$$V_{\text{diff}} = \frac{RT}{F}\left[\langle\phi(r_L)\rangle - \langle\phi(r_R)\rangle\right]. \tag{5.12}$$

Therefore,

$$V_{\text{rev}} = \frac{RT}{F}\left(\phi_L - \langle\phi(r_L)\rangle + \langle\phi(r_L)\rangle - \langle\phi(r_R)\rangle + \langle\phi(r_R)\rangle - \phi_R\right). \tag{5.13}$$

Examining two limiting cases gives an initial confirmation of this result. These cases are

- highly charged pores and very dilute solutions ($|X| \gg c_k,\ k = L, R$), where it leads to the Nernstian value for V_{rev} (ideal solution limit), if the ion fluxes are negligible ($\langle j\rangle = \langle j_+\rangle \approx 0$)
- uncharged pores ($|X| = 0$), where the cation and anion concentrations are equal ($\langle c_+\rangle = \langle c_-\rangle \equiv \langle c\rangle$) and the liquid junction limit [103] $V_{\text{rev}} = V_{\text{diff}} = -\frac{RT}{F}\frac{D_- - D_+}{D_- + D_+}\ln\frac{c_R}{c_L}$ is obtained.

5.3.2 *Comparison with experimental results*

Fig. 50 shows the potential profiles inside a conical pore with $a_L = 5$ nm and $a_R = 200$ nm calculated for three different concentration gradients, each for arrangement 1 and arrangement 2. In the following, these two arrangements will be denoted by superscripts (1) and (2). To interpret these figures correctly, one should keep in mind the composition of V_{rev} given in Eq. (5.9), which leads to

$$\begin{aligned} V_{\text{rev}} &= V_{D,L} + V_{\text{diff}} + V_{D,R} \\ &= \frac{RT}{F}\left(\phi_L - \langle\phi(r_L)\rangle + \langle\phi(r_L)\rangle - \langle\phi(r_R)\rangle + \langle\phi(r_R)\rangle - \phi_R\right), \end{aligned} \tag{5.14}$$

using the definitions from Eqs. (5.10), (5.11) and (5.12).

The contribution of $V_{D,L}^{(1)}$ to $V_{\text{rev}}^{(1)}$ and $V_{D,L}^{(2)}$ to $V_{\text{rev}}^{(2)}$, respectively is the same for all three concentration gradients, since the concentration on the left side is always fixed at 0.1 M. $V_{D,L}^{(1)} \gg V_{D,L}^{(2)}$, because the potential

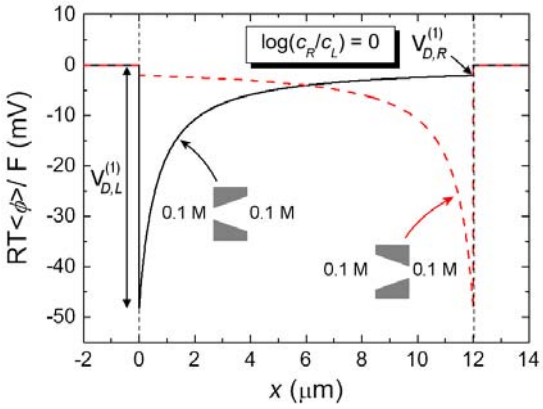

(a)

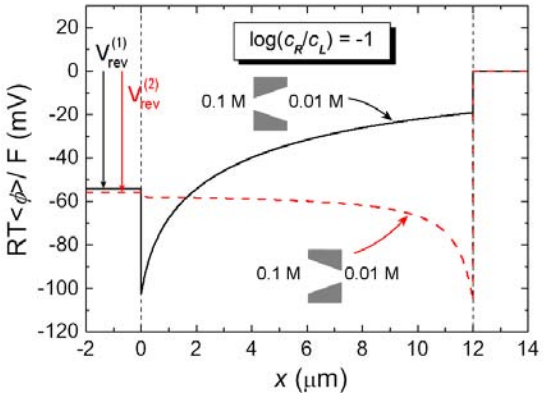

(b)

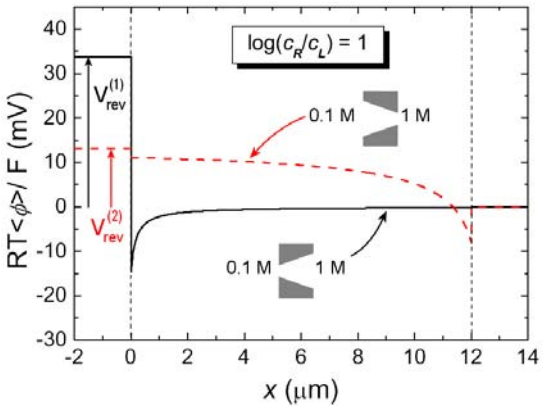

(c)

Figure 50. Potential profiles for arrangements 1 and 2 for a) symmetric concentrations 0.1 M b) 0.1 M and 0.01 M c) 0.1 M and 1 M. The reversal potential for the three different cases is marked by arrows (there are no arrows in a), because there the reversal potential is zero.

drop is higher at the pore tip than at the base. In contrast, the diffusion potential and the Donnan potential on the right are different for all three cases, because different concentrations are present on the right. Due to convention, the sign of $V_{D,L}$ is always positive, while $V_{\text{diff}} < 0$ for arrangement 1 and > 0 for arrangement 2. $V_{D,L}$ is always negative.

In Fig. 50(a) no concentration gradient is present. Thus, there is no net flow of ions, and $V_{\text{rev}} = 0$. The Donnan potential drops at the left and right pore/solution interfaces are different, however, due to the asymmetric shape of the pore. With $V_{\text{rev}} = 0$ for arrangements 1 and 2 in Eq. (5.9) this leads to

$$V_{\text{diff}} = -V_{D,L} - V_{D,R}. \tag{5.15}$$

For a symmetric pore the Donnan potential drops would be zero, leading to a vanishing diffusion potential.

Fig. 50(b) deals with the case $\log_{10}(c_R/c_L) = -1$, corresponding to the comparatively low concentrations 0.1 M and 0.01 M. The screening of the fixed charges at these concentrations is relatively weak everywhere in the pore, and therefore the resulting values for V_{rev} are close to that for an ideally selective pore (Nernst value). This is due to the fact that the relatively low Donnan potential drop for arrangement 2 at the left interface is counterbalanced by an even higher one at the right, where the pore tip is in contact with the low concentration 0.01 M.

In Fig. 50(c), the concentration on the right-hand side of the pore is 1 M, which leads to almost complete shielding of the pore wall charges, especially for arrangement 2. But even when this high concentration is placed at the small opening of the pore, it leads to only a small Donnan potential. The diffusion potentials are also quite small for both arrangements, thus the big difference between $V_{D,L}^{(1)}$ and $V_{D,L}^{(2)}$ explains differences for $\log_{10}(c_R/c_L) > 0$ in Fig. 48(b).

These calculations were applied to the pore used for the experiments in section 5.2 (see Fig. 51(b)). The value for σ used in the calculations has been obtained from a fit to the $I - V$ curve (Fig. 51(a)). Additionally, one can calculate the corresponding transference numbers and compare them with the experimental results (see Fig. 52). As expected, t_+, i. e., the selectivity of the pore, is higher for the cases where the low concentration is facing the pore tip ($\log_{10}(c_R/c_L) < 0$ for arrangement 2 and $\log_{10}(c_R/c_L) > 0$ for arrangement 1). The results presented here show that the simple PNP model described above is able to reproduce the asymmetries in V_{rev} found experimentally that occur depending on the direction of a concentration gradient. However, as suggested in [32], it would be interesting to perform measurements of the cation selectivity under different applied voltages, because the model predicts a much higher selectivity for negative compared to positive voltages (Fig. 53). To do this, one could for example use radioactive-marked ions and observe their transport through the pores for different applied potentials.

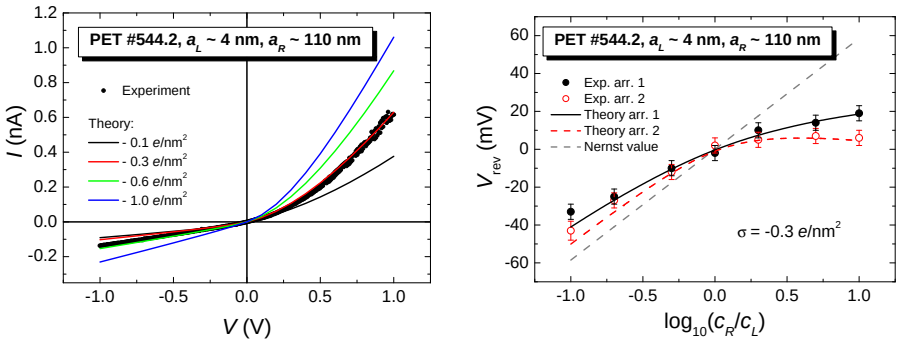

(a) (b)

Figure 51. a) Calculated $I - V$ curve fitted to experimental data to obtain σ b) Comparison of measured and calculated values of V_{rev}.

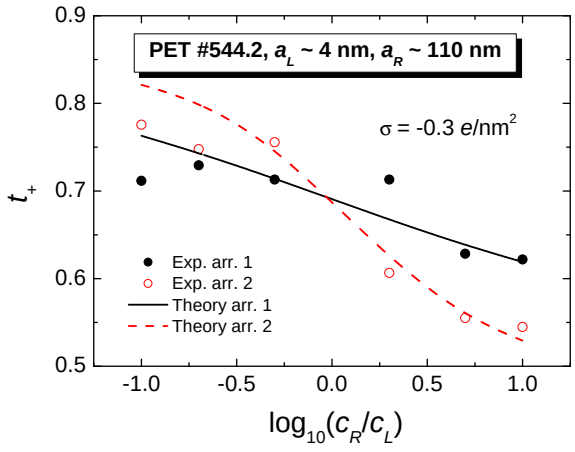

Figure 52. Comparison of measured and calculated transference numbers.

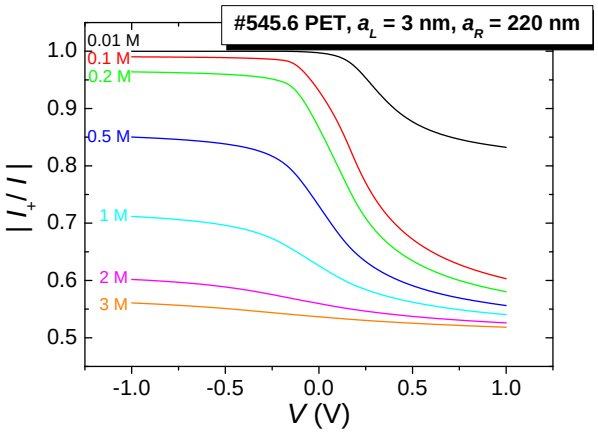

Figure 53. Fraction of total current transported by cations at different applied voltages parametric in the electrolyte concentration. Calculated with PNP model for sample #545.6, using a value of $\sigma = -1\ e/\mathrm{nm}^2$ as in Fig. 36. The values for this fraction, i. e., the selectivity, are higher for negative voltages than for positive ones.

6 EFFECT OF DIVALENT CATIONS

Besides effects like current rectification or selectivity, another typical feature of biological ion channels is their ability to react, e. g., open and close, to the presence of different ions. A well-known example is the blockage of voltage-gated channels by small concentrations of extracellular divalent cations [1, 106], e. g., by binding to negative charges on the pore walls and thereby changing the electric field inside the pore or by occupying binding sites inside a channel which must be held by monovalent cations to keep the channel open. Since synthetic nanopores are sometimes regarded as models for biological ion channels or even future candidates to 'mimic' such channels, a very interesting question is whether they are also able to distinguish between different ionic species, especially whether and how they react to the presence of divalent cations such as Ca^{2+}.

6.1 NEGATIVE RESISTANCE AND FLUCTUATIONS IN PET PORES

It has indeed been found that the flux through track-etched nanopores can be inhibited by protons and divalent cations [78, 98, 100, 107], and recently it was discovered that single conical nanopores in PET show an effect called negative incremental resistance [108, 109] in the presence of micro- to millimolar concentrations of $CaCl_2$. This terminology describes the fact that in a certain voltage range for increasing voltages the current does not increase, but decrease, contrary to normal ohmic behavior. A schematic of this effect is shown in Fig. 54. In the nanopore system this

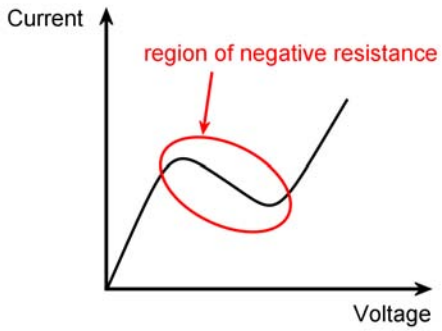

Figure 54. Schematic of an effect called negative resistance, where the current decreases with increasing applied voltage, in contrast to Ohm's law.

happens only for one polarity, namely positive potential applied to the tip of the pore. The voltage at which this effect occurs, depends on the calcium concentration (lower voltages for higher concentrations) and for concentrations of about 1 mM $CaCl_2$ the pore is effectively blocked for all voltages $V > 0$, i. e., positive potential on the small opening of the pore. An example of this effect for a PET pore is shown in Fig. 55 [108] (Here, the $I - V$ curve is inverted relative to the other plots in this thesis).

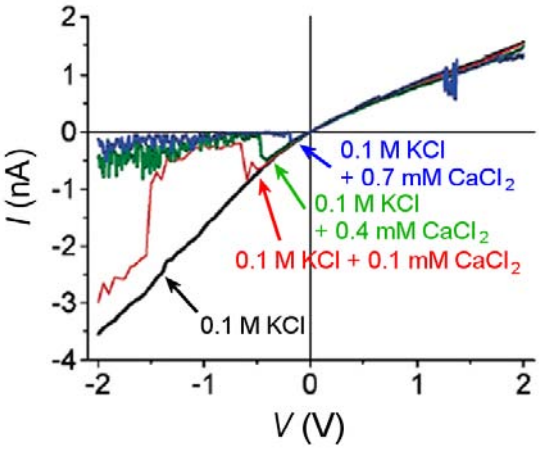

Figure 55. The effect of calcium on the $I - V$ curve of a conical pore in PET, $d \sim 5$ nm and $D \sim 890$ nm [108]. The black curve is the $I - V$ curve at 0.1 M KCl without the addition of calcium. The red, green and blue curves correspond to addition of $CaCl_2$ of 0.1, 0.4 and 0.7 mM respectively. The arrows indicate the occurrence of the negative resistance.

The effect is strongly pH dependent: it occurs only in buffered solutions (e. g., 2 mM phosphate buffer (PB), pH 8 in [108]) of pH greater than or equal to neutral, lowering the pH to 6 resulted in normal $I - V$ curves (see also Fig. 59(a)). Because lowering the pH reduces the charges on the pore walls, this is a strong hint to assume electrostatic interactions between the divalent cations and these negative charges to be involved in the effect.

By looking closer at the current-time traces for voltages in the region of the negative incremental resistance, it was found that the pore is not constantly blocked, but shows voltage dependent oscillatory fluctuations between open and closed states [110]. The time scale of these oscillations depends on the species of divalent cation used, e. g., for Mn^{2+} the pore is much less frequently in the open state than for Ca^{2+}. Frequencies of the oscillation range from tens of Hz to sub-Hz.

The occurrence of such oscillations induced by divalent cations in synthetic nanoporous systems is of great interest from several points of view. Oscillatory processes are essential in many physiological processes,

one of the most obvious being the regular heart rate. Oscillations in transmembrane current or voltage are involved in the transduction of nerve impulses and action potential. Regular oscillations in intracellular calcium concentrations are associated with many of these processes [111], and therefore there is growing interest in building a controllable inorganic calcium oscillator [112]. Also, biological channels are known to show negative incremental resistance and current instabilities induced by divalent cations [35, 36]. Due to this ubiquity of oscillatory systems in nature, understanding the mechanisms of such processes is of common interest. A lot of electrochemical reaction systems are also known to exhibit instabilities or self-organized spatiotemporal periodicities [113–115]. These systems operate far from equilibrium and usually involve a negative impedance characteristic [116]—both points are also true for the nanopore system with added calcium, which is studied here. An interesting feature of the fluctuations occurring in the nanopore is their frequency, which can be tens of Hz and thus much higher than most of the frequencies of chemical oscillators, which are usually below 1 Hz. This is probably due to the much smaller volume in which the reactions occur, allowing for a much faster response.

A first attempt to explain the calcium induced fluctuations was made by Siwy et al. [110] soon after the discovery of the effect. They suggested a mechanism based on charging and uncharging of the pore walls due to temporary binding of the calcium ions to the negatively charged COO^- groups on the pore walls. This leads to changes of the intrinsic pore potential at a time scale comparable to the time a K^+ ion needs to traverse the pore and can therefore lead to changes in the potassium current. It is known that divalent cations form complexes with EDTA, a molecule having four carboxyl groups in the center, thus reaching a density of COO^- groups comparable to that present on the pore walls. From this chemical system, binding constants for different divalent cations are known, e. g., the binding constant for manganese ion is three orders of magnitude larger than that for calcium [110]. Therefore it is reasonable that the frequency of the fluctuations in the presence of Mn^{2+} is much lower.

More recently, another possible origin of the current fluctuations was worked out [117]. Precipitation reactions inside the nanopore could lead to its blocking, and dissolving of the precipitates would result in current increases. Due to the presence of phosphates in the solution[1], there exists the possibility to form $Ca(HPO_4)$ or $Ca(H_2PO_4)_2$. These salts have the solubility products $\approx 5 \cdot 10^{-6}$ for $Ca(HPO_4)$ [118] and $\approx 10^{-13}$ for $Ca(H_2PO_4)_2$ [119]. The solubility product K_{sp} of a salt A_rB_s is defined as $K_{sp} = [A]^r[B]^s$, where [A] and [B] are the concentrations of ions A and B in mol/l [103]. This means the salt will precipitate as soon as the product of the concentrations of its constituents exceeds the solubility product. While the

1 Phosphate buffer was used in all experiments.

concentrations of calcium and phosphates used here are too low to cause precipitation in the bulk solution, the situation inside the nanopore can be quite different. Due to the negative charges on the inner pore wall, the concentration of positive ions inside the pore near the tip of the pore can increase enormously compared to the bulk concentration, depending on the applied potential. This was shown as a result of PNP modeling for the concentrations of potassium ions inside the pore in section 4.3.2. In Fig. 56 an example of the calculated concentration profile for cations inside a pore with $d \sim 6$ nm and $D \sim 440$ nm (#545.6, see Fig. 36) is again shown. Similar calculations can be performed for the Ca^{2+} concentration,

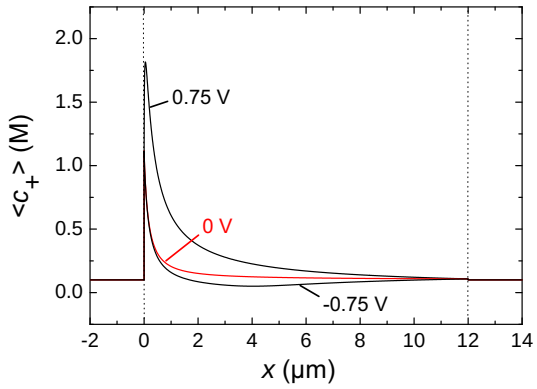

Figure 56. Concentration profile of cations inside a pore with $d \sim 6$ nm and $D \sim 440$ nm at a bulk solution concentration of $c_0 = 0.1$ M, calculated with the PNP formalism.

and lead also to voltage dependent elevated concentrations inside the pore [117].

6.2 VOLTAGE-DEPENDENT FLUCTUATIONS IN POLYIMIDE PORES

Our interest was now to check if the effects described above also occurred in pores of the same conical geometry but different material, such as the Kapton pores, which are known to exhibit a very stable ion current (making them ideal candidates for the detection of single molecules (see chapter 7)) and which give more reproducible results compared to PET pores, probably due to the smoother surface of the polymer (cross sections of membranes containing 10^8 pores/cm² are shown in Fig. 57). Another possible reason for this is that the PET used here has a semi-crystalline structure, so pores might behave differently when created in either amorphous or crystalline regions. The polyimide on the other hand is totally amorphous.

Another open question was, how the observed oscillations would behave under higher applied voltages, since the measurements in [110]

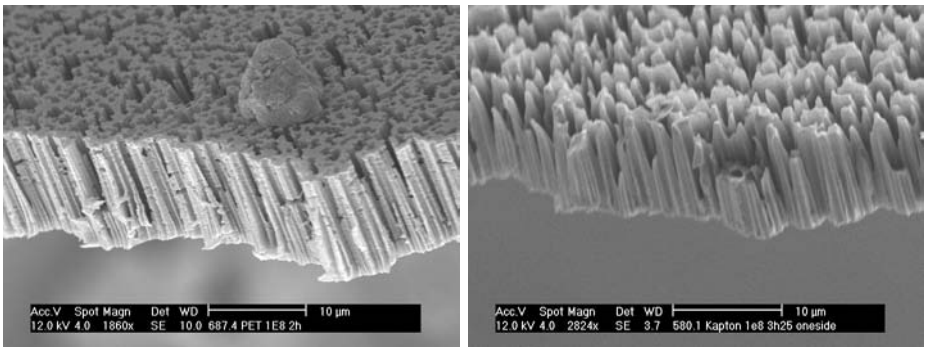

(a) (b)

Figure 57. a) Cross section through PET membrane with conical pores b) cross section through Kapton membrane with conical pores. A lot of air bubbles are present in the PET membrane, resulting from the production process.

had been performed only up to 1 V due to technical reasons.

The setup used for these measurements was the following: The current traces were recorded by an Axopatch 200B patch-clamp amplifier, filtered at 10 kHz and digitized by a Measurement Devices card PCI-DAS 4020/12 at 50 kHz. The voltage was not applied by the Axopatch amplifier, but by a Keithley 6487 picoamperemeter/source, connected to the ground of the Axon. QuB [120], a software package for ion channel recordings was used for data collection. Histograms, power spectra and idealized data were also calculated using QuB.

The electrolytic cell was the same as used for the measurements in chapters 4 and 5.

The measurements performed with Kapton pores clearly show that the pores' reactions to small concentrations of Ca^{2+} are indeed similar to the observations made with PET pores. They show the same negative incremental resistance as well as voltage-dependent oscillations between open and closed states. In general, it can be said that for low positive voltages in the region where the negative resistance occurs, the pore is mainly in the closed state. For increasing voltages, more and more fluctuations to the open state occur, finally reaching a region were these fluctuations become ordered oscillations. If the voltage is increased further, this regular behavior vanishes, while the amplitudes of the fluctuations become higher and higher. Finally a region is reached were the pore is mostly in the open state again, however the mean current is still reduced compared to the situation without calcium.

Examples of the above behaviors are presented below, recorded with sample #161.5, having $D \sim 1.5$ µm and $d \sim 8$ nm. All solutions were buffered to pH 8 with 2 mM sodium phosphate buffer. In Fig. 58, the

$I - V$ curves for this pore in 0.1 M KCl are shown without calcium (black), as well as with the addition of 0.05 mM (red) and 0.4 mM (green) $CaCl_2$. For both concentrations, the current for positive voltages is almost

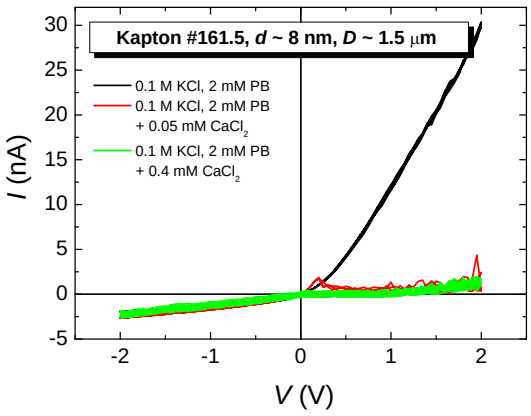

Figure 58. $I - V$ curves for sample #161.5 in 0.1 M KCl, 2 mM PB pH 8 without calcium (black), with addition of 0.05 mM (red) and 0.4 mM (green) $CaCl_2$.

completely blocked, apart from one period of the $I - V$ curve recording for 0.05 mM $CaCl_2$, where the current increases slightly for small positive voltages, before dropping again. A comparison with the $I - V$ curves of the PET sample shown in Fig. 55, which is comparable in size, suggest that Kapton pores react to even lower concentrations of calcium, maybe due to their bigger opening angle or a higher concentration of COO^- groups.

For larger pores, the behavior is more similar to the one presented for the PET pore (Fig. 59). For the lower calcium concentration used here (0.1 mM), the current drop occurs at 0.6 V, while for 0.5 mM it occurs already at 0.3 V and the pore is mainly blocked for voltages higher than 1 V. However, for 0.1 mM the current does not 'jump' back to almost the level without calcium as it did for PET pores, but increases only gradually and reaches only up to 50% of its normal value. It has also been found that in the cases where the current is not blocked too much, the $I - V$ curve follows a hysteresis for positive voltages, as clearly visible in Fig. 59(b). For increasing voltage, the current follows first the normal $I - V$ curve, then there is a drop at a certain voltage, and afterwards the current increases again for low concentrations (0.1 mM, green curve in Fig. 59(b)) or drops even further for higher concentrations (0.5 mM, red curve in Fig. 59(b), 1 mM, blue triangle in Fig. 59(a)). But for the falling edge of the triangular voltage signal the current values are lower over the whole range. This hysteresis behavior has not been reported for PET pores, possibly it has not been observed because only rising voltage

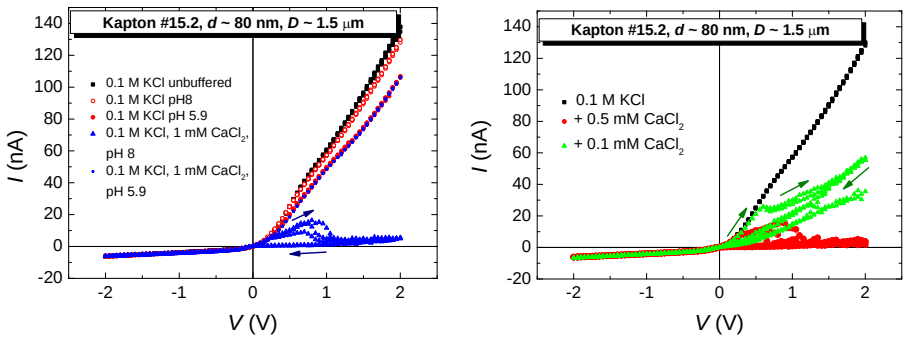

Figure 59. $I - V$ curves for sample #51.2, Kapton, $d \sim 80$ nm, $D \sim 1.5$ µm, all solutions buffered with 2 mM phosphate buffer (Measurement performed by M. Ali, PhD student, GSI) a) Addition of 1 mM $CaCl_2$ reduces the current strongly for $V > 0$ only at pH 8. Calcium has no effect at pH 5.9 b) All measurements at pH 8. Higher concentrations of calcium affect the current at lower voltages. The arrows indicate the direction of the hysteresis.

ramps have been used to record the $I - V$ curves. The reason for this hysteresis is probably that more and more calcium ions enter the pore when increasing the voltage, but when it is decreased, they stay inside and leave the pore only when negative voltages are applied again.

No effect on the $I - V$ curve was found, when not adjusting the pH of the solution with phosphate buffer, but only using NaOH (see Fig. 60).

To study the current at different voltages with high time resolution, current traces of at least 1 minute have been recorded for positive voltages in steps of 0.1 V in the case of calcium added and in steps of 0.2–0.5 V without calcium. Fig. 61 shows 1 s long current traces recorded at a) 0.2, b) 0.7, c) 1, d) 1.5 and e) 2 V in 0.1 M KCl. The insets show a histogram and power spectrum of a 1 minute long recording. The regular downward spikes in the current, corresponding to the peak at 50 Hz in the power spectrum for 0.2 V, originate from power line interference, related to the CRT monitor used at that time. Later replacement with a flat-screen LCD eliminated the problem. The peak visible in all power spectra at about 2 kHz is caused by an oscilloscope through which the signal was carried before it reached the measurement card. The setup was not changed, because it is very useful to view the signal on the oscilloscope parallel to recording, and no relevant signals in this frequency range are expected in the data.

It can be seen that the current distribution becomes wider for higher voltages, correlated to an increase in low frequency noise as visible in the power spectra, which is the typical behavior of these pores.

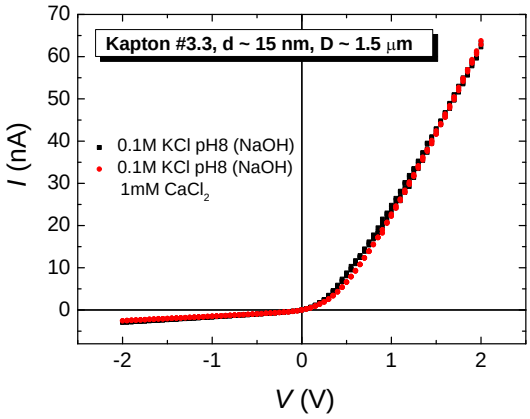

Figure 60. $I - V$ curves for sample #3.3 in 0.1 M KCl, adjusted to pH 8 with NaOH and without calcium (black squares) and with the addition of 1 mM $CaCl_2$ (red dots).

The measurements for 0.04 mM $CaCl_2$ added ($I - V$ curve in Fig. 58, green curve) are shown in Fig. 62. Again, representative current-time traces of 1 s (or less if a higher magnification is needed) for different voltages are presented. Histograms and power spectra have been produced for 1 min long recordings at 0.2, 0.7, 1.6 and 1.8 V. Because of the more irregular structure of the current signal, longer segments (3 min for 1 and 1.2 V; 100 s for 1.4 V) have been used at intermediate voltages.

As can be seen from subfigures (a) and (b), the pore is essentially blocked for voltages below 1 V. Again, the spikes from the monitor and oscilloscope can be seen in the power spectra. At 1 V, fluctuations similar to those found in PET in the presence of $CaCl_2$ start to appear. Their height is up to 1 nA and their duration about 5–12 ms, reflected by the appearance of a shoulder around 100 Hz in the spectrum. By increasing the voltage further, the peaks become higher, while their length stays approximately the same. A very interesting effect is that they also become more frequent, appear in more regular intervals and in general become more uniform. This ordering behavior can also be followed in the power spectrum, were the shoulder develops into a broad peak at about 50–60 Hz. For comparison, Fig. 63 and 66 show the results for the second, much lower concentration of $CaCl_2$ (0.05 mM) used here, which resulted in an $I - V$ curve very similar to the one with 0.4 mM (Fig. 58, red curve). The effects which occur on the lower timescale are indeed similar, but a more detailed analysis reveals also some differences. The occurrence of the peaks happens more gradually and at relatively low voltages ($V \leq 1.2$ V). They are also less uniform and in general longer (about 20–50 ms) than those recorded at the same voltages with higher calcium concentration. But despite this quite irregular behavior in

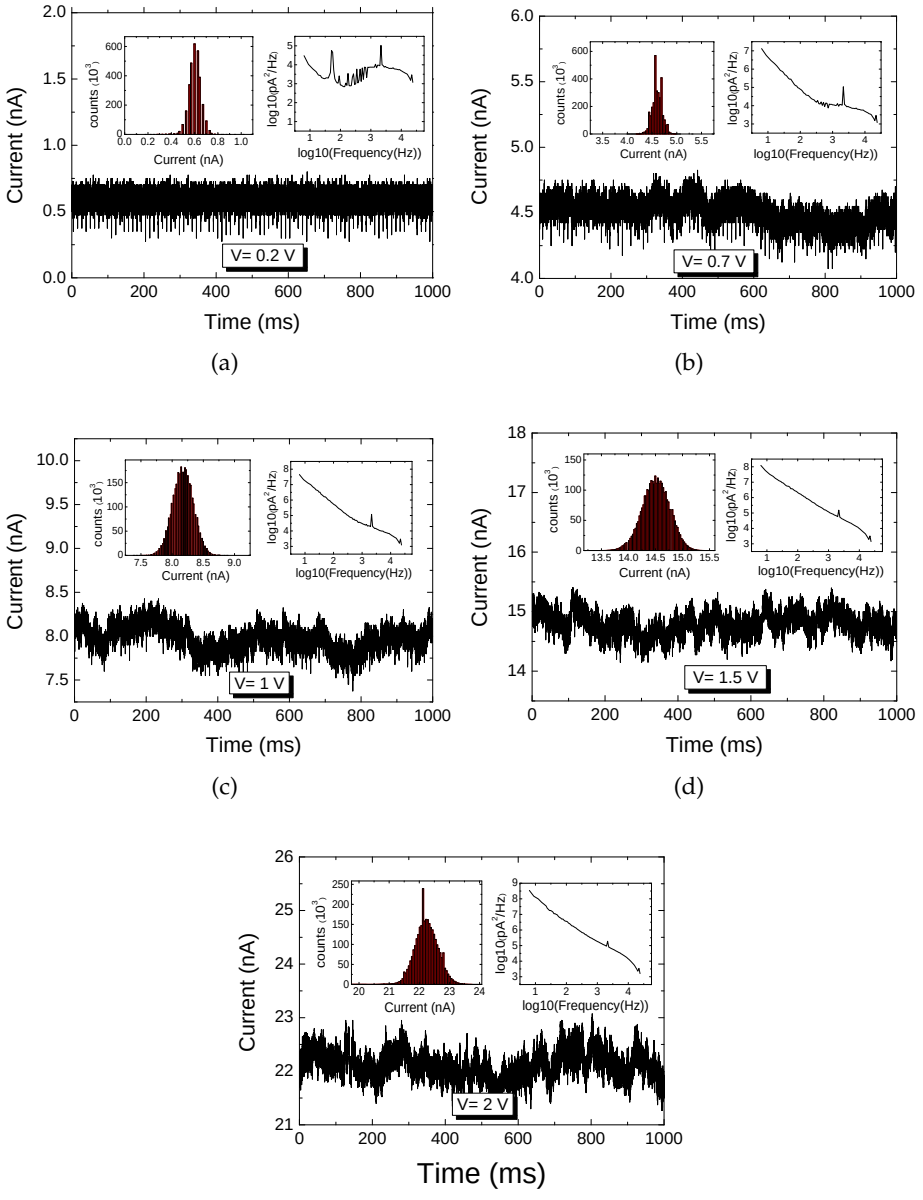

Figure 61. Current traces of 1 s for sample #161.5, recorded at a) 0.2, b) 0.7, c) 1, d) 1.5 and e) 2 V in 0.1 M KCl. The insets show a histogram and power spectrum of a 1 minute long recording.

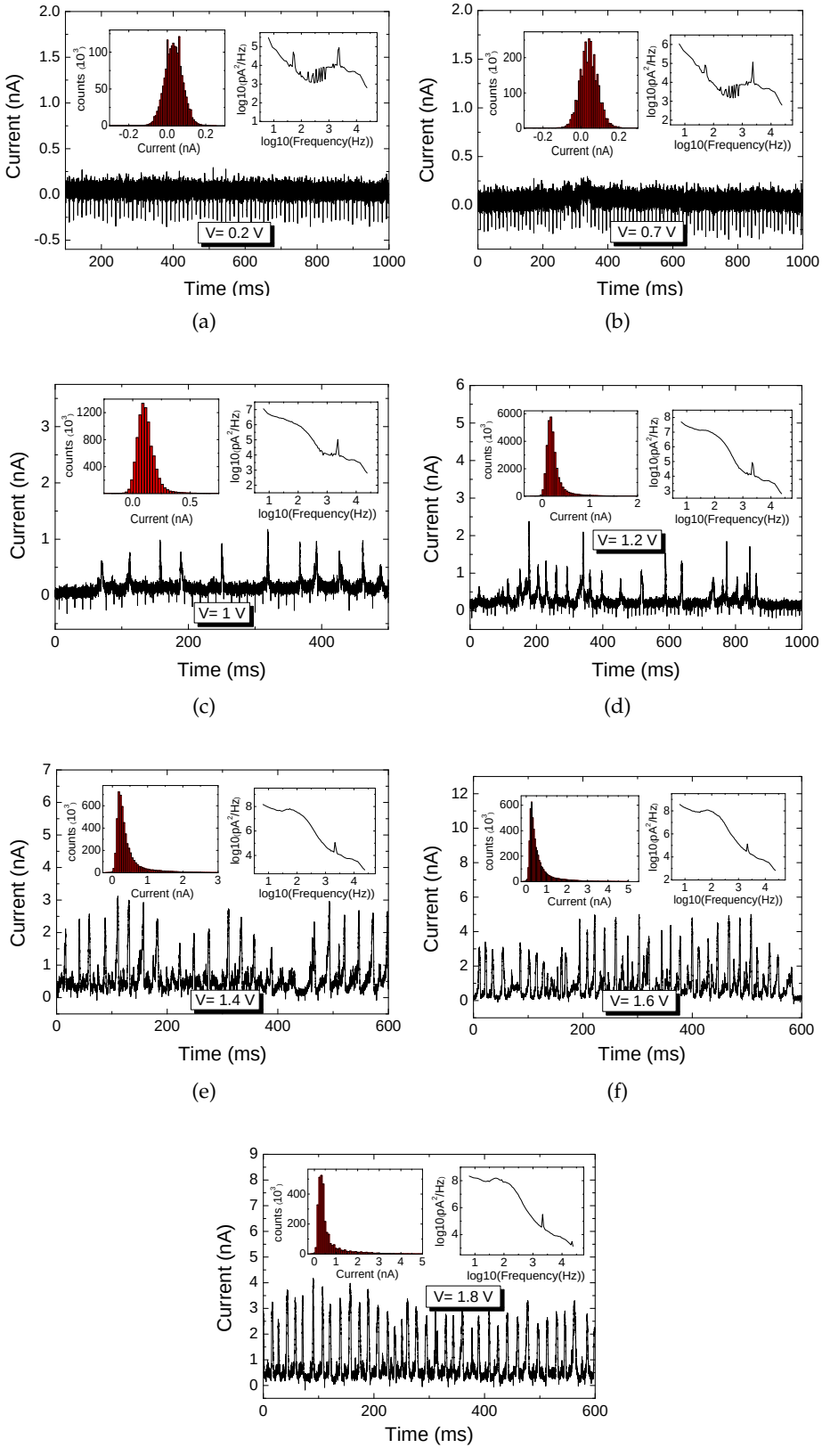

Figure 62. Current traces, current histograms and power spectra for sample #161.5, recorded in 0.1 M KCl, 0.4 mM $CaCl_2$ at a) 0.2, b) 0.7, c) 1, d) 1.2, e) 1.4, f) 1.6 and g) 1.8 V.

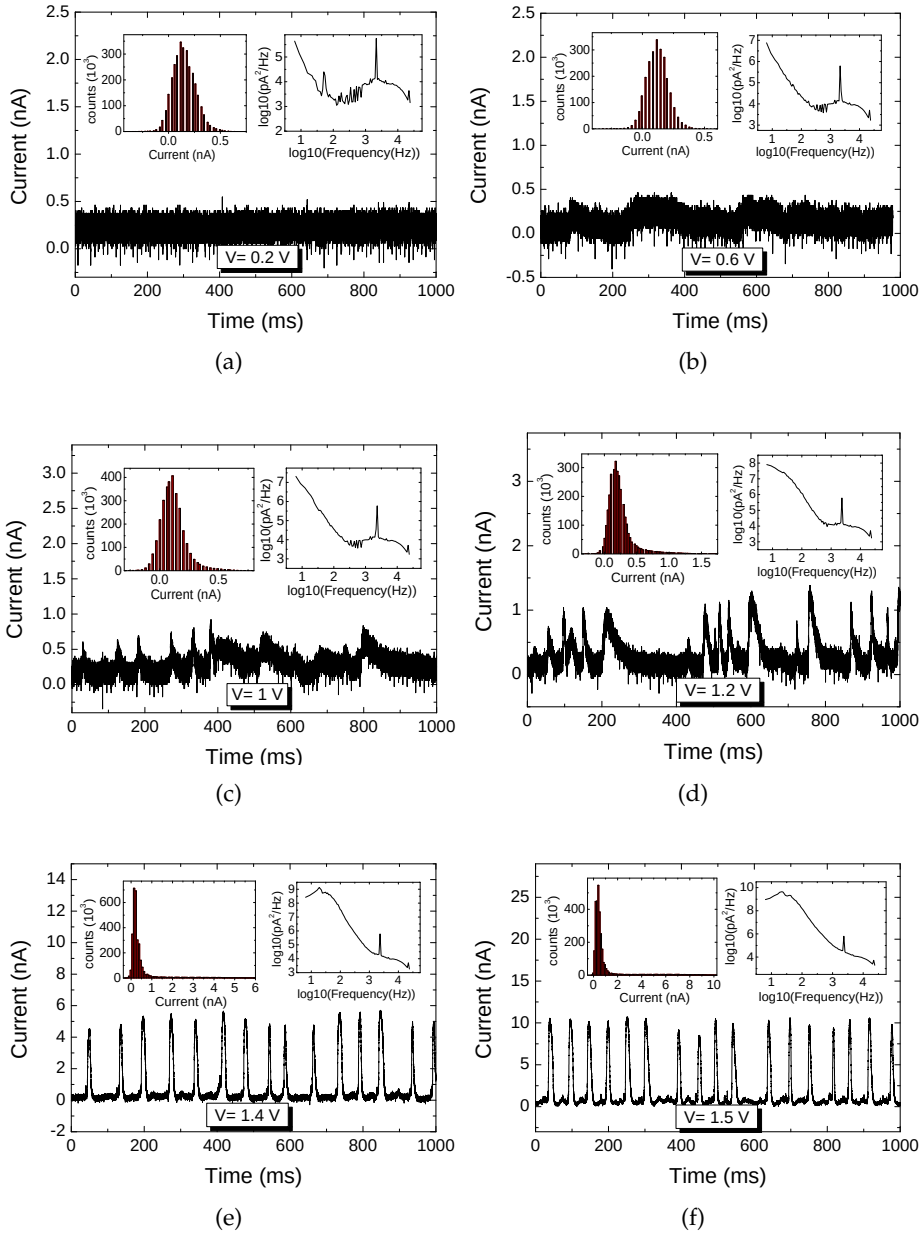

Figure 63. Current traces, current histograms and power spectra for sample #161.5, recorded in 0.1 M KCl, 0.05 mM $CaCl_2$ at a) 0.2, b) 0.6, c) 1, d) 1.2, e) 1.4 and f) 1.6 V.

the lower voltage range, the peaks become suddenly very well ordered at 1.4 and 1.5 V. To further analyze this striking behavior, a histogram of the duration times of the peaks have been calculated for these two voltages. The results are shown in Fig. 64. To achieve this, the data have first been idealized using a two state (open-close) model. The result of this idealization is shown as an example for the first 6 peaks from Fig. 63(f) in Fig. 65. The idealization is done in the following way: First, a certain current level has to be assigned to the open and the closed state respectively, then the mean of these two values is used as a threshold to assign each data point to one of the states. The same values for open and closed state have been used for 1.4 and 1.5 V, therefore in Fig. 65 the idealized peaks are lower than the measured ones. In Fig. 64(a), there are a number of very short (< 1 ms) events visible in the histogram, these result from peaks which are only slightly higher than the value chosen as open state and therefore classified as too short. Due to the shape of the peaks which are not square like, it is difficult to decide what to take as open state and what to define as duration. A good compromise was found by taking the duration at half the amplitude, but since the idealization is not done separately for each peak and they still show some variation in height, there will be always a certain error. By measuring the width in the upper and lower third for several peaks at 1.4 and 1.5 V, this error can be estimated to be about ± 3 ms.

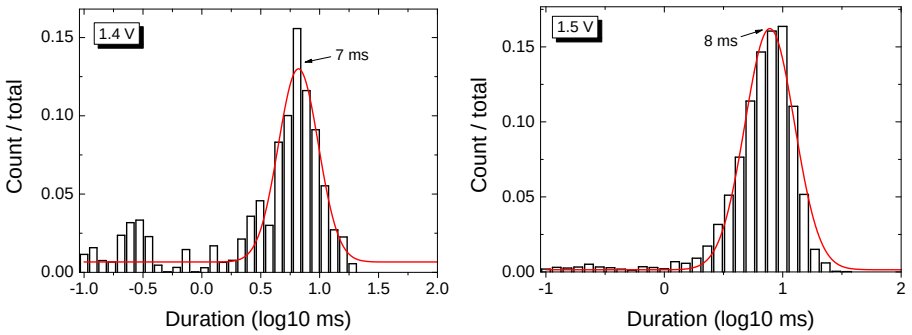

(a) (b)

Figure 64. Histograms of the duration of the fluctuations for 1.4 and 1.5 V, extracted from the idealization shown in Fig. 65. The red curves are Gaussian fits to the histograms to obtain the most probable duration.

The time scales of the peaks are very similar for 1.4 and 1.5 V, but their mean amplitude has increased by a factor of about two from 1.4 to 1.5 V, reaching 2/3 of the current recorded without calcium. This is a clear difference to the results with 0.4 mM $CaCl_2$, where even the most regular fluctuations at 1.8 V were not higher than about 4 nA, compared to about 20 nA without calcium.

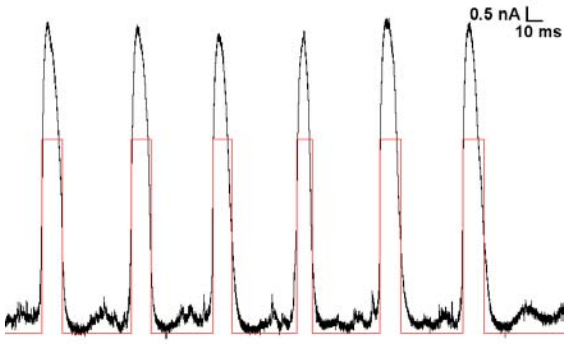

Figure 65. Result of the idealization with a two state model done in QuB for the first 6 peaks from Fig. 63 f) in Fig. 65. The red curve shows the idealized data which are used as basis for the duration histograms in Fig. 64.

It has to be mentioned that the fluctuations at 1.5 V were not as stable as reported for PET [108], they disappeared after several minutes, leaving the pore in the closed state with only very few irregular openings up to 2 V. They could be restored by reversing the voltage to –2 V for a short time and then showed exactly the same properties at positive voltages as before. But again they stopped after some time, however this time, when increasing the voltage up to 2 V the fluctuations occurred anew, with the characteristics described in the following. The long-term stability of the fluctuations should be examined in the future in more detail under various conditions.

Since the current with this low concentration of calcium seems to be especially voltage sensitive, measurements up to 4 V have been performed (Fig. 66). For these higher voltages the appearance of the fluctuations changes substantially. For 2 V, the majority of them now has two open states, one being about 100% of the normal current, the other about 40%. This second state is also visible in the histogram, which no longer has only a long tail extending to higher currents, but a small broad peak appears at the level of the lower open state. Overall, the pore now spends more time in the open state. This tendency continues for even higher voltages. For 2.5, 3 and 4 V, the fluctuations become much longer (note the different scales on the x-axis in Fig. 66 h), i) and j)), reaching finally a duration of several seconds at 4 V.

The development of the amplitudes is not as simple. While the peak values of the fluctuations are highest between 2.5 and 3 V and decrease again for higher voltages, the mean value of the current is steadily increasing with voltage and at 4 V the pore spends most of the time in an intermediate state, closing only for very short periods. A similar behavior has been found for other samples; it seems that even for quite

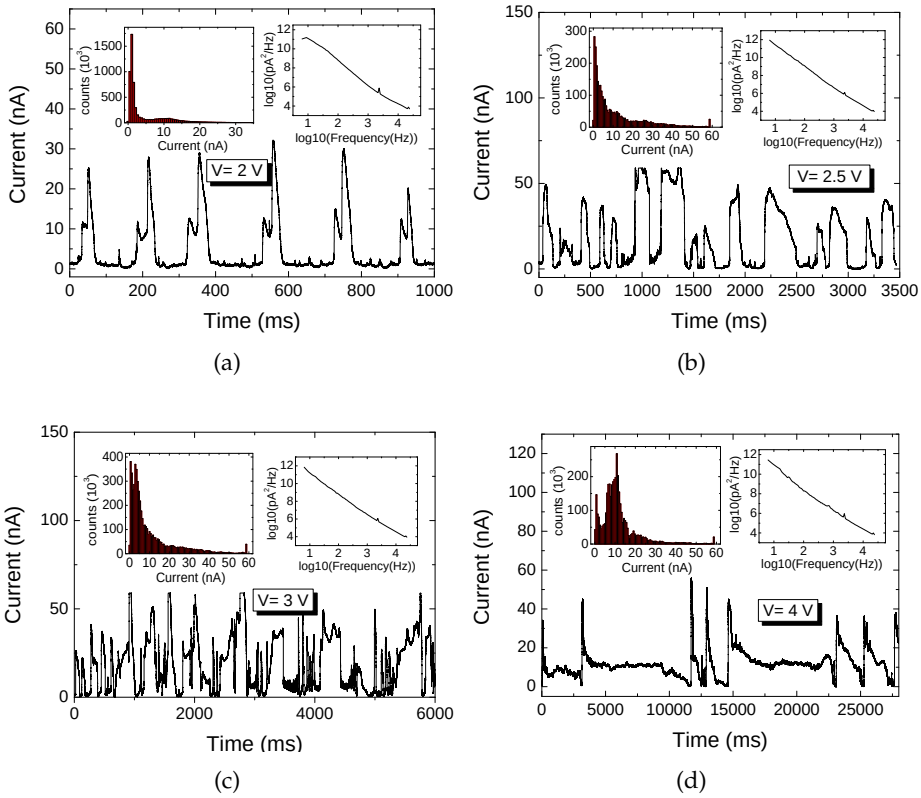

Figure 66. Current traces, current histograms and power spectra for sample #161.5, recorded in 0.1 M KCl, 0.05 mM $CaCl_2$ at a) 2, b) 2.5, c) 3, and d) 4 V.

high voltages the pore does not reach constantly the same current as without calcium.

Understanding the dynamics of this voltage dependence is still a challenge, and more systematic measurements are needed to further clarify the underlying mechanisms, leading to the oscillation-like fluctuations which are observed at certain 'optimal' voltages. One step in this direction could be to test the importance of the presence of carboxyl groups in the system by using a chemically modified pore, having different negatively charged groups on the surface [117].

7 NANOPORES AS SINGLE-MOLECULE DETECTORS

7.1 BACKGROUND

Probably one of the most interesting recent applications of nanopores is the possibility to use them as detectors and even analyzers for single (bio)molecules. The basic idea behind this is very simple and already rather old. In the 1950's, Wallace Coulter patented a method to count single particles (e. g., cells) in solution as they pass through a small aperture, which resulted in a device today known as the 'Coulter-counter' [121]. The principle of this system is to place the aperture in an electrolyte solution, containing the particles to count only on one side, and then constantly measure the conductance of the aperture. Assuming the conductivity of the particles differs from that of the electrolyte solution, then as they move through the aperture, e. g., by diffusion or driven by an external pressure gradient, they will cause a change in conductance and thus can be detected.

The original system was limited to particles in the micrometer range as smaller apertures had not been produced at that time, but in the 1970's Ralph W. DeBlois and Charles P. Bean extended it to submicron sized particles by using a single pore of a few hundred nanometers in diameter, produced by the track-etching technique, which was still in its early stages at that time [122, 123]. They successfully applied their system to particles (latex spheres, bacteriophages) as small as 90 nm diameter and not only used it for counting them, but were able to extract information, e. g., as the electrophoretic mobility or the size of the passing particle from characteristics such as height or duration of the electric signals.

Another 20 years later, David Deamer came up with the idea of characterizing linear polymers like DNA with nanopores using the same concept. The idea was first realized in 1996 using the pore-forming protein α-hemolysin[1] as the nanopore [10] and patented in 1998 [124].

The principle of such an experiment is shown in Fig. 67. Since DNA molecules are negatively charged at physiological pH values (the phosphate groups in the backbone of DNA molecules are deprotonated), they can be driven electrophoretically through the pore, thereby partially blocking the ionic current flowing through it during the time of their passage. Detailed analysis of the characteristics of these current blockades (called 'events') can reveal information about the molecule translocating

1 Extracted from the bacterium *Staphylococcus aureus*, which uses this protein to attack cells, in order to damage or kill them by causing the leakage of water, ions and other molecules through the pore.

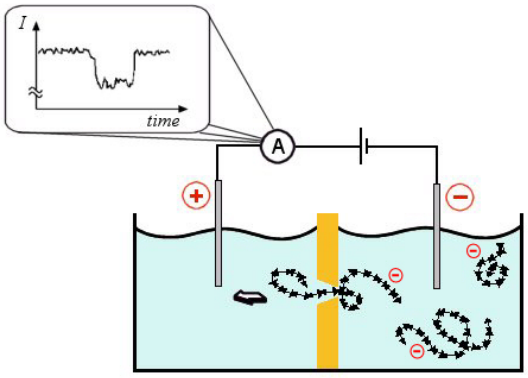

Figure 67. Schematic of a DNA detection experiment using a nanopore: negatively charged DNA molecules are driven through the pore by an electric field and partially block the ionic current flowing through the pore during the time of their passage.

the pore.

7.1.1 *α-hemolysin*

Until now a lot of work has been done in this field by different groups using α-hemolysin. This protein forms a well-defined pore with a limiting aperture of 1.5 nm diameter in a lipid bilayer, by self-assembling from seven subunits. At low protein concentrations in the solution, it takes tens of minutes until one pore is inserted [11], which can therefore easily be detected by an increase in current and the insertion of a second pore can be avoided by flushing the measurement cell with buffer solution. α-hemolysin was chosen due to its well-known structure [125] and comparably high steady ionic current (∼ 100 pA at 100 mV [9]), which facilitates measurements. Due to the limiting aperture of 1.5 nm, double stranded (ds) DNA, which has a diameter of 2 nm is not able to pass through it, therefore the work concentrated on single stranded (ss) RNA and DNA. This includes

- discrimination between different homopolymer species (such as poly(A), poly(C), poly(U)) [11, 12, 126] based on characteristic event depths and durations
- effects of secondary structures of DNA and RNA [11, 127]
- discrimination between single-nucleotide/single-base pair differences [14] in ssDNA or DNA hairpin molecules[2] [128]. The double

2 ssDNA molecules with a loop at one end forming a double stranded part of a few bases.

stranded part can not fit into the pore but is dissociated (unzipped) after a characteristic time or at a certain applied voltage

- orientation discrimination of ssDNA and RNA [129, 130]
- studies of unzipping kinetics of dsDNA [131–134]

This large amount of results indicates the potential of α-hemolysin, whose structure is very well known down to the molecular level [125] and happens to match the needs for single molecule analysis. However, there are some disadvantages, limiting the applicability of this technique. These are mainly the relatively short lifetime ($\sim$36 h) originating from the fragility of the lipid bilayer, which makes the system improper for commercialization, as well as the sensitivity to the external experimental conditions, such as temperature, high and low pH values or high electric fields.

7.1.2 *Solid state nanopores*

In the recent years, a lot of work has been done to overcome these shortcomings, starting from improving the existing system, e. g., by using more stable supported lipid bilayers [135, 136], but mainly by developing solid state nanopores. Although these are not trivial to produce with high precision and reproducibility in the range of a few nanometer, their advantage besides higher stability is the possibility to tailor pore sizes and shapes to match the needs of different experiments.

Besides the track-etching technique described here (see chapter 2), a variety of different methods have been developed in recent years to create nanopores. Currently, the most popular class of methods start with a relatively large pore (several tens of nanometers) in thin (a few tens of nanometers) SiO_2 or Si_3N_4 membranes. This large pore is then shrunk using a diffuse ion beam or the electron beam of a transmission electron microscope (TEM). This effect was first observed by Li et al. [19] in 2001 using the ion beam, while the TEM technique was developed by Storm et al. [22] in 2003. A number of groups are nowadays using variations of these techniques [25, 26, 137–139].

A similar shrinking effect was found in silicon using a field-emission SEM [140] and using lasers in thermoplastic membranes [141].

Another way to reduce the size of a relatively large pore drilled by focused ion beam, is subsequent material deposition, as done by Danelon et al. [142] with silicon dioxide.

Recently, focused ion [25] and electron [140] beams have also been used to directly create pores of a few nanometers in diameter in SiC and Si_3N_4 membranes respectively.

In the methods which induce shrinking of larger pores, the pore size development can be observed online by either collecting and counting

the transmitted ions in the case of ion-beam sculpting or obtaining a direct image of the pore in the TEM approach. Also the pores created directly by ion or electron beams can be monitored by TEM; in the case of the ion beam method, the position of the pore is marked by a cross, which is created by slightly thinning the material also with the ion beam. Compared to these methods, which result in pores of well-known sizes, a disadvantage of conical track-etched pores is the difficulty to accurately determine the actual diameter of the small pore opening, which has to be done by conductivity measurements assuming a perfect conical geometry. But their main potential advantage is probably the material they are made in, since polymers open the possibility to directly chemically modify the pores' surface properties and thereby influence their interaction with different analytes. They are also stable over a long time (weeks to months) when kept in water for storage and are very easy to handle. Also, wettability is usually not a problem, in contrast to some of the silicon based pores [26, 140, 143, 144].

Most of the pores described above have been successfully applied to single molecule experiments, mainly dealing with dsDNA due to its larger diameter, since it is still a challenge to reproducibly manufacture pores in the range 1–2 nm.

Most of the early work with solid-state nanopores (including the first experiments using track-etched pores [24]) has dealt with length discrimination of dsDNA, based on histograms of the translocation event durations. While it was possible to observe corresponding peaks in the histograms for all the experiments, essentially non-overlapping peaks could be found only for DNA fragments of lengths differing by several thousand base pairs (bp) [144, 145]. The smallest length difference detected up to now is 500 bp (170 nm) [146].

Some other interesting experiments that have been carried out with solid state pores include

- studies of DNA folding during translocation, which can be detected by different event depths (or different blockage levels in one event), corresponding to molecules translocating unfolded and single or even multiple folded molecules [144]. This behavior is best visible when using very long DNA such as the λ-phage DNA, being 48.5 kbp (∼16.5 µm) in length [143, 147].

- field strength and length dependence of the electrophoretic mobility [147] (found to be independent).

- determination of the effective charge of DNA by measuring the voltage dependent force acting on it in a nanopore [148]. This was achieved by coupling λ-DNA to a large (∼2 µm) polystyrene bead whose position could be controlled by optical tweezers, thus enabling to insert, hold or remove the DNA in/from the nanopore.

The position of the DNA inside the nanopore was simultaneously recorded by ionic current measurements.

- slowing down the translocation speed of DNA, e. g., by changing the viscosity of the electrolyte solution [149] which is important for space resolved studies on DNA, such as sequencing.
- denaturing of dsDNA at high pH values [150]

An interesting observation made with synthetic nanopores was also that the current reduction during the translocation of a DNA molecule strongly depends on the electrolyte concentration and can even switch to peaks with increased current during translocation for low concentrations [26, 151–153]. This is due to the fact that the quantity measured is the conductance of the pore, and this can be increased at low concentrations due to a cloud of counterions brought into the pore with the negatively charged DNA.

A more detailed review of the work done to date with α-hemolysin as well as with solid state nanopores can be found in [154].

7.2 METHODS

The experimental setup used here was developed in close collaboration with K. Healy, who was doing a PhD in the same field until September 2006 at the University College Cork (UCC) in Ireland [154]. He was especially involved in setting up the electronics and writing software for data recording and analysis, including online and offline detection of square-like DNA translocation events.

7.2.1 *Pores*

Pores used in single molecule detection experiments were produced in polyimide (as described in section 2.2), following the work of Mara et al. [24], due to their stable ion current signal [47] (see also section 2.3.3), which is needed for the detection of small current changes. Several reasons exist to use conical pores for this purpose: First, it is much easier to create truly nanometer sized openings using this method as compared to cylindrical track-etched pores, which require an extremely high ratio of track- to bulk-etch velocity to be opened but not enlarged significantly. Also, the total resistance of a conical pore is much lower than that of a cylindrical one of the same length, resulting in higher currents. This leads to a better signal to noise ratio and also facilitates current measurements. Last but not least it is desirable to have a short 'detection length' (the region of the pore in which the molecule causes a significant change in current signal), to be able to resolve structures distributed along the length of the molecule while it passes through the pore. While this seems

to be impossible to fulfill at first glance with a pore that is 12 µm in length, it is indeed the case for a conical pore of the dimensions used here ($D \sim 1.5$ µm, $d \sim 5$ nm), which has an effective length (the length over which 85% of the resistance is concentrated) of about 200 nm [105] (supporting information). Of course, thinner foils could also be used to create cylindrical pores, but these would be much more difficult to handle.

7.2.2 *Setup*

A special low-volume cell was developed for measurements with DNA, which was based loosely on the design used by Mara et al., modified mainly with respect to the channel alignment to allow for easier filling without bubble creation. The cell (Fig. 68) consists of two halves made of PMMA, one of which has a circular recess of 3 cm diameter in which the polymer membrane is automatically centered. The other half has a matching raised cylinder, so that they hold the membrane in place when clamped together. The channels containing the electrolyte solution are

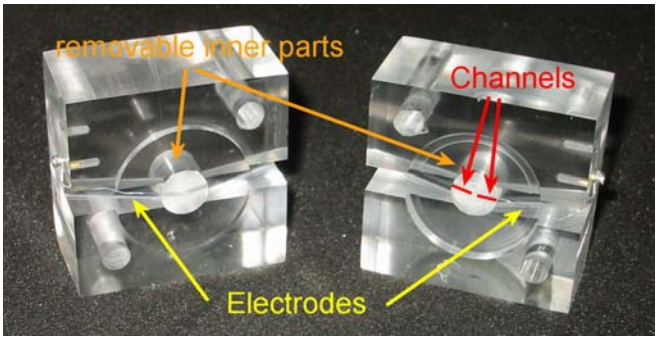

(a)

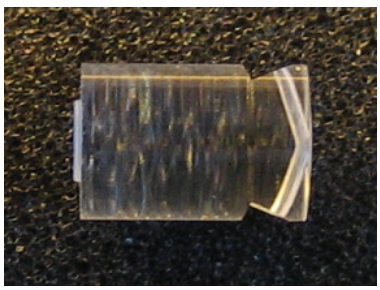

(b)

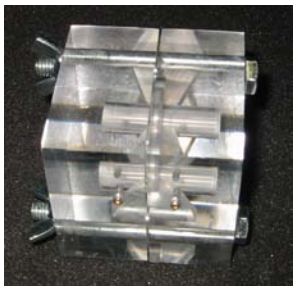

(c)

Figure 68. Pictures of the cell used for DNA detection experiments a) open b) detail of the removable cylinders containing the channels for the electrolyte c) clamped together by screws.

drilled inside removable cylinders placed in the center of both halves of the cell, to facilitate cleaning as well as possible changes in the design. Each channel has a V-like shape with the tip of the V cutting through one of the ends of the cylinder, resulting in a small opening through which the pore comes in contact with the solutions (detail Fig. 68(b)). Each channel is 1 mm in diameter and has a total volume of approx. 8 µl. The cell is pressure sealed using screw-nuts, and thin chlorided silver wires inserted into one end of the channel are used as electrodes.

Data were recorded with the setup described in section 6.2, filtered by the Axopatch 200B at 10 kHz and sampled at 50 kHz. Software written by K. Healy was used for recording.

7.3 RESULTS AND DISCUSSION

7.3.1 *Measurements at low voltages*

The typical voltage range to perform DNA translocation measurements—with α-hemolysin as well as with synthetic pores—is between 100 and 300 mV, with the upper limit in the case of α-hemolysin set by the electrical breakdown of the lipid bilayer at about 500–1000 mV [155]. To allow comparison to the first experiments with track-etched pores [24], a voltage of 300 mV was used here also.

The experiments were performed in a buffered solution of 1 M KCl, 10 mM Tris-HCl, 1 mM EDTA, adjusted to pH 7.5. The DNA used was PhiX174 plasmid, 5386 bp in length, (obtained from G. Becker, Biophysics, GSI). Plasmids are circular double stranded DNA molecules, existing usually in supercoiled form, where the two ends of the dsDNA are joined to a circle but with an additional twist, resulting in a circle that is twisted around itself. If one of the two strands is broken, the circle relaxes, called 'nicked-circle' conformation. Fig. 69 shows an electron micrograph of these two forms of a plasmid, together with the linearized form, which occurs if both strands are broken.

The DNA used here was shown to be in both supercoiled and nicked-circle conformation by gel electrophoresis.

The dimensions of the polyimide pore were $D \sim 2$ µm and $d \sim 20$ nm. A control measurement with only the buffer solution was performed before adding DNA and showed no current blockage events (upper part of Fig. 70). Subsequently, DNA was added to the chamber facing the tip of the pore to a final concentration of about 10 nM. After several minutes—presumably the time the DNA needs to diffuse to the pore—different types of current blockages occurred (lower part Fig. 70). Most of them were of very short duration ($\sim$ 0.1 ms) and were attributed not to real DNA translocations but rather to short collisions of the molecules with the pore opening. A similar effect has been reported by other groups with solid state nanopores [24] as well as with α-hemolysin [12, 127]. The

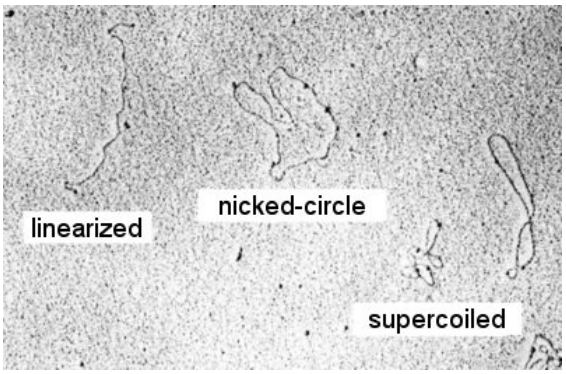

Figure 69. The three conformations of plasmid DNA: supercoiled, nicked-circle (single strand break) and linearized (double strand break). Public Domain picture from wikipedia.de.

events occurred in clusters, possibly the DNA had not yet fully mixed with the buffer solution.

The longer events had various shapes and durations, a few of which are shown in Fig. 71. The scale on the y-axis is the same in all subfigures to visualize the different event depths, while the variation in duration is so big that the scales on the x-axes had to be adjusted. The durations vary from a few to several hundred milliseconds—an extremely long event of more than 1 s is shown in part (d). This variety of event shapes is not surprising due to the different conformations in which the DNA was present and the fact that the pore diameter was rather big compared to the DNA. Therefore, it seems possible that the DNA entered the pore in various configurations, of which some might have been quite compressed and therefore moved faster through the pore, while others had irregular shapes, resulting in a slower passage with varying blockage degrees. Some of the events also show a structure with different sublevels, similar to that observed for the translocation of folded DNA molecules [147].

7.3.2 *Measurements at higher voltages*

One observation with the measurements at low voltages was that they were found to be very hard to reproduce. For reasons yet not fully clarified, many times no events were observed in the presence of DNA. Possible explanations for this are discussed in section 8.5. As a consequence, higher bias voltages were explored in further experiments. For these, the linear double stranded DNA molecules shown in table 1 were used.

VOLTAGE THRESHOLD In the course of these measurements it was found that indeed in several cases current blockages of different shapes

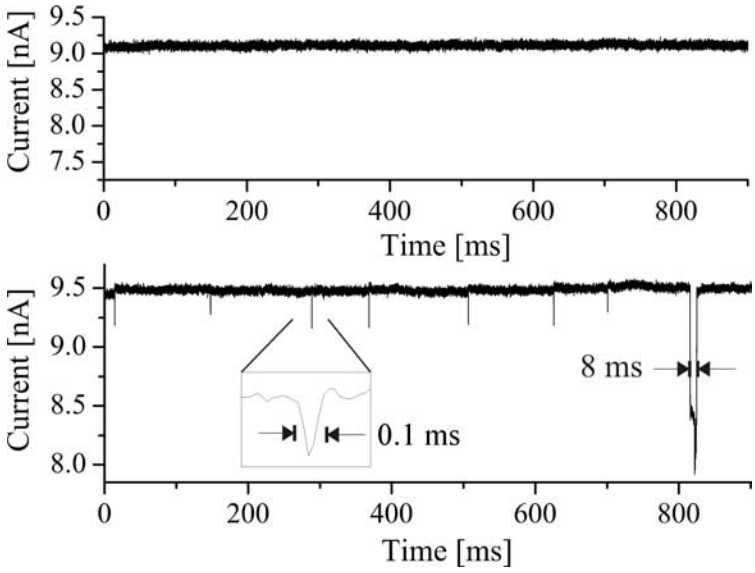

Figure 70. Upper part: reference measurements without DNA show no current blockages comparable to that recorded in the presence of DNA. Lower part: Current trace after addition of PhiX DNA: short decreases in current ($\sim$ 0.1 ms) indicate collisions of DNA molecules with the pore, longer blockages translocation of DNA.

reproducibly occurred above a certain threshold voltage (i. e., they vanished when lowering the voltage and reappeared when rising it again). Some examples for this behavior are shown in Figs. 72–74 for pores of different sizes. Figs. 72 and 74 correspond to measurements performed with nanomolar concentrations of λ-DNA, while the measurement presented in Fig. 73 was done with a solution containing similar weight concentrations (around 20 ng/µl) of dsDNA with lengths 104 and 1215 bp. The threshold voltage was found to vary from pore to pore. While such a high threshold value was not reported up to now, it was found with α-hemolysin that no translocations are observed below a bias voltage of about 60 mV [13], a fact that the authors attributed to an entropic barrier the molecules have to overcome before entering the pore. They suggest that this barrier could arise either from a narrow constriction inside the channel or from electrostatic repulsion between the negatively charged polynucleotides and negative charges present at the narrower end of α-hemolysin. Although the track-etched pores used here are much larger than α-hemolysin (which should result in lower entropic barriers), the presence of a barrier is also expected due to the high number of charges present at the pore entrance. Also, the average electric field strength in the track-etched pores is much lower at similar applied voltages, due to their much longer length. For example a bias voltage of 120 mV with α-hemolysin, which has an effective length of about 7.5 nm, results in an

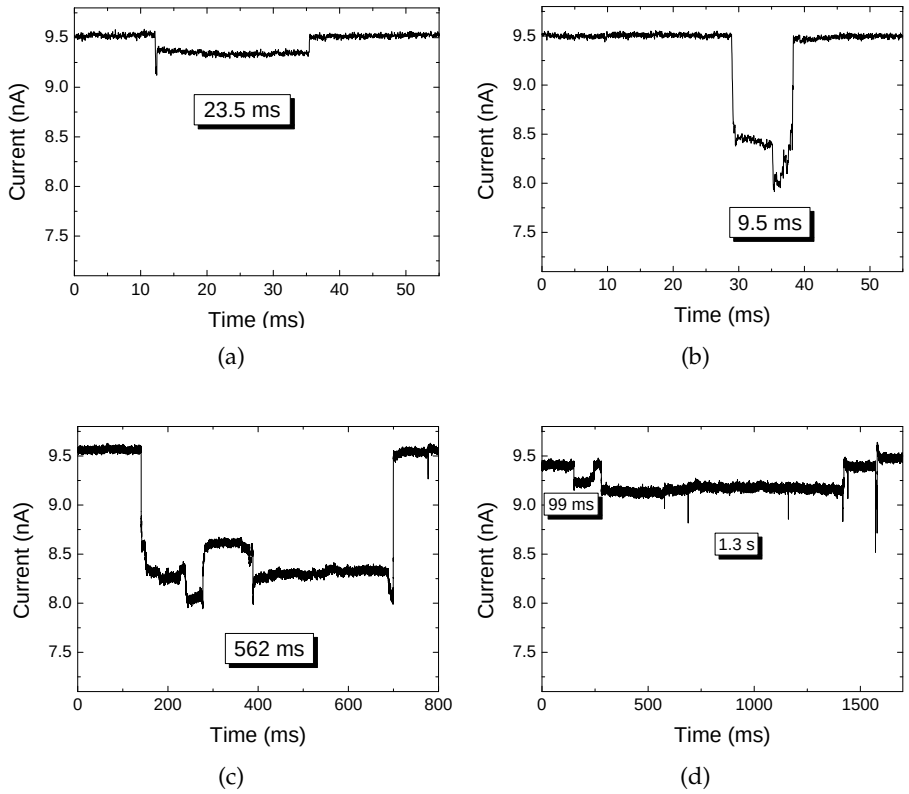

Figure 71. Examples of current blockage events that most likely correspond to DNA molecules passing through the pore in different conformations.

electric field strength of 160 kV/cm. The same field strength is achieved for a track-etched pore (effective length 200 nm (see section 7.2.1 [105])) only for 3.3 V. It is also possible that the specific shape of individual pore tips as well as the charge density present varies from pore to pore thus leading to the different observed threshold voltages. This idea is supported by the fact that pores of nominally similar sizes show sometimes different degrees of rectification in their $I - V$ curves.

Not only the threshold voltage but also the size and shape of the observed events varied between the experiments. In the majority of cases, they were of 'spike-like' shape with durations of 1–2 ms as those shown in the inset of Fig. 72 and those shown in Fig. 75. But a few measurements revealed also different characteristic event shapes, for example those belonging to the measurement presented in Fig. 74, examples of which are shown in Fig. 76. The majority of these had a very characteristic shape shown in parts (a) and (b), starting with a short upward spike, followed by one (or more) downward spikes, a constant region of slightly reduced current and finally a 'bump' of larger current reduction. Sometimes

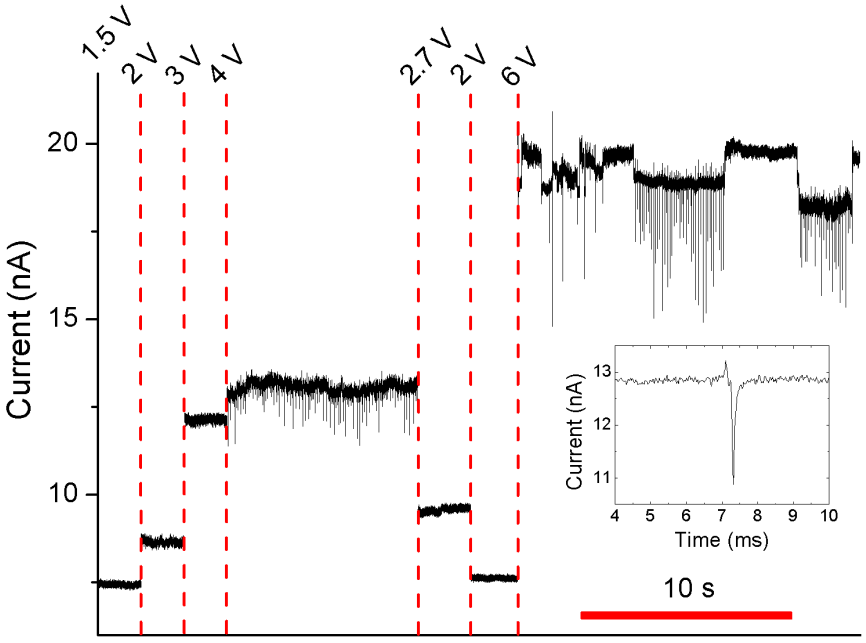

Figure 72. Voltage dependent measurements with pore #1022.2 with $d \sim 6$ nm and λ-DNA added on the small side of the pore to a final concentration of 30 ng/µl ≙ 0.9 nM.

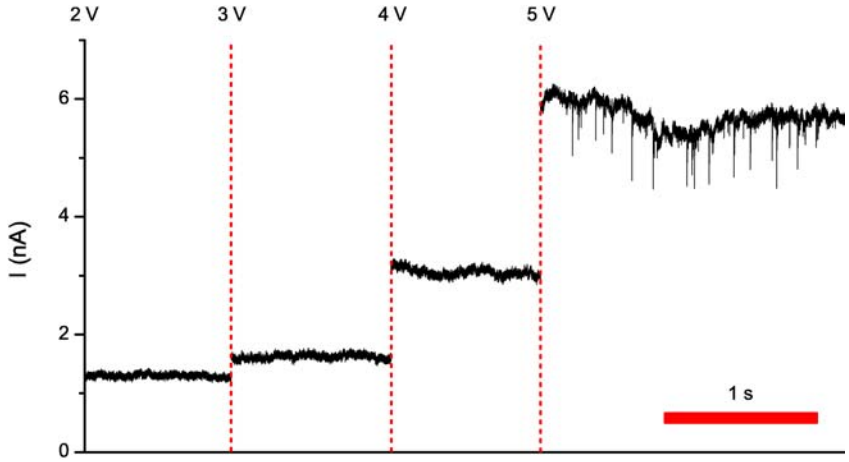

Figure 73. Voltage threshold for pore #299.1 with $d \sim 6$ nm. Final DNA concentrations: 104 bp: 24 ng/µl ≙ 373 nM and 1215 bp: 21 ng/µl ≙ 28 nM. Experiment carried out in Ireland, figure courtesy of K. Healy.

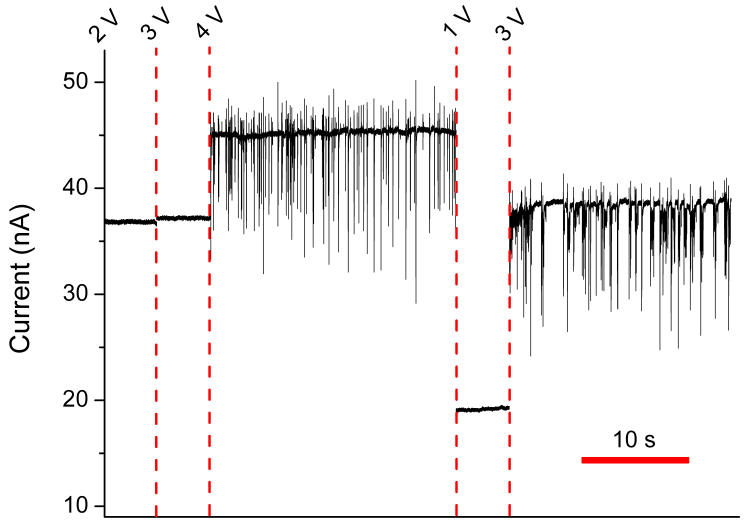

Figure 74. Voltage dependent measurements with pore #1022.4 with $d \sim 20$ nm and λ-DNA added on the small side of the pore to a final concentration of 71 ng/µl ≙ 2.3 nM. For examples of the event shapes, see Fig. 76.

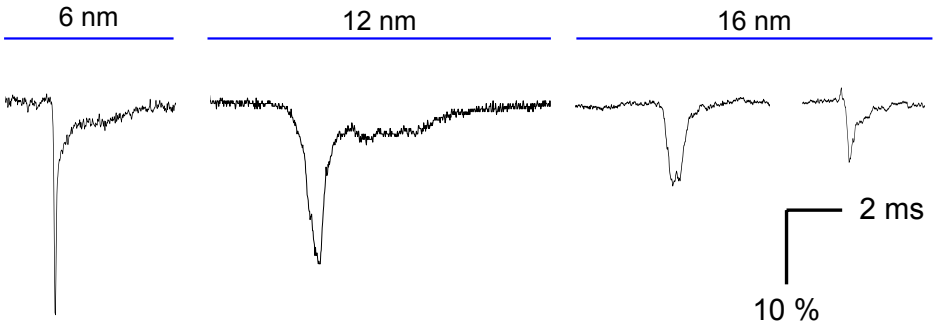

Figure 75. Example events for different pore sizes. The depth has been normalized to facilitate comparison. Figure courtesy of K. Healy.

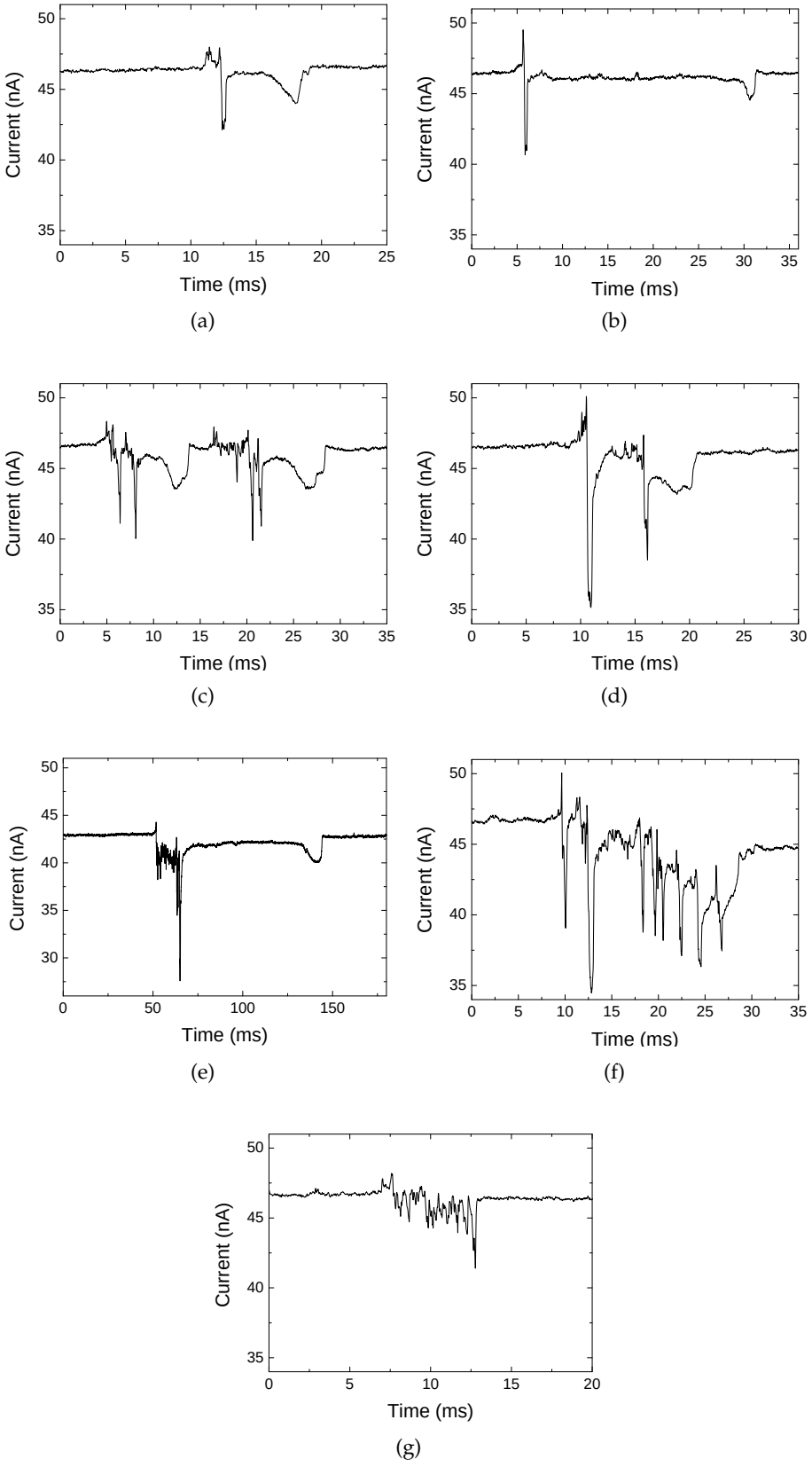

Figure 76. Examples of current blockage events observed with λ-DNA recorded with pore #1022.4, $d \sim 20$ nm. Final DNA concentration was 2.3 nM. The voltage dependence of this measurement is shown in Fig. 74.

LENGTH (BP)	NAME/DESCRIPTION	SOURCE
104	from human gene IGF2	Biochem. Dept., UCC
1215	from yeast *Yarrowia lipolytica*	Biochem. Dept., UCC
48500	λ-DNA	Bioron GmbH, Germ.

Table 1. Linear double stranded DNA of different lengths used in translocation experiments at higher voltage.

they followed very closely one after the other (c) or appeared nested one inside the other (d). Their duration was usually around 20 ms, but a few extended up to 100 ms (e). A much smaller number of events showed more complicated shapes as in (f) and some disturbances of the current as in (g) were also observed. The mean depth of the events was about 20% of the open pore current. Histograms of depth and duration are shown in Fig. 77. If one assumes that these events are caused by

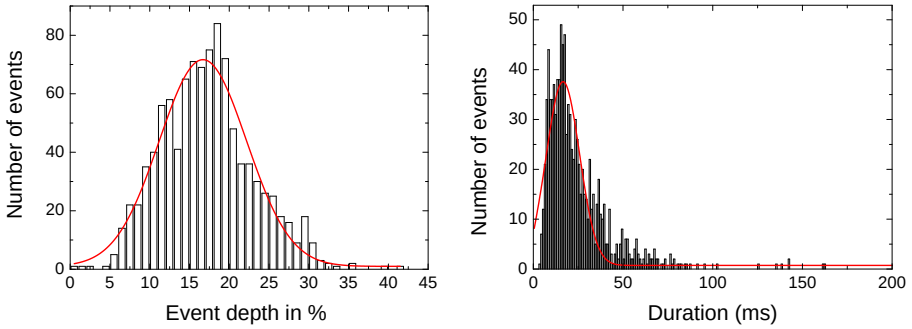

(a) (b)

Figure 77. Histograms of depth (in % of open pore current) and duration of the events recorded with pore #1022.4 and λ-DNA fitted by Gaussians (red curves) (belonging to Figs. 74 and 76).

translocations of the λ-DNA through the pore, their characteristic shape could be attributed to a specific procedure required by the very long DNA to enter the pore (DNA was placed on the side of the narrow pore opening). The spikes at the start of the events could be due to collisions of the coiled molecule with the pore opening, after which it enters the pore, is stretched and moves through (region of constant reduced current) and finally moves around in different conformations in the large part of the pore (giving the 'bump') before exiting.

The question remains, why these events are so different in shape and duration from the 'spike-like' ones observed with the same DNA but a

different pore (Fig. 72) as well as with shorter DNA molecules (Fig. 73). It is unlikely (although not completely ruled out) that the latter result from only collisions with the pore, since these are expected to be still much shorter.

BEHAVIOR AT HIGHER VOLTAGES WITHOUT DNA It has to be mentioned, that recent experiments with polyimide pores at higher voltages with only buffer solution sometimes also revealed voltage dependent current fluctuations, as shown in Figs. 78 and 79. However, the spikes in

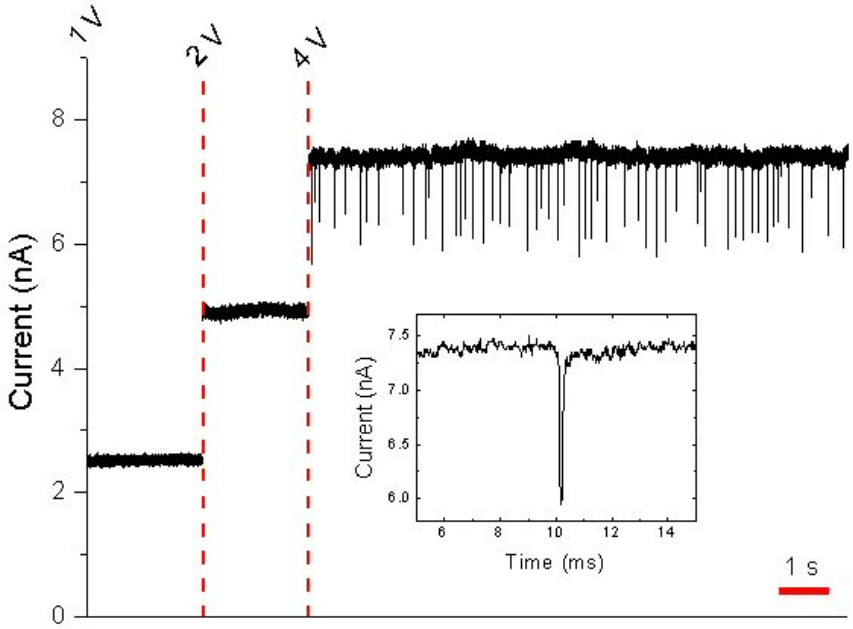

Figure 78. Spike-like fluctuations at higher voltages in pure buffer solution. Pore #90.4, $d \sim 10$ nm.

Fig. 78 are shorter ($\sim$ 200 µs) than those recorded with DNA and those in Fig. 79 are characterized rather by upward spikes than blockages of current. It has also to be noted that these fluctuations do not occur in all pores. A decision whether current blockages recorded in the presence of DNA are actually caused by those DNA molecules, or something else, is complicated by the fact that reference measurements before the addition of DNA were often performed for lower voltages only, because the threshold voltage was expected to be lower. To repeat this measurement afterwards is problematic, since the cell has to be disassembled for cleaning which results in slight variations in the experimental conditions. Also, some DNA fragments may remain after cleaning.

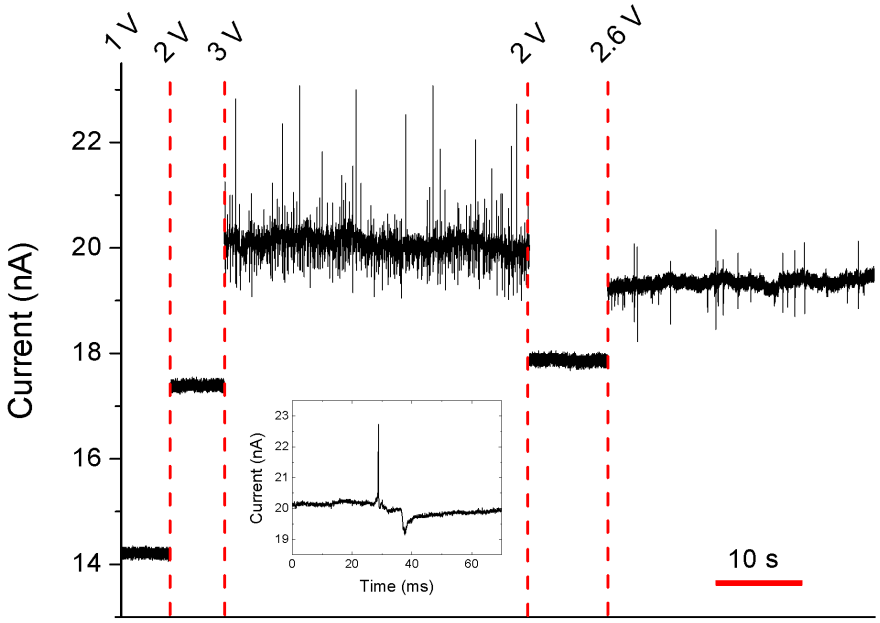

Figure 79. Fluctuations at higher voltages in pure buffer solution. Pore #92.1, $d \sim 38$ nm.

A more systematic examination of the behavior of polyimide pores in pure buffer solution at higher voltages is certainly needed to clarify the origin of voltage dependent fluctuations, and to develop criteria to clearly distinguish them from those caused by DNA translocations.

8 CONCLUSIONS AND OUTLOOK

This work deals with a variety of different topics, concerning the production, characterization and application of track-etched nanopores in various polymer foils. Most of the work focused on conical nanopores, covering their unusual asymmetric current-voltage characteristics and application as biosensors, but also different methods for pore size determination were compared and small-angle X-ray scattering experiments were performed with cylindrical pores in various types of polycarbonates.

8.1 GEOMETRICAL CHARACTERIZATION OF CYLINDRICAL PORES

By comparing the diameter values obtained by SEM on the membrane surface with those extracted from metalic replica grown inside the pores, as well as with values determined by conductometry, it was found that cylindrical pores in PET and polycarbonate prepared by the methods described here, have a constriction near the membrane surface. This result was confirmed by SAXS measurements, where the diameters extracted from the scattering data (being values resulting from the bulk of the membrane) were also larger than those obtained from the corresponding electron micrographs. Whether this is a surface tension effect or caused by a chemically more resistant surface layer [58] or even an inhomogeneous track [52], has yet to be clarified. Experiments with membranes preetched before the irradiation in order to remove a possible surface layer are currently under way. In any case one should keep this effect in mind when determining pore sizes from SEM pictures. It will be especially interesting to find out if this narrowing of the pore close to the surface occurs also for conical pores on the side of the large diameter D, because this is needed to calculate the diameter of the narrow pore opening from conductometric data, and a convenient way to determine D is by SEM.

8.2 SMALL-ANGLE X-RAY SCATTERING

Polycarbonate is used regularly as template for nanowire growth as well as for filtration applications. It is known that track-etched pores in polycarbonate exhibit a very uniform pore size distribution, especially when they are irradiated with UV light before etching. As the currently used polycarbonate material (Makrofol from Bayer) has recently been discontinued and will have to be replaced by other materials in the future, the successor material (Pokalon from LOFO) was investigated here in comparison to Makrofol. The results show that UV irradiation has

a very beneficial effect on the pore size distribution in both materials, with an effect even more pronounced in Pokalon. However, pores in the latter were reported to exhibit cigar-like shapes [52, 53], which would be a disadvantage if for example cylindrical nanowires were required. A possible substitute for Pokalon could also be Aryphan (from LOFO), a polyarylate, which is reported to have very similar properties to polycarbonate [156]. SAXS studies on this material are in preparation. It is also planned to extend the scattering experiments to the conical pores discussed in the other sections of this thesis; the required modifications to the data analysis software PXY7 are currently being performed by G. Pépy.

8.3 IONIC TRANSPORT PROPERTIES OF SINGLE CONICAL PORES IN PET

Conical pores in PET raised early interest due to their ionic current transport properties similar to those of biological ion channels. These include voltage dependent ion current fluctuations with power spectra similar to biochannels [30, 77], ion current rectification [31] and cation selectivity [77]. Understanding the physical processes underlying these properties is of great interest for any applications involving transport of ions or molecules through these pores and also might be useful for the understanding of transport through ion channels on a basic level. Crucial to the occurrence of rectification and selectivity is the fact that track-etched pores in PET (and also in polyimide) have negatively charged pore walls due to the creation of carboxyl groups during the etching process.

8.3.1 *Ion current rectification*

Several theoretical models have been developed to describe the asymmetric $I - V$ curves [32–34, 79–83], which were later also observed in other asymmetric charged nanosystems [21, 73–75]. Due to the negatively charged pore walls, an asymmetric electrostatic potential is present along the pore axis without an external voltage applied. The earliest model [32, 33] explains the rectification, i. e., different currents for different polarities of external voltage by the ratchet-like shape of this potential, which leads to formation of a cation trap for one polarity. Here the validity of another theoretical approach, namely the calculation of $I - V$ curves based on the Poisson-Nernst-Planck (PNP) equations (developed by P. Ramírez and J. Cervera) [34] was tested by comparison of calculations with systematic experimental measurements of the concentration dependence of the observed rectification. A good qualitative agreement was found [80], however calculations have been performed only up to 1 V, while measurements ranged up to 2 V. The applicability of the model to

this higher voltage range has still to be evaluated. It would also be an interesting task to apply the model to pores with different geometries (e. g., different opening angle, cylindrical pores tapered at one end).

8.3.2 *Selectivity*

Another interesting property of conical charged pores is the fact, that their cation selectivity depends on the direction of an applied concentration gradient. The selectivity can be extracted from measurements of the reversal potential in asymmetric electrolyte conditions, which were performed systematically for up to ten-fold concentration gradients. It was found that the selectivity is higher, when the lower concentration is applied on the small side of the pore. This is due to the fact that the fixed charges at the pore tip (the crucial region for the determination of transport properties) are then less screened and thus have a stronger effect. This behavior was reproduced by PNP calculations. The model predicts furthermore a voltage dependence of the selectivity (higher selectivity for negative voltages applied on the small side of the pore). An experimental confirmation of this effect would give additional information about the validity of this model. For these measurements one could use radioactive or fluorescent labeled charged particles of different polarities and observe their transport through the pores depending on the externally applied voltage.

8.4 EFFECT OF DIVALENT CATIONS ON ION TRANSPORT OF SINGLE CONICAL PORES IN POLYIMIDE

Recently, another 'biomimetic' effect of conical track-etched pores was discovered with PET: The presence of micromolar concentrations of divalent cations (e. g., Ca^{2+}) influences the pores' transport properties dramatically, leading to blockages and oscillation-like fluctuations [108, 110]. Since it is known that transport properties of track-etched pores are influenced by the polymer they are produced in (pores in PET exhibit current fluctuations while pores in polyimide show a stable current signal), it was an interesting task to perform complementary experiments to study this effect with polyimide pores. It was found that they indeed show a similar behavior to that observed with PET pores. Theories to explain this effect are currently developed. In both polymers, carboxyl groups (COO^-) are created at the pore walls during the etching process. Several divalent metal ions are known to temporarily bind to these groups. They thus change the electrostatic potential inside the pores and thereby also the ionic transport characteristics [110]. Due to these negative charges at the pore walls, the concentration of divalent cations inside the pore can be increased voltage-dependently in comparison with the

bulk solution. This allows the precipitation of calcium phosphates[1] inside the pore, where the precipitates block the pore, while their dissolution again increases the current. It is not yet clear if and how the two effects (binding to carboxyls and precipitation) are related, leading finally to the observed fluctuations. The binding constants of the divalent cations to the COO^- groups as well as the calcium concentrations inside the pore are voltage dependent, a fact that is reflected by the observation that the characteristics of the current fluctuations are also voltage dependent. Usually no fluctuations are observed below a certain voltage (the pore is mainly in closed state), they then become more and more ordered with increasing voltage and finally show a 'chaotic' behavior at high voltages. It was already shown that different divalent cations lead to different time scale characteristics of the observed fluctuations, possibly related to their binding constants to carboxyl groups. First experiments with polyimide pores show the same effect. A more systematic study with a range of different ions will help to further clarify the underlying physics of this phenomenon. Since the fluctuating nanopore is a system far from equilibrium, it is expected to be very sensitive (i. e., change its characteristics) to small changes in the external conditions, such as the presence of other ions or biomolecules. The system seems therefore to be ideal to work as a new type of very sensitive detector. Preliminary measurements performed by Siwy et al. [117] indicated that the system indeed responds to micromolar additions of, for example, antibiotics.

8.5 APPLICATION: DETECTION OF SINGLE DNA MOLECULES

Due to their stable ion current signal, pores in polyimide are promising candidates for applications requiring the detection of small current changes, such as the detection of single molecules passing through the pore by a change in pore conductance. It was shown that these pores are indeed suitable for the detection of DNA molecules of different length, however the success rate of these experiments was rather low (20–30%), indicating a problem inherent in the system. One reason for this could be electrostatic interactions of the negatively charged DNA molecules with the also negatively charged pore walls, hindering the molecules from entering the pore. Testing of this hypothesis could be carried out by performing translocation experiments with pores having different surface charges. It is possible by a variety of methods to chemically modify the carboxyl groups on the pore walls, however, many of these methods involve the use of organic solvents which can affect the polymer and therefore the geometry of the pores. This can be a problem especially for very small pores, so it is advisable to stay with water soluble chemicals. Recently, the conversion of carboxyl groups to amino groups was achieved by the use of the activation agent N-(3-dimethylaminopropyl)-

1 All solutions contained 2 mM phosphate buffer.

N-ethylcarbodiimide hydrochloride (EDC), in polyimide [76] as well as in PET [157]. Single-molecule detection experiments with thus modifed pores are planned for the near future.

Another possible reason for the low reproducibility of the DNA detection experiments could be variations in the actual shape of the small pore opening—it could be possible for example that in some cases this opening is not one single hole but rather a mesh of much smaller pores, yielding together the effective diameter calculated from the conductivity measurements, but preventing DNA from entering. It would be helpful to image the small opening of the pore either by high resolution SEM, TEM or AFM, to learn more about the actual shape of very small pores. The difficulty here is to locate a very small single pore for imaging. To do this, one could either use a mask with an aperture of only a few micrometers for irradiation, which stays fixed on the sample during etching, or create a mark on a foil and shoot a single ion onto this mark, which is possible with a precision of approx. 0.5 µm using the microprobe available at GSI [158]. Another possibility would be to investigate a sample containing many conical pores—in this case one can not make a direct comparison with the diameter obtained by conductance measurements, but obtain information about the shapes of very small pores. In such a sample a variety of different pore sizes are present due to slight variations in breakthrough time for the individual tracks.

8.6 OUTLOOK

Besides the future activities mentioned above, it is planned to explore in more detail the possibilities to chemically modify or functionalize the inner walls of track-etched pores in different polymers. It should be possible to attach molecules on the surface which bind specifically to other molecules one wants to detect, resulting in a blockage of the pore in the presence of the analyte. This was already achieved with gold plated pores using thiol chemistry[2] [159] but eliminating this gold plating step would be a further progress towards practical nanopore-based sensors. The possibility to directly change the surface properties by simple chemical reactions can be seen as a major advantage of polymer pores compared to other types of synthetic nanopores.

2 Thiol (SH) groups form strong chemical bonds with gold.

BIBLIOGRAPHY

[1] B. Hille, *Ionic Channels of Excitable Membranes*, 2nd ed. Sinauer Associates Inc., 1992. (Cited on pages 1, 15, 31, 37, 51, 53, and 63.)

[2] D. Doyle, J. Cabral, R. Pfuetzner, A. Kuo, J. Gulbis, S. Cohen, B. Chait, and R. MacKinnon, "The structure of the potassium channel: Molecular basis of K^+ conduction and selectivity," *Science*, vol. 280, p. 69, 1998. (Cited on pages 1 and 51.)

[3] Y. Jiang, A. Lee, J. Chen, M. Cadene, B. Chait, and R. MacKinnon, "Crystal structure and mechanism of a calcium-gated potassium channel," *Nature*, vol. 417, p. 515, 2002. (Cited on page 1.)

[4] Y. Jiang, V. Ruta, J. Chen, A. Lee, and R. MacKinnon, "The principle of gating charge movement in a voltage-dependent K^+ channel," *Nature*, no. 423, p. 42, 2003. (Cited on page 1.)

[5] J. Morais-Cabral, Y. Zhou, and R. MacKinnon, "Energetic optimization of ion conduction rate by the K^+ selectivity filter," *Nature*, vol. 414, p. 37, 2001. (Cited on page 1.)

[6] M. Sansom, I. Shrivastava, J. Bright, J. Tate, C. Capener, and P. Biggin, "Potassium channels: structures, models, simulations," *Biochim. Biophys. Acta*, vol. 1565, p. 294, 2002. (Cited on page 1.)

[7] G. Yellen, "The voltage-gated potassium channels and their relatives," *Nature*, vol. 419, p. 35, 2002. (Cited on page 1.)

[8] S. Berneche and B. Roux, "Energetics of ion conduction through the K^+ channel," *Nature*, vol. 414, p. 73, 2001. (Cited on page 1.)

[9] D. Deamer and M. Akeson, "Nanopores and nucleic acids: prospects for ultrarapid sequencing," *Trends Biotechnol.*, vol. 18, no. 4, p. 147, Apr. 2000. (Cited on pages 1 and 80.)

[10] J. Kasianowicz, E. Brandin, D. Branton, and D. Deamer, "Characterization of individual polynucleotide molecules using a membrane channel," *Proc. Natl. Acad. Sci. USA*, vol. 93, p. 13770, 1996. (Cited on pages 1 and 79.)

[11] M. Akeson, D. Branton, J. Kasianowicz, E. Brandin, and D. Deamer, "Microsecond Time-Scale Discrimination Among Polycytidylic Acid, Polyadenylic Acid, and Polyuridilic Acid as Homopolymers or as Segments Within Single RNA Molecules," *Biophys. J.*, vol. 77, p. 3227, 1999. (Cited on pages 1 and 80.)

[12] A. Meller, L. Nivon, E. Brandin, J. Golovchenko, and D. Branton, "Rapid nanopore discrimination between single polynucleotide molecules," *Proc. Natl. Acad. Sci. USA*, vol. 97, p. 1079, 2000. (Cited on pages 1, 80, and 85.)

[13] S. Henrickson, M. Misakian, B. Robertson, and J. Kasianowicz, "Driven DNA transport into an asymmetric nanometer-scale pore," *Phys. Rev. Lett.*, vol. 85, p. 3057, 2000. (Cited on pages 1 and 87.)

[14] W. Vercoutere, S. Winters-Hilt, H. Olsen, D. Deamer, D. Haussler, and M. Akeson, "Rapid discrimination among individual DNA hairpin molecules at single-nucleotide resolution using an ion channel," *Nat. Biotech.*, vol. 19, p. 248, 2001. (Cited on pages 1 and 80.)

[15] A. Meller, L. Nivon, and D. Branton, "Voltage-driven DNA translocations through a nanopore," *Phys. Rev. Lett.*, vol. 86, no. 15, p. 3435, Apr. 2001. (Cited on page 1.)

[16] S. Howorka, S. Cheley, and H. Bayley, "Sequence-specific detection of individual DNA strands using engineered nanopores," *Nat. Biotech.*, vol. 19, no. 7, p. 636, July 2001. (Cited on page 1.)

[17] A. Meller and D. Branton, "Single molecule measurements of DNA transport through a nanopore," *Electrophoresis*, vol. 23, no. 16, p. 2583, Aug. 2002. (Cited on page 1.)

[18] D. Branton and A. Meller, "Using nanopores to discriminate between single molecules of DNA," in *Structure and Dynamics of Confined Polymers*, J. Kasianowicz, Ed. Kluwer Acad. Pub., 2002, p. 177. (Cited on page 1.)

[19] J. Li, D. Stein, C. McMullan, D. Branton, M. Aziz, and J. Golovchenko, "Ion-beam sculpting at nanometre length scales," *Nature*, vol. 412, p. 166, 2001. (Cited on pages 1 and 81.)

[20] D. M. Stein, C. J. McMullan, J. Li, and J. A. Golovchenko, "Feedback-controlled ion beam sculpting apparatus," *Rev. Sci. Inst.*, vol. 75, no. 4, p. 900, Apr. 2004. (Cited on page 1.)

[21] P. Chen, T. Mitsui, D. Farmer, J. Golovchenko, R. Gordon, and D. Branton, "Atomic layer deposition to fine-tune the surface properties and diameters of fabricated nanopores," *Nano Lett.*, vol. 4, p. 1333, 2004. (Cited on pages 1, 31, and 96.)

[22] A. Storm, J. Chen, X. Ling, H. Zandbergen, and C. Dekker, "Fabrication of solid-state nanopores with single-nanometre precision," *Nat. Mat.*, vol. 2, p. 537, 2003. (Cited on pages 1 and 81.)

[23] J. Heng, V. Dimitrov, Y. Grinkova, C. Ho, T. Kim, D. Muller, S. Sligar, T. Sorsch, R. Twesten, R. Timp, and G. Timp, "The detection of DNA using a silicon nanopore," in *IEDM'03 Technical Digest*. Washington, DC, USA: IEEE International, 2003, p. 32.2.1. (Cited on page 1.)

[24] A. Mara, Z. Siwy, C. Trautmann, J. Wan, and F. Kamme, "An asymmetric polymer nanopore for single molecule detection," *Nano Lett.*, vol. 4, p. 497, 2004. (Cited on pages 1, 82, 83, and 85.)

[25] A. Biance, J. Gierak, E. Bourhis, A. Madouri, X. Lafosse, G. Patriarche, G. Oukhaled, C. Ulysse, J. Galas, Y. Chen, and L. Auvray, "Focused ion beam sculpted membranes for nanoscience tooling," *Microelec. Eng.*, vol. 83, p. 1474, 2006. (Cited on pages 1 and 81.)

[26] H. Chang, F. Kosari, G. Andreadakis, M. Alam, G. Vasmatzis, and R. Bashir, "DNA-mediated fluctuations in ionic current through silicon oxide nanopore channels," *Nano Lett.*, vol. 4, p. 1551, 2004. (Cited on pages 1, 81, 82, and 83.)

[27] Z. Siwy, E. Heins, C. Harrell, P. Kohli, and C. Martin, "Conical-nanotube ion-current rectifiers: the role of surface charge." *J. Am. Chem. Soc.*, vol. 126, p. 10850, 2004. (Cited on pages 1, 31, and 51.)

[28] Z. Siwy, I. Kosińska, A. Fuliński, and C. Martin, "Asymmetric Diffusion through Synthetic Nanopores," *Phys. Rev. Lett.*, vol. 94, p. 048102, 2005. (Cited on pages 1, 51, 53, and 56.)

[29] Y. E. Korchev, C. L. Bashford, G. M. Alder, P. Y. Apel, D. T. Edmonds, A. A. Lev, K. Nandi, A. V. Zima, and C. A. Pasternak, "A novel explanation for fluctuations of ion current through narrow pores," vol. 11, no. 7, pp. 600–608, June 1997. (Cited on page 1.)

[30] Z. Siwy and A. Fuliński, "Origins of $1/f^{\alpha}$ noise in membrane channel currents," *Phys. Rev. Lett.*, vol. 89, p. 158101, 2002. (Cited on pages 1 and 96.)

[31] P. Apel, Y. Korchev, Z. Siwy, R. Spohr, and M. Yoshida, "Diode-like single-ion track membrane prepared by electro-stopping," *Nucl. Instrum. Methods Phys. Res., Sect. B*, vol. 184, p. 337, 2001. (Cited on pages 1, 9, 31, and 96.)

[32] Z. Siwy, "Ion-current rectification in nanopores and nanotubes with broken symmetry," *Adv. Funct. Mater.*, vol. 16, p. 735, 2006. (Cited on pages 1, 32, 33, 60, and 96.)

[33] Z. Siwy and A. Fuliński, "A nanodevice for rectification and pumping ions," *Am. J. Phys.*, vol. 72, p. 567, 2004. (Cited on pages 1, 32, 53, and 96.)

[34] J. Cervera, B. Schiedt, and P. Ramírez, "A Poisson/Nernst-Planck model for ionic transport through synthetic conical nanopores," *Europhys. Lett.*, vol. 71, p. 35, 2005. (Cited on pages 2, 32, 39, 43, and 96.)

[35] Z. Lu, "Mechanism of Rectification in Inward-Rectifier K^+ Channels," *Annu. Rev. Physiol.*, vol. 66, p. 103, 2004. (Cited on pages 2 and 65.)

[36] J. Johnson and P. Ascher, "Voltage-dependent block by intracellular Mg^{2+} of N-methyl-D-aspartate-activated channels," *Biophys. J.*, vol. 57, p. 1085, 1990. (Cited on pages 2 and 65.)

[37] R. Fleischer, P. Price, and R. Walker, *Nuclear Tracks in Solids*. University of California Press, 1975. (Cited on pages 3 and 5.)

[38] P. Sigmund, *Stopping of Heavy Ions (A Theoretical Approach)*. Springer, 2004. (Cited on page 3.)

[39] J. Ziegler, "SRIM 2003," SRIM.com, 2003. (Cited on page 3.)

[40] J. Jackson, *Klassische Elektrodynamik*. Walter de Gryuter Verlag, 1983. (Cited on page 4.)

[41] C. Trautmann, S. Bouffard, and R. Spohr, "Etching threshold for ion tracks in polyimide," *Nucl. Instrum. Methods Phys. Res., Sect. B*, vol. 116, p. 429, 1996. (Cited on page 5.)

[42] Y. Sun, Z. Zhu, Z. Wang, Y. Jin, J. Liu, M. Hou, and Q. Zhang, "Swift heavy ion induced amorphisation and chemical modification in polycarbonate," *Nucl. Instrum. Methods Phys. Res., Sect. B*, vol. 209, p. 188, 2003. (Cited on page 5.)

[43] F. Dehaye, E. Balanzat, E. Ferain, and R. Legras, "Chemical modifications induced in bisphenol A polycarbonate by swift heavy ions," *Nucl. Instrum. Methods Phys. Res., Sect. B*, vol. 209, p. 103, 2003. (Cited on page 5.)

[44] D. Albrecht, P. Armbruster, R. Spohr, M. Roth, K. Schaupert, and H. Stuhrmann, "Small angle scattering from oriented latent nuclear tracks," *Nucl. Instrum. Methods Phys. Res., Sect. B*, vol. 2, p. 702, 1984. (Cited on page 5.)

[45] V. Picq, J. Ramillon, and E. Balanzat, "Swift heavy ions on polymers: Hydrocarbon gas release," *Nucl. Instr. Methods Phys. Res. B*, vol. 146, p. 496, 1998. (Cited on page 5.)

[46] Z. Siwy, P. Apel, D. Dobrev, R. Neumann, R. Spohr, C.Trautmann, and K.O.Voss, "Ion transport through asymmetric nanopores prepared by ion track etching," *Nucl. Instr. Methods Phys. Res. B*, vol. 208, p. 143, 2003. (Cited on page 8.)

[47] Z. Siwy, D. Dobrev, R. Neumann, C. Trautmann, and K. Voss, "Electro-responsive asymmetric nanopores in polyimide with stable ion-current signal," *Appl. Phys. A*, vol. 76, p. 781, 2003. (Cited on pages 9, 11, and 83.)

[48] T. Cornelius, "Fabrication and characterization of bismuth nanowires," Ph.D. dissertation, Universität Heidelberg, 2006. (Cited on pages 10 and 17.)

[49] N. Chtanko, M. Toimil Molares, T. Cornelius, D. Dobrev, and R. Neumann, "Etched Single Ion-Track Templates for Single Nanowire Synthesis," *J. Phys. Chem. B*, vol. 108, p. 9950, 2004. (Cited on page 10.)

[50] C. Harrell, Z. Siwy, and C. Martin, "Conical nanopore membranes: Controlling the nanopore shape," *Small*, vol. 2, p. 194, 2006. (Cited on pages 10 and 48.)

[51] C. Harrell, Y. Choi, L. Horne, L. Baker, Z. Siwy, and C. Martin, "Resitive-Pulse DNA Detection with a Conical Nanopore Sensor," *Langmuir*, vol. 22, p. 10837, 2006. (Cited on page 10.)

[52] C. Schönenberger, B. van der Zande, L. Fokkink, M. Henny, C. Schmid, M. Krüger, A. Bachtold, R. Huber, H. Birk, and U. Staufer, "Template Synthesis of Nanowires in Porous Polycarbonate Membranes: Electrochemistry and Morphology," *J. Phys. Chem. B*, vol. 101, p. 5497, 1997. (Cited on pages 10, 17, 95, and 96.)

[53] N. Chtanko, private communication. (Cited on pages 10 and 96.)

[54] Z. Siwy, P. Apel, D. Baur, D. Dobrev, Y. Korchev, R. Neumann, R. Spohr, C. Trautmann, and K. Voss, "Preparation of synthetic nanopores with transport properties analogous to biological channels," *Surface Science*, vol. 532, p. 1061, 2003. (Cited on pages 11 and 34.)

[55] C. Trautmann, W. Brüchle, R. Spohr, J. Vetter, and N. Angert, "Pore geometry of etched ion tracks in polyimide," *Nucl. Instrum. Methods Phys. Res., Sect. B*, vol. 111, p. 70, 1996. (Cited on page 11.)

[56] J. Romano and R. Price, "The conical resistor conundrum. A potential solution," *Am. J. Phys.*, vol. 64, p. 1150, 1996. (Cited on page 14.)

[57] J. Hall, "Access resistance of a small circular pore," *J. Gen. Physiol.*, vol. 66, p. 531, 1975. (Cited on page 15.)

[58] M. Lindeberg and K. Hjort, "A comprehensive study of ion track enabled high aspect ratio microstructures in flexible circuit boards," *Microsys. Tech.*, vol. 9, p. 608, 2004. (Cited on pages 17 and 95.)

[59] O. Kratky, "Diffuse Röntgenkleinwinkelstreuung," *Angew. Chem.*, vol. 72, p. 467, 1960. (Cited on pages 19 and 22.)

[60] A. Guinier and G. Fournet, *Small-Angle Scattering of X-Rays*. Wiley, 1955. (Cited on pages 20 and 22.)

[61] D. Albrecht, "Untersuchung der von schweren Ionen in Dielektrika erzeugten Defektstrukturen mittels Kleinwinkelstreuung," Ph.D. dissertation, Universität Gießen, 1983. (Cited on pages 21 and 22.)

[62] M. Born and E. Wolf, *Principles of Optics*, 7th ed. University Press, Cambridge, 2005. (Cited on page 21.)

[63] M. Toimil Molares, J. Brötz, V. Buschmann, D. Dobrev, R. Neumann, R. Scholz, I. Schuchert, C. Trautmann, and J. Vetter, "Etched heavy ion tracks in polycarbonate as template for copper nanowires," *Nucl. Instrum. Methods Phys. Res., Sect. B*, vol. 185, p. 192, 2001. (Cited on page 21.)

[64] G. Pépy, "Pxy7." (Cited on page 22.)

[65] D. Albrecht, P. Armbruster, M. Roth, and R. Spohr, "Solid state nuclear track detectors," *Rad. Efffects*, vol. 65, p. 145, 1982. (Cited on page 22.)

[66] W. DeSorbo, "Ultraviolet effects and aging effects on etching characteristics of fission tracks in polycarbonate film," *Nucl. Tracks*, vol. 3, p. 13, 1979. (Cited on page 23.)

[67] E. Ferain and R. Legras, "Track-etch templates designed for micro- and nanofabrication," *Nucl. Instrum. Methods Phys. Res., Sect. B*, vol. 208, p. 115, 2003. (Cited on page 23.)

[68] Z. Zhu, Y. Maekawa, Q. Liu, and M. Yoshida, "Influence of UV light illumination on latent track structure in PET," *Nucl. Instrum. Methods Phys. Res., Sect. B*, vol. 236, p. 61, 2005. (Cited on page 23.)

[69] G. Pépy and A. Kuklin, "An orientation process to study nuclear membranes by small angle neutron scattering," *Nucl. Instr. Methods Phys. Res. B*, vol. 185, p. 198, 2001. (Cited on page 24.)

[70] G. Pépy, P. Boesecke, A. Kuklin, E. Manceau, B. Schiedt, Z. Siwy, M. Toulemonde, and C. Trautmann, "Cylindrical nanochannels in ion-track polycarbonate membranes studied by small-angle x-ray scattering," *J. Appl. Cryst.*, 2007, accepted for publication. (Cited on page 28.)

[71] F. Reimann and F. Ashcroft, "Inwardly rectifying potassium channels," *Curr. Op. Cell Biol.*, vol. 11, p. 503, 1999. (Cited on page 31.)

[72] C. Doupnik, N. Davidson, and H. Lester, "The inward rectifier potassium channel family," *Curr. Op. Neurobiol.*, vol. 5, p. 268, 1995. (Cited on page 31.)

[73] C. Wei, A. Bard, and S. Feldberg, "Current Rectification at Quartz Nanopipet Electrodes," *Anal. Chem.*, vol. 69, p. 4627, 1997. (Cited on pages 31 and 96.)

[74] S. Umehara, N. Pourmand, C. Webb, R. Davis, K. Yasuda, and M. Karhanek, "Current Rectification with Poly-L-Lysin-Coated Quartz Nanopipettes," *Nano Lett.*, vol. 6, p. 2486, 2006. (Cited on pages 31 and 96.)

[75] Z. Wei, M. Kondratenko, L. Dao, and D. Perepichka, "Rectifying Diodes from Asymmetrically Functionalized Single-Wall Carbon Nanotubes," *J. Am. Chem. Soc.*, vol. 128, p. 3134, 2006. (Cited on pages 31 and 96.)

[76] M. Ali, W. Ensinger, R. Neumann, and B. Schiedt, "Chemical modification of track-etched single conical nanopores inducing inversed inner wall polarity," *GSI Scientific Report*, 2006. (Cited on pages 31 and 99.)

[77] Z. Siwy, Y. Gu, H. Spohr, D. Baur, A. Wolf-Reber, R. Spohr, P. Apel, and Y. Korchev, "Rectification and voltage gating of ion currents in a nanofabricated pore," *Europhys. Lett.*, vol. 60, p. 349, 2002. (Cited on pages 32, 44, 48, 53, and 96.)

[78] A. Fuliński, I. Kosińska, and Z. Siwy, "On the validity of continuous modelling of ion transport through nanochannels," *Europhys. Lett.*, vol. 67, p. 683, 2004. (Cited on pages 32, 33, 37, and 63.)

[79] I. Kosińska, "How the asymmetry of internal potential influences the shape of $I - V$ characteristic of nanochannels." *J. Chem. Phys.*, vol. 124, p. 244707, 2006. (Cited on pages 32 and 96.)

[80] J. Cervera, B. Schiedt, R. Neumann, S. Mafé, and P. Ramírez, "Ionic conduction, rectification, and selectivity in single conical nanopores." *J. Chem. Phys.*, vol. 124, p. 104706, 2006. (Cited on pages 32, 39, 43, and 96.)

[81] D. Woermann, "Analysis of non-ohmic electrical current-voltage characteristic of membranes carrying a single track-etched conical pore," *Nucl. Instrum. Methods Phys. Res., Sect. B*, vol. 194, p. 458, 2002. (Cited on pages 32 and 96.)

[82] ——, "Electrochemical transport properties of a cone-shaped nanopore: high and low electrical conductivity states depending on the sign of an applied electric potential difference," *Phys. Chem. Chem. Phys.*, vol. 5, p. 1853, 2003. (Cited on pages 32 and 96.)

[83] ——, "Electrochemical transport properties of a cone-shaped nanopore: revisited," *Phys. Chem. Chem. Phys.*, vol. 6, p. 3130, 2004. (Cited on pages 32 and 96.)

[84] A. Fuliński, I. Kosińska, and Z. Siwy, "Transport properties of nanopores in electrolyte solutions: the diffusional model and surface currents," *New J. Phys.*, vol. 7, p. 132, 2005. (Cited on page 33.)

[85] B. Schiedt, K. Healy, A. Morrison, R. Neumann, and Z. Siwy, "Transport of ions and biomolecules through single asymmetric nanopores in polymer films," *Nucl. Instr. Methods Phys. Res. B*, vol. 236, p. 109, 2005. (Cited on page 33.)

[86] Z. Siwy and A. Fuliński, "Fabrication of a Synthetic Nanopore Ion Pump," *Phys. Rev. Lett.*, vol. 89, p. 198103, 2002. (Cited on page 34.)

[87] R. Weast, *Handbook of Chemistry and Physics*. CRC Press, 1973-1974. (Cited on page 37.)

[88] P. Ramírez, M. Aguilella-Arzo, A. Alcaraz, J. Cervera, and V. Aguilella, "Theoretical Description of the Ion Transport Across Nanopores With Titratable Fixed Charges," *Cell Biochem. Biophys.*, vol. 44, p. 287, 2006. (Cited on page 40.)

[89] T. Rostovtseva, C. Bashfors, G. Alder, G. Hill, C. McGiffert, P. Apel, G. Lowe, and C. Pasternak, "Diffusion through Narrow Pores: Movement of Ions, Water and Nonelectrolytes through track-etched PETP Mebranes," *J. Membrane Biol.*, vol. 151, p. 29, 1996. (Cited on page 40.)

[90] R. Robinson and R. Stokes, *Electrolyte Solutions*. Butterworth, London, 1955. (Cited on pages 41 and 55.)

[91] F. Donnan, "The theory of membrane equilibria," *Chem. Rev.*, vol. 1, p. 73, 1924. (Cited on page 41.)

[92] K. Meyer and J.-F. Sievers, "La perméabilité des membranes I. Théorie de la perméabilité ionique," *Helv. Chim. Acta*, vol. 19, p. 649, 1936. (Cited on pages 41 and 57.)

[93] G. Schmid, "Electrochemistry of capillary systems with narrow pores. I. Overview," *J. Membr. Sci.*, vol. 150, p. 151, 1998. (Cited on page 41.)

[94] D. Gillespie and R. Eisenberg, "Modified Donnan potentials for ion transport through biological channels," *Phys. Rev. E*, vol. 63, p. 061902, 2001. (Cited on page 41.)

[95] A. Mauro, "Space charge regions in fixed charge membranes and the associated property of capacitance," *Biophys. J.*, vol. 2, p. 179, 1962. (Cited on page 42.)

[96] C. L. Bashford, G. M. Alder, and C. A. Pasternak, "Fluctuation of surface charge in membrane pores," *Biophys. J.*, vol. 82, p. 2032, 2002. (Cited on page 44.)

[97] E. Gouaux and R. MacKinnon, "Principles of Selective Ion Transport in Channels and Pumps," *Science*, vol. 310, p. 1461, 2005. (Cited on page 51.)

[98] A. Lev, Y. Korchev, T. Rostovtseva, C. Bashford, D. Edmonds, and C. Pasternak, "Rapid switching of ion current in narrow pores: implications for biological ion channels." *Proc. R. Soc. Lond. B*, vol. 252, p. 187, 1993. (Cited on pages 51 and 63.)

[99] C. Martin, M. Nishizawa, K. Jirage, M. Kang, and S. Lee, "Controlling Ion-Transport Selectivity in Gold Nanotubule Membranes," *Adv. Mater.*, vol. 13, p. 1351, 2001. (Cited on page 51.)

[100] P. Ramírez, S. Mafé, V. Aguilella, and A. Alcaraz, "Synthetic anopores with fixed charges: an electrodiffusion model for ionic transport," *Phys. Rev. E*, vol. 68, p. 011910, 2003. (Cited on pages 51 and 63.)

[101] P. Ramírez, S. Mafé, V. Alcaraz, and J. Cervera, "Modeling of pH-switchable ion transport ans selectivity in nanopore membranes with fixed charges," *J. Phys. Chem. B*, vol. 107, p. 13178, 2003. (Cited on page 51.)

[102] N. Lakshminarayanaiah, "Measurements of Membrane Potential and Estimation of Effective Fixed-Charge Density in Membranes," *J. Membrane Biol.*, vol. 21, p. 175, 1975. (Cited on page 53.)

[103] G. Adam, P. Läuger, and G. Stark, *Physikalische Chemie und Biophysik*. Springer, 2003. (Cited on pages 55, 58, and 65.)

[104] S. Lee, Y. Zhang, H. White, C. Harrell, and C. Martin, "Electrophoretic Capture and Detection of Nanoparticles at the Opening of a Membrane Pore Using Scanning Electrochemical Microscopy," *Anal. Chem.*, vol. 76, p. 6108, 2004. (Cited on page 56.)

[105] E. Heins, Z. Siwy, L. Baker, and C. Martin, "Detecting single porphyrin molecules in a conically shaped synthetic nanopore," *Nano Lett.*, vol. 5, p. 1824, 2005. (Cited on pages 56, 84, and 88.)

[106] K. Mubagwa, M. Stengl, and W. Flameng, "Extracellular divalent cations block a cation non-selective conductance unrelated to calcium channels in rat cardiac muscle," *J. Physiol.*, vol. 502, p. 235, 1997. (Cited on page 63.)

[107] C. Pasternak, C. Bashford, Y. Korchev, T. Rostovtseva, and A. Lev, "Modulation of surface flow by divalent cations and protons," *Coll. Surf. A*, vol. 77, p. 119, 1993. (Cited on page 63.)

[108] Z. Siwy, M. Powell, E. Kalman, R. Astumian, and R. Eisenberg, "Negative Incremental Resistance Induced by Calcium in Asymmetric Nanopores," *Nano Lett.*, vol. 6, p. 473, 2006. (Cited on pages 63, 64, 75, and 97.)

[109] R. Mackay, "Negative Resistance," *Am. J. Phys.*, vol. 26, p. 60, 1958. (Cited on page 63.)

[110] Z. Siwy, M. Powell, A. Petrov, E. Kalman, C. Traumann, and R. Eisenberg, "Calcium-Induced Voltage Gating in Single Conical Nanopores," *Nano Lett.*, vol. 6, p. 1729, 2006. (Cited on pages 64, 65, 66, and 97.)

[111] M. Berridge, "Calcium Oscillations," *J. Biol. Chem.*, vol. 265, p. 9583, 1990. (Cited on page 65.)

[112] K. Kurin-Csörgei, I. Epstein, and M. Orbán, "Periodic Pulses of Calcium Ions in a Chemical System," *J. Phys. Chem. A*, vol. 110, p. 7588, 2006. (Cited on page 65.)

[113] M. Koper, "The theory of electrochemical instabilities," *Electrochimica Acta*, vol. 37, p. 1771, 1992. (Cited on page 65.)

[114] K. Gedalin, "Electro-osmotic oscillations," *Physica D*, vol. 110, p. 154, 1997. (Cited on page 65.)

[115] J. Kelzer and D. Scherson, "A Theoretical Investigation of Electrode Oscillations," *J. Phys. Chem.*, vol. 84, p. 2025, 1980. (Cited on page 65.)

[116] P. Strasser, "Electrochemistry in Self-Organized Dynamical States," *The Electrochemical Society Interface*, Winter 2000. (Cited on page 65.)

[117] Z. Siwy, "private communication," 2007. (Cited on pages 65, 66, 77, and 98.)

[118] R. Blachnik, Ed., *Taschenbuch für Chemiker und Physiker, Band III: Elemente, anorganische Verbindungen und Materialien, Minerale*, 4th ed. Springer, 1998. (Cited on page 65.)

[119] D. Lide, *CRC Handbook of Chemistry and Physics*, 84th ed., D. Lide, Ed. CRC Press, 2003. (Cited on page 65.)

[120] L. Milescu, C. Nicolai, J. Bannen, H. Ananthakrishnan, F. Qin, T. Auerbach, and F. Sachs, "QuB, Version 1.4.0.60," Copyright (C) 1998-2004 University at Buffalo. [Online].

Available: http://www.qub.buffalo.edu/wiki/index.php?title=Main_Page&redirect=no (Cited on page 67.)

[121] W. Coulter, "Means for counting particles suspended in a fluid," US Patent 2656508, 1953. (Cited on page 79.)

[122] R. DeBlois and C. Bean, "Counting and sizing of submicron particles by resistive pulse technique," *Rev. Sci. Inst.*, vol. 41, p. 909, 1970. (Cited on page 79.)

[123] R. DeBlois, C. Bean, and R. Wesley, "Electrokinetic measurements with submicron particles and pores by resistive pulse technique," *J. Coll. Int. Sci.*, vol. 61, p. 323, 1977. (Cited on page 79.)

[124] G. Church, D. Deamer, D. Branton, R. Baldarelli, and J. Kasianowicz, "Characterization of individual polymer molecules based on monomer-interface interactions," US patent 5795782, 1998. (Cited on page 79.)

[125] L. Song, M. Hobaugh, C. Shustak, S. Cheley, and H. Bayley, "Structure of staphylococcal α-hemolysin, a heptameric transmembrane pore," *Science*, vol. 274, p. 1859, 1996. (Cited on pages 80 and 81.)

[126] D. Deamer and D. Branton, "Characterization of Nucleic Acids by Nanopore Analysis," *Acc. Chem. Res.*, vol. 35, p. 817, 2002. (Cited on page 80.)

[127] S. Winters-Hilt, W. Vercoutere, V. DeGuzman, D. Deamer, M. Akeson, and D. Haussler, "Highly accurate classification of Watson-Crick basepairs on termini of single DNA molecules," *Biophys. J.*, vol. 84, p. 967, 2003. (Cited on pages 80 and 85.)

[128] N. Ashkenasy, J. Sánchez-Quesada, H. Bayley, and M. Ghadiri, "Recognizing a single base in an individual DNA strand: A step toward DNA sequencing in nanopores," *Angew. Chem.*, vol. 44, p. 1401, 2005. (Cited on page 80.)

[129] J. Mathé, A. Aksimentiev, D. Nelson, K. Schulten, and A. Meller, "Orientation discrimination of single-stranded DNA inside the α-hemolysin membrane channel," *Proc. Natl. Acad. Sci. USA*, vol. 102, p. 12377, 2005. (Cited on page 81.)

[130] T. Butler, J. Gundlach, and M. Troll, "Determination of RNA orientation during translocation through a biological nanopore," *Biophys. J.*, vol. 90, p. 190, 2006. (Cited on page 81.)

[131] A. Sauer-Budge, J. Nyamwanda, D. Lubensky, and D. Branton, "Unzipping kinetics of double-stranded DNA in a nanopore," *Phys. Rev. Lett.*, vol. 90, p. 238101, 2003. (Cited on page 81.)

[132] J. Mathé, H. Visram, V. Viasnoff, Y. Rabin, and A. Meller, "Nanopore unzipping of individual DNA hairpin molecules," *Biophys. J.*, vol. 87, p. 3205, 2004. (Cited on page 81.)

[133] J. Mathé, A. Arinstein, Y. Rabin, and A. Meller, "Equilibrium and irreversible unzipping of DNA in a nanopore," *Europhys. Lett.*, vol. 73, p. 128, 2006. (Cited on page 81.)

[134] M. Bates, M. Burns, and A. Meller, "Dynamics of DNA molecules in a membrane channel probed by active control techniques," *Biophys. J.*, vol. 84, p. 2366, 2003. (Cited on page 81.)

[135] E. Heins, F. Albertorio, T. Yang, Z. Siwy, L. Baker, S. Cheley, H. Bayley, P. Cremer, and C. Martin, "Development of a supported lipid bilayer on porous polymeric support," presented at the 49th Biophysical Society Meeting, Long Beach, CA, USA, 2005. (Cited on page 81.)

[136] R. White, B. Zhang, S. Daniel, J. Tang, E. Ervin, P. Cremer, and H. White, "Ionic Conductivity of the Aqueous Layer Separating a Lipid Bilayer Membrane and a Glass Support," *Langmuir*, vol. 22, p. 10777, 2006. (Cited on page 81.)

[137] M. Wiggin, N. Jetha, D. Trivedi, C. Tropini, J. Nakane, D. Broemeling, and A. Marziali, "Force spectroscopy with nanopores," presented at the 50th Biophysical Society Meeting, Salt Lake City, UT, USA, 2006. (Cited on page 81.)

[138] T. Aref, C. Lo, and A. Bezryadin, "Solid-state nanopores and detection of proteins," presented at the 2nd Focused Workshop on Electronic Recognition of Bio-molecules (ERBM), University of Illinois, USA, 2005. (Cited on page 81.)

[139] J. Kelly, M. Berry, and T. McMaster, "Nanopore translocation of a glycoconjugate structure," presented at the 50th Biophysical Society Meeting, Salt Lake City, UT, USA, 2006. (Cited on page 81.)

[140] C. Ho, R. Qiao, J. Heng, A. Chatterjee, R. Timp, N. Aluru, and G. Timp, "Electrolytic transport through a synthetic nanometer-diameter pore," *Proc. Natl. Acad. Sci. USA*, vol. 102, p. 10445, 2005. (Cited on pages 81 and 82.)

[141] S. Wu, S. Park, and X. Ling, "Lithography-Free Formation of Nanopores in Plastic Membranes using Laser Heating," *Nano Lett.*, vol. 6, p. 2571, 2006. (Cited on page 81.)

[142] C. Danelon, C. Santschi, J. Brugger, and H. Vogel, "Fabrication and Functionalization of Nanochannels by Electron-Beam-Induced Silicon Oxide Deposition," *Langmuir*, vol. 22, p. 10711, 2006. (Cited on page 81.)

[143] A. Storm, J. Chen, H. Zandbergen, and C. Dekker, "Translocation of double-strand DNA through a silicon oxide nanopore," *Phys. Rev. E*, vol. 71, p. 051903, 2005. (Cited on page 82.)

[144] J. Li, M. Gershow, D. Stein, E. Brandin, and J. Golovchenko, "DNA molecules and configurations in a solid-state nanopore microscope." *Nat. Mat.*, vol. 2, p. 611, 2003. (Cited on page 82.)

[145] A. Storm, C. Storm, J. Chen, H. Zandbergen, J. Joanny, and C. Dekker, "Fast DNA translocation through a solid-state nanopore," *Nano Lett.*, vol. 5, p. 1193, 2005. (Cited on page 82.)

[146] J. Heng, C. Ho, T. Kim, R. Timp, A. Aksimentiev, Y. Grinkova, S. Sligar, K. Schulten, and G. Timp, "Sizing DNA using a nanometer-diameter pore," *Biophys. J.*, vol. 87, p. 2905, 2004. (Cited on page 82.)

[147] P. Chen, J. Gu, E. Brandin, Y. Kim, Q. Wang, and D. Branton, "Probing single DNA molecule transport using fabricated nanopores," *Nano Lett.*, vol. 4, p. 2293, 2004. (Cited on pages 82 and 86.)

[148] U. Keyser, B. Koeleman, S. van Dorp, D. Krapf, R. Smeets, S. Lemay, N. Dekker, and C. Dekker, "Direct force measurements on DNA in a solid-state nanopore," *Nat. Phys.*, vol. 2, p. 473, 2006. (Cited on page 82.)

[149] D. Fologea, J. Uplinger, B. Thomas, D. McNabb, and J. Li, "Slowing DNA translocation in a solid-state nanopore," *Nano Lett.*, vol. 5, p. 1734, 2005. (Cited on page 83.)

[150] D. Fologea, M. Gershow, B. Ledden, D. McNabb, J. Golovchenko, and J. Li, "Detecting single stranded DNA with a solid state nanopore," *Nano Lett.*, vol. 5, p. 1905, 2005. (Cited on page 83.)

[151] R. Smeets, U. Keyser, D. Krapf, M. Wu, N. Dekker, and C. Dekker, "Salt dependence of ion transport and DNA translocation through solid-state nanopores," *Nano Lett.*, vol. 6, p. 89, 2006. (Cited on page 83.)

[152] H. Chang, B. Venkatesan, S. Iqbal, G. Andreadakis, F. Kosari, G. Vasmatzis, D. Peroulis, and R. Bashir, "DNA counterion current and saturation examined by a MEMS-based solid state nanopore sensor," *Biomed. Microdev.*, vol. 8, p. 263, 2006. (Cited on page 83.)

[153] R. Fan, R. Karnik, M. Yue, D. Li, A. Majumdar, and P. Yang, "DNA translocation in inorganic nanotubes," *Nano Lett.*, vol. 5, p. 1633, 2005. (Cited on page 83.)

[154] K. Healy, "Nanopore-based DNA analysis," Ph.D. dissertation, University College Cork, Ireland, 2006. (Cited on page 83.)

[155] C. Wilhelm, M. Winterhalter, U. Zimmermann, and R. Benz, "Kinetics of pore size during irreversible electrical breakdown of lipid bilayer membranes," *Biophys J.*, vol. 64, p. 121, 1993. (Cited on page 85.)

[156] LOFO High Tech Film GmbH, "Technical information Aryphan." (Cited on page 96.)

[157] I. Vlassiouk and Z. Siwy, "Nanofluidic Diode," *Nano Lett.*, 2007, published online ahead of print. (Cited on page 99.)

[158] B. Fischer, M. Heiss, and M. Cholewa, "About the art to shoot with single ions," *Nucl. Instrum. Methods Phys. Res., Sect. B*, vol. 210, p. 285, 2003. (Cited on page 99.)

[159] Z. Siwy, L. Trofin, P. Kohli, L. Baker, C. Trautmann, and C. Martin, "Protein biosensors based on biofunctionalized conical gold nanotubes," *J. Am. Chem. Soc.*, vol. 127, p. 5000, 2005. (Cited on page 99.)

ACKNOWLEDGMENTS

At this point I would like to thank all people who contributed to the success of this work:

- R. Neumann for the opportunity to perform this work in his group and the freedon of choice concerning its scientific topic. For his constant support, trust in my work and the possibility to attend many interesting international conferences.
- W. Ensinger for accepting to be the second referee of this work.
- K. Healy for being a permanent discussion partner (be it personal or via e-mail), coming up always with new suggestions, ideas or just encouragement. The setup for high-frequency low-noise current measurements was only made possible due to his detailed knowledge of electronics and informatics.
- Z. Siwy for initially introducing me into the nanopore field and always being available for help and advice even from overseas and during the busiest times.
- P. Ramírez for his interest in my work, always giving new impulses for further studies and being a most reliable collaborator. For doing his best in teaching me theory and never making me feel ignorant.
- G. Pépy for sharing his huge knowledge of small angle scattering whenever needed.
- G. Taucher-Scholz, G. Becker and D. Fink for their advice in biology questions, support in sample preparation and sharing lab equipment.
- T. Cornelius for many intensive and fruitful discussions in- and outside out group's coffee room.
- C. Trautmann for the introduction in the field of heavy-ion irradiation and her advice and encouragement.
- K.O. Voss for his LabView support.
- All members of materials research for the friendly atmosphere and the very pleasant working conditions including the regular coffee breaks filled with discussions about life and science.
- My parents and my sister for their constant support during my entire studies, their interest in my work and for just always being there for me.

- Last but not least my partner B. Zielbauer for standing long discussions about physical details, always being at hand to solve technical problems with his experimental smartness and managing to cheer me up in all situations. Just for all the time we spent together and everything he did for me.